POLITECNICO DI MILANO

Scuola di Ingegneria dell'Informazione
Corso di Laurea Specialistica in Ingegneria Elettronica
Dipartimento di Elettronica, Informazione e Bioingegneria

DEVELOPMENT OF AN ON-CHIP MALARIA DIAGNOSTIC TEST BASED ON ELECTRICAL IMPEDANCE DETECTION

Relatore: Prof. Giorgio FERRARI

Correlatori: Prof. Riccardo BERTACCO
                Ing. Marco GIACOMETTI

Tesi di Laurea Specialistica di

Andrea COLLOVINI

Matricola 858309

Anno Accademico 2016-2017

Alla mia famiglia,
che mi ha sempre supportato

Contents

List of Figures

List of Tables

Abstract

This thesis work presents an innovative on-chip malaria diagnostic test, involved in the Tɪᴅ Mᴇᴋɪɪ project, winner of Polisocial Award 2015/2016.

The disposal product of the malaria parasite, known as *hemozoin*, arises from the digestion of haemoglobin, and is used as a diagnostic tool. Combining a non-microfluidic magnetic particle separation and a subsequent impedance measurement, the device exploits the magnetic properties of hemozoin to detect the presence of the parasite in the bloodstream.

Starting from a theoretical analysis of the problem, a new sensor design is introduced and analyzed, with a focus on the electrical detection. An overview of the magnetic working principle is reported, as well as the integration of the two different aspects. The separation is based on the principle that healthy particles deposit on the bottom of a blood drop, and an impedance variation is observed once the infected particles are attracted to the top of the droplet, where the sensor is located.

A thorough description of the microfabrication techniques and procedures used for the production of test devices is given. All the fabrication processes were optimized and implemented at PoliFab, beside a device characterization.

Theoretical relations are in agreement with the obtained experimental results conducted on biological particles, and a discussion of magnetic and electrical properties of hemozoin is presented, as a proper characterization of this substance is not present in literature.

Riassunto

Questo progetto di tesi presenta un innovativo test diagnostico on-chip per il rilevamento della malaria, inserito nel contesto del progetto TID MEKII, vincitore del Polisocial Award 2015/2016.

Il prodotto di scarto del parassita della malaria, denominato *emozoina*, è formato dalla digestione dell'emoglobina, ed è utilizzato come strumento diagnostico. Combinando un sistema di separazione magnetico non microfluidico e una successiva misura di impedenza, il dipositivo sfrutta le proprietà magnetiche dell'emozoina per rilevare la presenza del parassita nel flusso sanguigno.

Partendo da un'analisi teorica del problema, la struttura del nuovo sensore è introdotta e analizzata, con un approfondimento sul rilevamento elettrico. È riportata una panoramica del principio di funzionamento della parte magnetica, così come l'integrazione dei due diversi aspetti. La separazione si basa sul fatto che le particelle sane sedimentano sul fondo di una goccia di sangue, e si osserva una variazione di impedenza una volta che le particelle infette sono attratte sulla sommità della goccia, dove il sensore è posizionato.

È presente un'approfondita descrizione di tecniche e procedure usate per la microfabbricazione dei dispositivi di prova. Tutti i processi sono stati condotti a PoliFab, così come la caratterizzazione dei dispositivi.

Le relazioni teoriche si sono rivelate in accordo con i risultati sperimentali effettuati su particelle biologiche, e le proprietà magnetiche ed elettriche dell'emozoina sono discusse, poiché una caratterizzazione completa di questa sostanza non è presente in letteratura.

Chapter 1

Introduction

1.1 Pathology

Malaria is the most diffused among parasitic diseases, with 200 million new cases and more than 400 000 deaths worldwide in 2015[1], and it accounts for 40% of the total medical expenses of over 100 countries. Specifically, Africa hosts 88% of the cases and 90% of the total deaths[2,3], clearly reported in Figure 1.1.
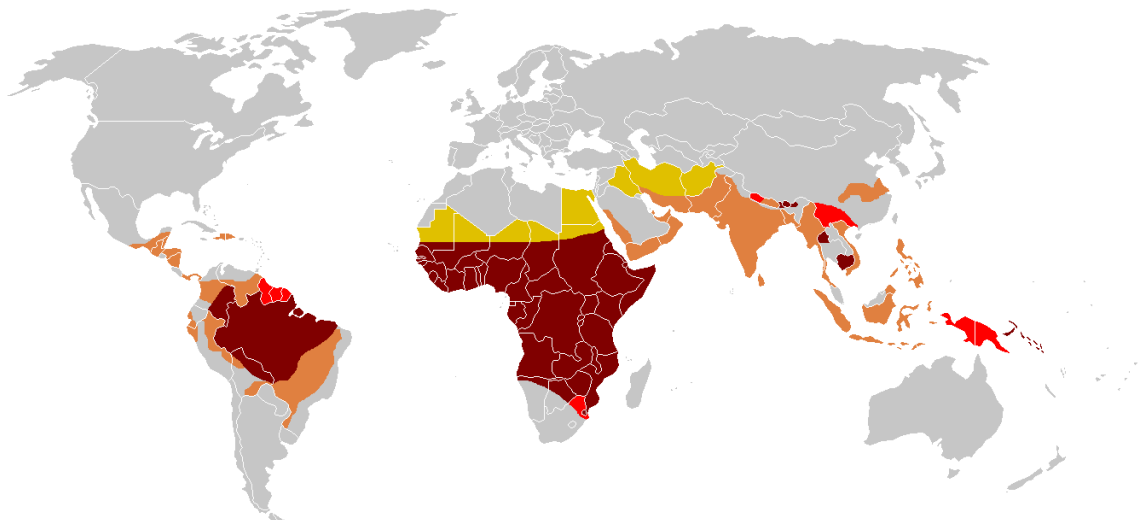
Figure 1.1: Malaria diffusion around the world[4]

- High chemoresistant Plasmodium Falciparum infection risk
- Chloroquine-resistant strains infection risk
- Chloroquine-sensitive Plasmodium Falciparum or Vivax infection risk
- Limited malaria infection risk

Malaria is transmitted by the bite of an infected mosquito, and its natural life-

cycle involves parasites infecting successively two types of hosts: humans and female *Anopheles* mosquitoes, as explained in Figure 1.2. In humans, parasites grow and multiply in the liver cells first (hepatocytes), and then in the red blood cells (RBCs). Successive broods of parasites grow inside the erythrocytes and destroy them[5], releasing daughter parasites, also known as *merozoites*, that continue the cycle by invading other RBCs.
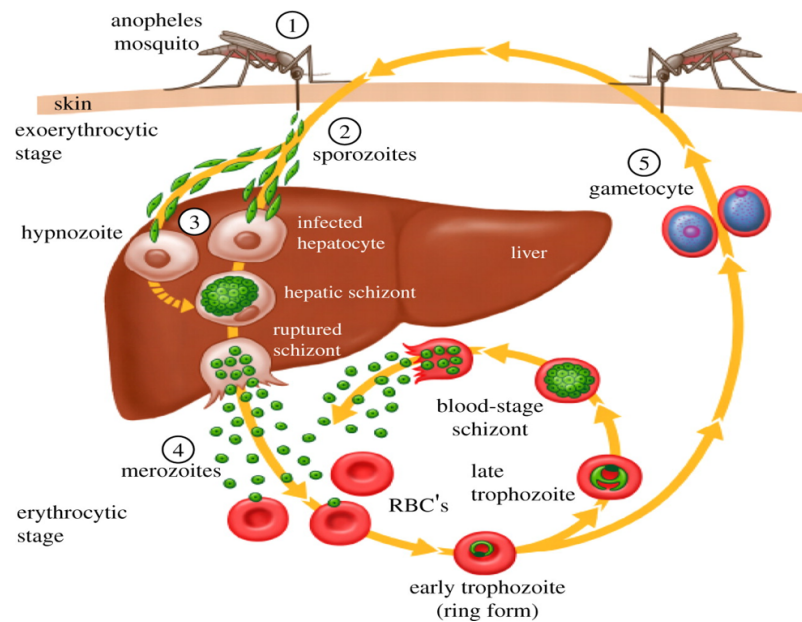
Figure 1.2: Plasmodium life cycle[6]

In Figure 1.3 the different stages of the erythrocyte cycle of the parasite are reported[7]. The parasite is visually darker, as it is marked with *Giemsa stain*, a common cellular marker[8]. It is clear that, as the cycle progresses, Plasmodium increases in number inside the cells, until the membrane rupture occurs. The blood stage parasites (gametocytes) are those that cause the typical malaria symptoms, such as fever, chills, sweats, headaches, muscle pains, nausea, and vomiting. When certain types of gametocytes are picked up by a mosquito during a blood meal, they start another cycle of growth and multiplication right into the mosquito. After 10–18 days, the parasites are found as sporozoites in the mosquito's salivary glands.

When it bites another human, the sporozoites are inoculated along with the mosquito's saliva and begin another human infection cycle, starting from liver cells. Mosquitoes carry the disease from one human to another, acting therefore as a vector, but differently from human hosts, mosquitoes do not suffer from the parasite's presence[7].

The malaria parasite is known as *Plasmodium*, which contains about 200 species, but only four species account for nearly all the human infections: Plasmodium Falciparum, Plasmodium Vivax, Plasmodium Ovale, and Plasmodium Malariae. The deadliest one is *Plasmodium Falciparum.*
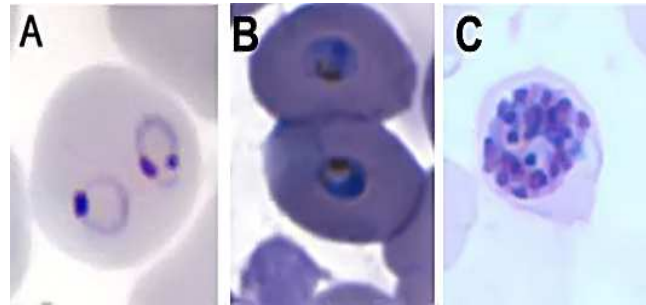
Figure 1.3: Giemsa stained Plasmodium in (A) ring stage, (B) trophozoite stage, and (C) schizont stage, which represent the life cycle of the parasite inside the red blood cell[9]

Plasmodium uses host erythrocyte's *haemoglobin* as a major nutrient source, and it converts the toxic haematin in an insoluble crystal, called *hemozoin*, until the rupture of the membrane happens.

In this phase a fever peak occurs, but this symptom cannot be univocally associated with malaria, therefore it is often neglected. Although the pathology can be pharmacologically effectively treated in an early stage, the diagnostic tests presently available in an African dispensary can't provide an efficient screening of the population.

1.1.1 Hemozoin

Bibliographic data suggests hemozoin to be made of Iron (III) *Protoporphyrin* IX (PPIX)[9–11], which has a similar structure to said compound's insoluble precipitate, β-haematin (Figure 1.4), and through techniques like X-ray diffraction, infrared spectroscopy, and solubility studies, it has been proven that β-haematin is structurally identical to hemozoin[12,13].

Later on, it was proved also that β-haematin and natural hemozoin crystals (HCs) also share the same unitary cell and structure[9,15], beside some optical properties, dichroism above all[9].

A RBC has about 6–8 μm diameter and a thickness of 2–2.5 μm[16], while hemozoin crystals are smaller[9], but their number is far superior, about 20 HCs for every infected red blood cell (iRBC). Hemozoin crystals differ in size quite a bit, as seen
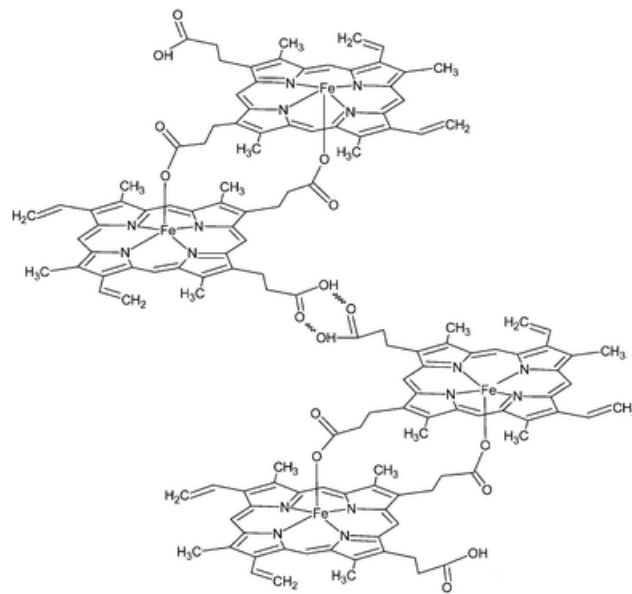
Figure 1.4: Chemical structure of a single crystal of hemozoin[14]
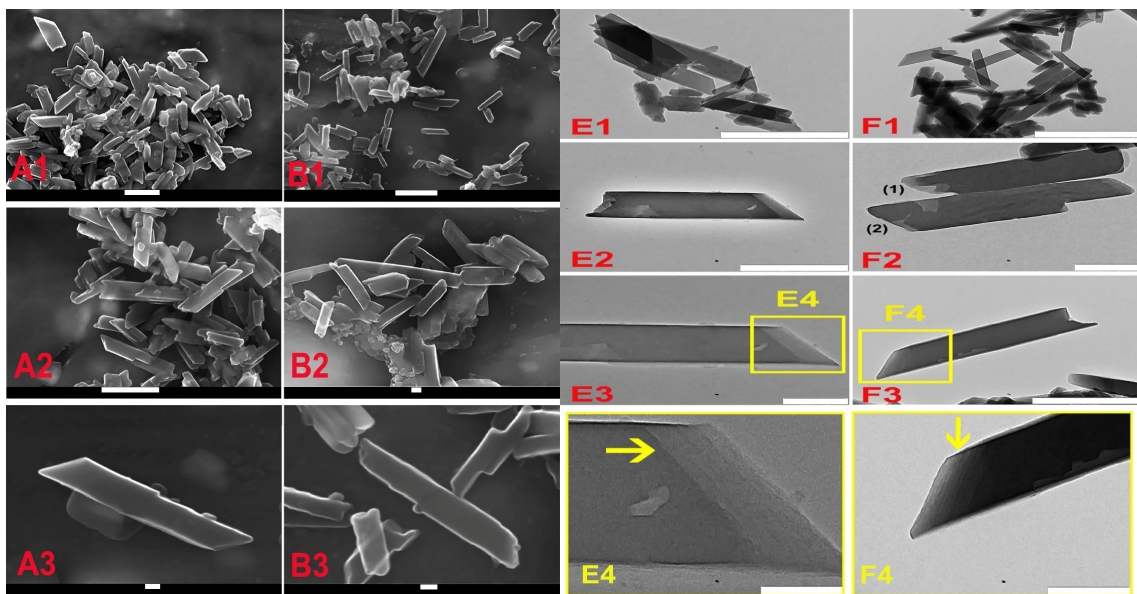
Figure 1.5: Various magnification SEM images showing heterogeneity of shape and size for crystals of native hemozoin from P. Falciparum strains. Yellow arrows and squares indicate the layered structure at the edge of the tips. Scale bars are 1 μm for A1, A2, B1, E1, F1, 500 nm for E2, F3, 200 nm for E3, F2, F4, 100 nm for A3, B2, B3, E4[9]

in Figure 1.5, taken with a scanning electron microscopy (SEM), namely their approximate size is thought to be 1 $\mu m \times 400\ nm \times 200\ nm$, and roughly three to five crystals are produced per parasite[9,15,17]. Besides, shape and size of hemozoin crys-

tals identifies different Plasmodium species, namely all strains share the unit crystal structure of β-haematin, but have different morphologies[17,18].

Bibliographic data suggests hemozoin crystals to be paramagnetic[19,20], or even superparamagnetic[21]. Subsequently, also erythrocytes containing HCs become paramagnetic[22,23]. These properties are discussed in Chapter 2.

1.2 Prevention and treatment

Malaria is a preventable and treatable disease, but it can be a severe, potentially lethal disease (especially when caused by Plasmodium Falciparum) and treatment should be initiated as soon as possible.

The aim of this project is to develop a simple and inexpensive method to diagnose malaria, compared to the current ones (discussed in Section 1.4), to eradicate it even in poor endemic areas.

1.2.1 Social relevance

This project's social relevance is unquestioned at both local and international level. On the one hand, the given analysis clarifies the noteworthy magnitude of the disease in Africa, Asia and South America, on the other hand migrating flows determined a number of cases also in Europe and Italy.

Although malaria is a well-known disease, the insufficient effort to eradicate it in endemic areas let sanitary emergencies arise, as Plasmodium is known to develop a strong drug resistance, especially to the most common ones, available to the local population. A latent malaria state is diffused in Africa, as it is often neglected for a lack of diagnostic instrumentation and adequate drugs, especially in small villages, resulting in a strong personal discomfort, but it also has a notable economic impact.

An immediate and decisive action to eradicate, or at least to contain it, is therefore needed, starting from a widespread, low cost, and early diagnosis, which enables a focused and effective therapy to restrict Plasmodium diffusion.

1.2.2 Prevention

Malaria prevention strategy comprehends two key objectives: the first focuses on core vector control measures, and the second on preventive treatment strategies for the most vulnerable groups in Africa, the former being the main approach to prevent malaria and reduce transmission.

Two forms of vector control are effective in an ample range of circumstances, namely insecticide-treated mosquito nets (ITNs) and indoor residual spraying of insecticides (IRS). ITNs are the backbone of malaria prevention efforts, especially in sub-Saharan Africa. Long-lasting insecticidal nets (LLINs) are designed to kill mosquitoes for 3 years, after that they need to be replaced.

Indoor residual spraying (IRS) is another valid method to quickly reduce malaria transmission. It consists of spraying insecticides on indoor walls and ceilings, where malaria-carrying mosquitoes are likely to rest. In 2015, an estimated 43% of people at risk of malaria in sub-Saharan Africa were not protected by either ITNs or IRS, visible in Figure 1.6a.
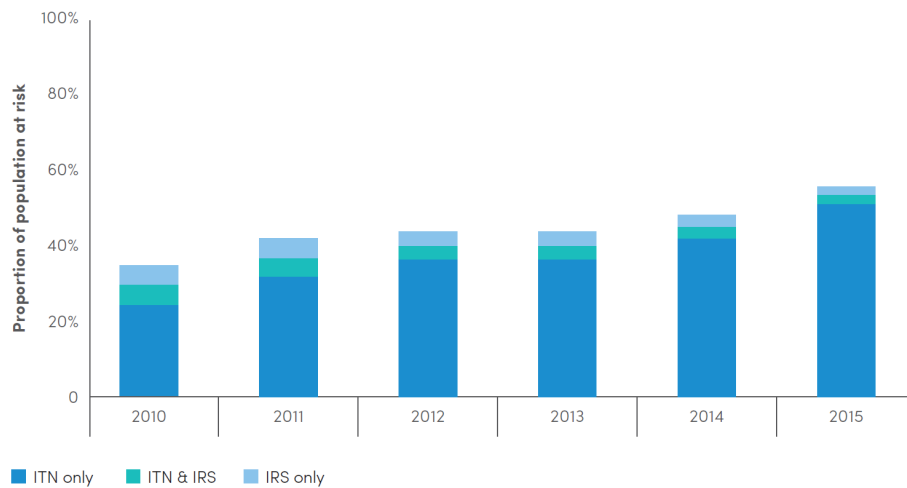
(a) Access to ITNs and IRS
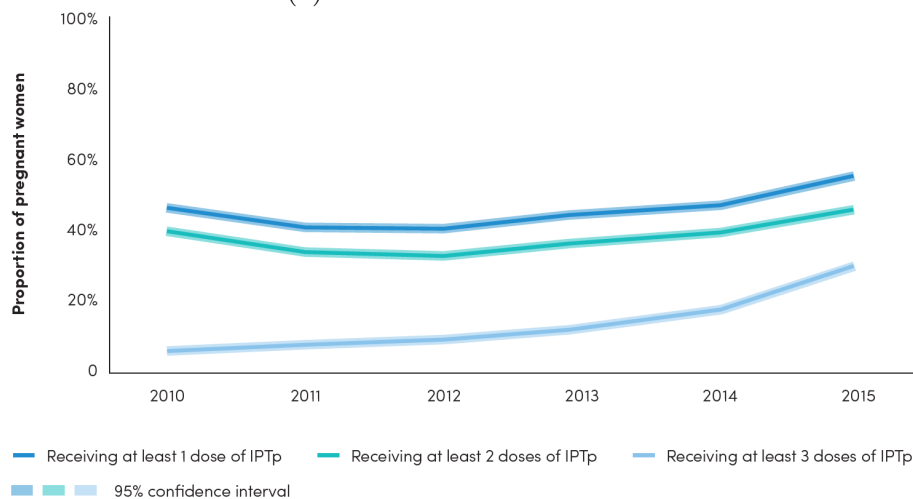
(b) Access to IPTp

Figure 1.6: Growing trend of prevention measures diffusion in sub-Saharan Africa[1]

Preventive measures are advisable for the most threatened groups in malaria-

endemic areas of sub-Saharan Africa: pregnant women, infants and children under 5 years of age. They target only Plasmodium Falciparum and include seasonal malaria chemoprevention (SMC), and intermittent preventive treatment of pregnant women (IPTp), and infants (IPTi)[24]. As an example, IPTp data are reported in Figure 1.6b.

1.2.3   Treatment

Primary objective of treatment is to guarantee complete cure, that is full and prompt elimination of the Plasmodium parasite from the patient's circulation, in order to prevent progression to life-threatening illness, and to chronic infection that leads to malaria-related anaemia.

From a public health perspective, treatment is meant to reduce spreading of the infection, by reducing the contagious reservoir and by preventing the emergence and expansion of resistance to antimalarial medicines.

How a malaria-ill patient is cured depends mainly on the strain of the infecting parasite, the area of contagion and its drug-resistance status, the clinical condition of the patient and any accompanying illness or circumstance, like pregnancy, or allergies to drugs or medications taken by the patient. People who have severe Plasmodium Falciparum malaria or who cannot take oral medications should be continuously given a more powerful intravenous infusion treatment.

Most drugs used in medical care are active against the blood forms of the parasite, that is the ones that cause disease, and include, among others, chloroquine, atovaquone-proguanil, artemether-lumefantrine, mefloquine, and quinine[7]. In addition, primaquine is yielding against dormant liver forms (hypnozoites) and prevents relapses.

Another possible therapy is *hemodialysis*. For example, mPharesis (magnetic aphaeresis) systems[25] operate similarly to a dialysis machine, which consists of draining the patient's blood, continuously removing the infected particles (iRBCs and HCs) by means of high gradient magnetic separation (HGMS), then returning the blood to the circulation.

The design of the mPharesis filter features a series of cascaded channels through which the infected blood follows a laminar flow and is exposed to a high magnetic field gradient. Said gradient is created by an array of ferromagnetic microstructures, placed in close proximity to the flow. The magnetic structures create a localized force field, causing the infected cells to migrate, or *marginate*, towards them, whereupon they are separated from healthy blood through a side branch (bleed-slit). Its working

principle is summarized in Figure 1.7.
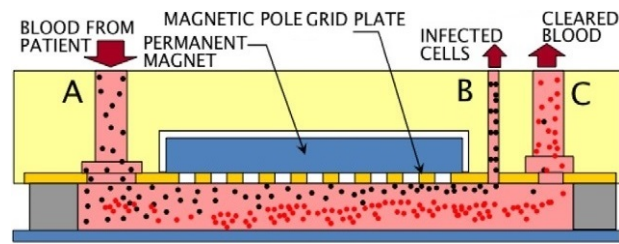
Figure 1.7: Working principle of mPharesis systems[25]

1.3 Tid Mekii project

The goal of this project, called TID MEKII, is to design and develop a fast and pan-plasmodic diagnostic *Lab-on-Chip* test, with sensitivity and reliability at least comparable to the current diagnostic techniques, apt to detect and diagnose early stages of malaria on the field. TID MEKII won Polisocial Award 2015/2016, funded by Politecnico di Milano, and it is proposed and coordinated by Professor R. Bertacco of NaBiS group.

This device exploits the paramagnetic properties of the hemozoin crystals[19,21,22], which are produced by all malaria strains, in two different ways:

- Magnetic separation and counting of infected erythrocytes, which contain hemozoin crystals, differently to healthy ones

- Straight HC attraction and following detection

The first one allows a direct evaluation of the parasitemia (infected RBCs by healthy RBCs ratio), possibly in an early disease stage, before the first Plasmodium reproductive cycle (48–72 h). It leads to the cellular membrane rupture and consequent HC release.

On the other hand, the second type of detection is beneficial regarding the measurement simplicity, since flowing crystals are a clear symptom of an ongoing illness. Besides, people generally go to the hospital only after the first febrile peak, that is after the first cycle has ended and HCs are already in the bloodstream, meaning that the advantages of an early detection of infected erythrocytes would be limited.

However, should widespread preventive care ever happen, the first method might allow earlier diagnosis.

1.3.1 Lab-on-chip

A Lab-on-Chip (LoC) is a miniaturized device which integrates in a single chip one or more analyses usually fulfilled in a laboratory, like DNA sequencing, protein characterization, cell and particle detection and counting.

Miniaturization of biochemical operations made them cheaper, thanks to reduced sample and agent volume, for both device fabrication and analysis. Moreover, it enhanced the test speed, because of shorter mixing time, high surface-volume ratio, and smaller thermal capacities, which translate into a higher control of the process, as the system responds more quickly. A LoC is also characterized by superior sensitivity and parallelization capacity, mainly as a result of the limited sample and device volumes.

However, it is still a relatively young technology, and detection principles not always advantageously scale. Unfavourable physical and chemical properties and phenomena may become predominant, such as surface roughness, capillary forces and chemical interactions.

The fundamental process widely used for LoC fabrication is *photolithography*, explained in detail in Chapter 4.

1.3.2 Working principle

This project's aim is to exploit innovative technologies to develop a tiny, low-cost, and disposable system, using a Lab-on-Chip approach, which allows miniaturization and optimization of complex operations right inside the chip.
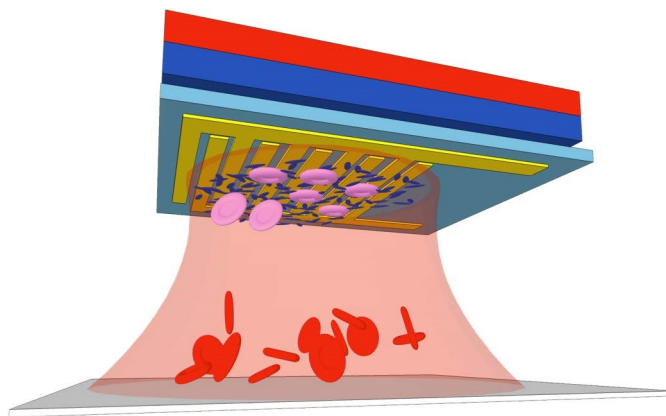
Figure 1.8: A first idea of the device working principle, showing iRBCs in pink and healthy RBCs in red, beside the smaller HCs. The magnet pulls the infected particles, and the gold electrodes sense them

The device is composed of magnetic concentrators and measurement electrodes, shown in Figure 1.8, then USB-connected to an electronic reading module. The tested blood drop is put into contact with the chip surface, and the generated high magnetic gradient pulls iRBCs and HCs to the surface of electrodes, which in turn detect the impedance variation due to the particles by using electrical impedance spectroscopy, covered in Section 2.2. On the contrary, healthy erythrocytes, leukocytes, and thrombocytes do not show paramagnetic properties and deposit on the bottom of the drop, under effect of gravity.

The innovative combination of both non-microfluidic magnetic separation and impedance measurement on a single chip allows a test which consists of:

- High sensitivity (5–10 parasites per μL)

- Quickness of actuation ($<$10 minutes)

- Low sensor cost ($<$1€), and reading module cost lower than 100€

- Tropical-area compatibility, even without specialized staff

The last point is crucial to widely carry out diagnostic screenings, essential to enforce effective restraint policies and disease eradication. Putting this in perspective, TID MEKII may potentially allow a significant advancement, as:

- Magnetic separation and concentration of iRBCs and HCs grants a simple local impedance count

- The system does not need intense oscillating magnetic fields or expensive chemical products

- Differently to other diagnostic methods, slow and unreliable microfluidics is not called for

- Electric measurement grants high sensitivity with low instrumentation complexity

1.3.3 Multidisciplinary work

To develop the diagnostic test, high level competences in very diverse knowledge domains are needed, as reported in Table 1.1. For this reason, this project involves the expertise of many different research groups.

First of all, NaBiS and I³N of Politecnico di Milano, respectively led by Professor R. Bertacco and Professor M. Sampietro, assessed the project feasibility by estimating parameters like maximum attraction distance on the magnetic side, and minimum detectable signal from the electrical standpoint. These two groups carried out also the device realization regarding their own field of competence, including theoretical analysis (Chapter 2), design (Chapter 3), and fabrication (Chapter 4).

Capture tests were accomplished by NaBiS and impedance measurements by I³N, in collaboration with μBS Lab, which provided bovine test erythrocytes with various treatments. More on this topic in Section 5.1.

As of now, human blood samples have not been tested, as the device is still being developed and it is not ready for infected blood testing, so the involvement of the two latter groups is still limited.

Subject	Related activity	Group
Physics, Magnetism and Nanotechnologies	Development and realization of the magnetic nanostructures	NaBiS (DFIS) Professor R. Bertacco
Electronics	Impedance measures development and realization	I³N (DEIB) Professor M. Sampietro
Bioengineering	Hematic treatment	μBS Lab (DEIB) Professor B. Fiore
Biology, Medicine, Tropical diseases	Healthy and infected blood harvest. Comparison with gold standard	Tropical Disease Center at Sacco Hospital Professor S. Antinori
Medicine, Tropical diseases	First field evaluation on a small range of blood samples	COE sanitary operators in Cameroon Dr. B. Lemen

Table 1.1: Needed skills and work division

1.4   State of art

1.4.1   Diagnostics

Currently there are numerous methods to diagnose malaria, either commercially available or in literature.

The highest sensitivity method at the moment is based on gene recognition of the Plasmodium strains through polymerase chain reaction (PCR), also shown in Table 1.2[26], but its complexity and fragility cause this method to be cumbersome

for an African dispensary. Furthermore, its reliability is affected by Plasmodium mutations. PCR is not pan-plasmodic, as it targets specific strains.

The traditional method, which is still considered the gold standard nowadays, consists of counting the infected red blood cells in a blood smear, and it is widely spread because of its adequate sensitivity, simplicity, and cost-effectiveness, as it only requires an optical microscope and a well-trained person[26]. Prior to examination, the specimen is stained (most often with the Giemsa stain) to give the parasites a distinctive appearance. Nevertheless, the results take usually a long time and are subject to interpretation variability, also due to the quality of the reagents and of the microscope, and on the experience of the laboratory technician[27]. A magnetic deposition microscopy could nonetheless improve the detection effectiveness by magnetically concentrating the infected cells in small areas[28].

Recently, rapid diagnostic tests (RDTs) based on antibody-antigen interaction have been introduced also in Africa, in which tested blood drop is commonly obtained from a finger-prick. An antibodies-soaked test strip is put in contact with a blood drop, and when an antigen is captured by the corresponding antibody it produces a visible coloured line. RDTs provide evidence of the presence of parasites in human blood, and are therefore a valid option as a diagnostic method, particularly where good quality microscopy services cannot be readily provided[2,26]. Variations occur between malaria RDT products, though the principles of the tests are similar. RDTs detect specific antigens produced by Plasmodium, which show in the blood of infected people. Some RDTs can detect only one species (Plasmodium Falciparum), but some also detect other strains of the parasite (Plasmodium Vivax, Plasmodium Malariae, and Plasmodium Ovale). However, RDTs are currently too expensive, have low sensitivity, and it was not proven that their performance is adequate under adverse field conditions.

In some implementation proposals, hemozoin crystals sensing happens by means of a magneto-optical (MO) method, magnetically inducing a rotation and measuring the presence of crystal using a laser[29,30]. The rotating-crystal MO technique determines the concentration of hemozoin crystals via their linear *dichroism* and magnetic anisotropy[31]. Hemozoin, under the action of an applied magnetic field, gives rise to an induced optical dichroism related to the hemozoin concentration, thus precise measurement of the dichroism may be used to ascertain the level of malarial infection. Nevertheless, this solution is not appropriate for the African circumstances due to the complexity of the required instrumentation.

Technique	Detectable parasite density (per μL)	Plasmodium species	Infection stage	Sensitivity	Cost (per test)	Operation time (per test)
Microscopy	5–20, 50–100	All species	All stages	Gold Standard	5000€ for a microscope, 0.12€–0.40€ per test	30–60 min
RDT	>100	All species	N/A	~95%	~1€	~20 min
DEP Deformation	N/A	P. Falciparum	All stages	N/A	<0.1€	Depending on sample volume
Electromagnet with wedge-shaped poles	N/A	P. Vivax, P. Malariae	N/A	~25%	<0.1€	6-12 h
Magnetophoretic between stainless wool in a large chamber	5000 for the first chamber, 50 for the second one	P. Falciparum	Trophozoites and schizonts	N/A	<0.1€	~15 min
Magnetophoretic in a microchannel between two magnets	N/A	All species	All stages	N/A	<0.1€	Depending on sample volume
Magnetophoretic between stainless wool in column tube	400	P. Falciparum	Trophozoites and schizonts	95.7%	<0.1€	Depending on sample volume
Magnetophoretic with magnet nanoparticles	30	N/A	N/A	N/A	<0.1€	Depending on sample volume
Magnetophoretic with ferromagnetic material	N/A	P. Falciparum	All stages	99.2%	<0.1€	Depending on sample volume
Magnetic relaxometry	<10	P. Falciparum	All stages	~100%	N/A	~30 min

Table 1.2: A brief recap of the state of art diagnostic techniques presently employed

1.4.2 Separation

Very few diagnostic methods at the moment exploit hemozoin magnetic properties[28,32], and most of the main techniques of magnetic separation at the moment involve a *microfluidic channel*.

Some HGMS methods[33], for instance, call for a Paramagnetic Capture (PMC) 3-channel microfluidic system, in order to efficiently separate white blood cells (WBCs) from red blood cells, exploiting their different magnetic properties in plasma. The single-channel PMC magnetophoretic[34] microseparator consists of a microchannel located at the interface between two glass substrates, a magnetic wire running down of the center of the microchannel for all its length, a fluid inlet port and three outlets (Figure 1.9a).

When an external magnetic field is applied to the microchannel, paramagnetic RBCs are drawn closer to the ferromagnetic wire and diamagnetic leukocytes are forced away as shown in Figure 1.9a. Blood cells can be separated continuously as the whole blood flows through the microchannel of the PMC microseparator.

Efficiency can be increased by adding two stages in cascade to the first one, with noteworthy performance differences, attributed mainly to minimization of fickian diffusion of the RBCs away from the wire. Furthermore, other methods involve effective late-stage iRBC separation, even decent early-stage[32]. Although they use a nickel permanent magnet, they require a microfluidic channel to work properly (Figure 1.9b), as the working principle is similar to the one described above.

A microfluidic channel is however really slow and not easy to manage, as particles differ in size and may obstruct the channel.

1.4.3 Detection

Using a LoC approach, impedance measurement offers a simple, cost-effective, and non-invasive method for monitoring biological particles[16,35].

The first developed cytometer was the so-called *Coulter counter*[36], still used nowadays, which measures the DC resistance variation of a particle flowing through a small orifice, illustrated in Figure 1.10a. Each current pulse corresponds to a single particle moving through the opening, proportional to the displaced fluid, and consequently proportional to the particle size[16,37].

AC measurements can be done to retrieve impedance properties, to diagnose various diseases which affect cells at specific frequencies[38,39]. Electrodes can even be integrated directly as walls of the microchannel, shown in Figure 1.10b. This

(a) Working principle of microfluidic HGMS [33]

(b) Separation of infected RBCs and healthy ones by means of HGMS [32]
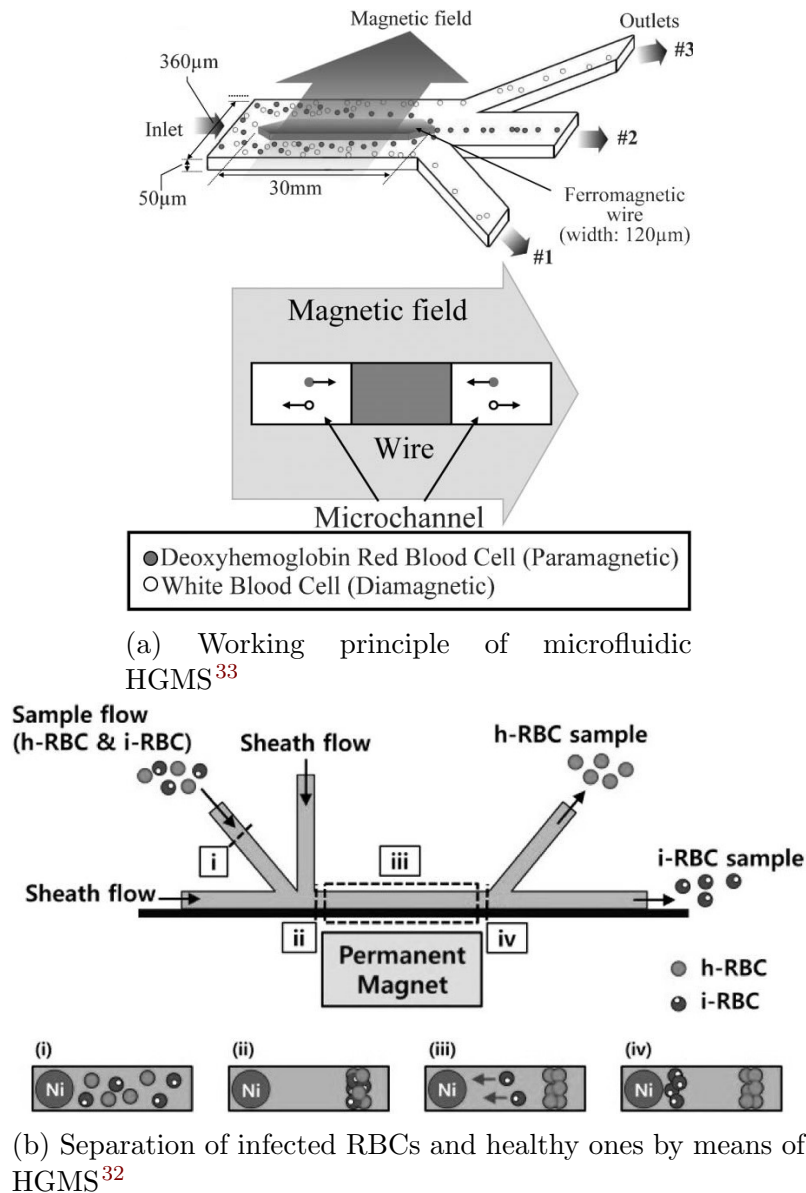
Figure 1.9: Working principle of HGMS and application of it to separate different kinds of particles

configuration is not optimal for sizing the particles though, as different positions inside the channel disturb the electric field in different ways, resulting in discordant impedance values for nominally identical particles [16]. This effect happens especially for planar electrodes, but some techniques can improve the focusing of the particles at the center of the channel taking advantage of hydrodynamic flows [40,41].

The sensitivity of this kind of system increases as the size of the channel approaches the size of the flowing particles, but channel clogging probability inevitably raises. Even though there are techniques to reduce channel clogging and increase
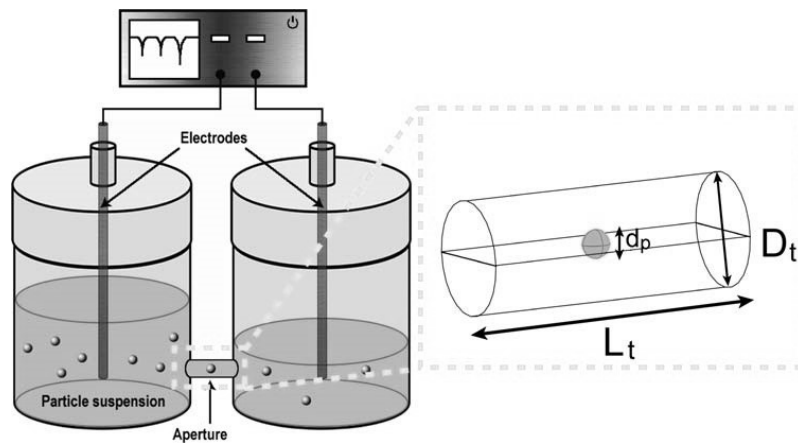
(a) Coulter counter
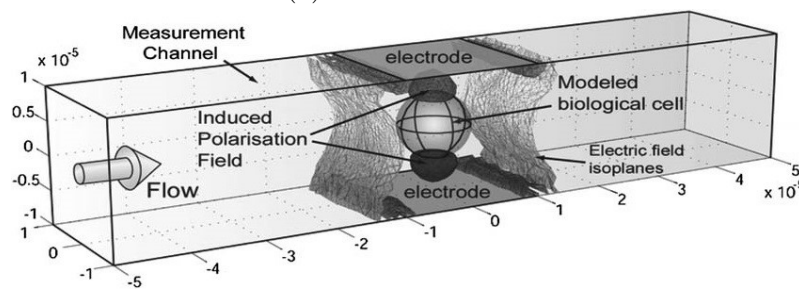
(b) Particle counter, electrodes are integrated in the microchannel

Figure 1.10: When a particle flows through the small aperture between the two chambers, the electrodes sense a current variation. Since particles are usually insulating, the current is reduced as one passes through, so that it can be counted and possibly sized[16]

its throughput[16], employing a microfluidic system should be avoided, as the aforementioned issues are very relevant.
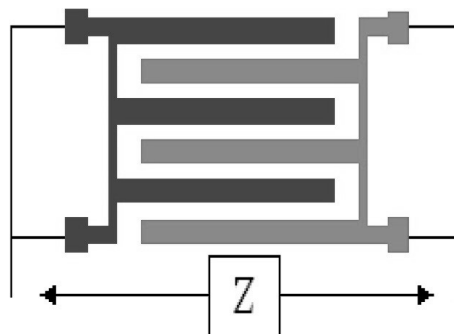
Figure 1.11: Sketch of a coplanar interdigitated electrodes configuration, where Z is the measured impedance[42]

On the non-microfluidic side, the most popular configuration for impedance spec-

troscopy is coplanar interdigitated electrodes (IDE), depicted in Figure 1.11 [16,42–45].

In this configuration the fluid is in contact with the whole IDE area, and it is either dropped through a pipette or the entire sensor is immersed in the liquid. This configuration is beneficial, as it increases the contact area between sensed material and sensor itself, and it can be used in a wide range of fields without substantial design modification [46]. IDE offers a noteworthy versatility though, as the geometrical parameters of the electrodes can be optimized to meet specific demands, thoroughly analyzed in Chapter 3. Moreover, the design is inexpensive, which is a crucial prerogative for mass fabrication [47].

The electrical measurement are typically carried out by means of a technique called electrical impedance spectroscopy, deepened in Section 2.2, and usually resistance or capacitance of the electrodes through the solution are measured.

Chapter 2

Theoretical analysis

2.1 Theoretical background

Considering a blood sample containing 10 iRBCs per μL (the determined limit of detection), and being about $5 \cdot 10^6 \, \mu L^{-1}$ the typical number of healthy RBCs per unit volume[48,49], this system must be able to discern a single iRBC over $5 \cdot 10^5$. It corresponds to a 0.002‰ parasitemia, thus dictating a powerful magnetic separation before the impedance measurement.

It is needed to recall some aspects of magnetism and fluid dynamics, in order to understand how to reach said result.

2.1.1 Magnetism

When an object is immersed in an external magnetic field $\mathbf{H}$, it creates an induced *flux density* $\mathbf{B}$, linearly dependent on its magnetic permeability $\mu = \mu_0 \mu_r$. μ_0 is the permeability constant, while μ_r is the relative magnetic permeability of the material. Moreover, the *magnetization* $\mathbf{M}$ is related to its volume magnetic susceptibility χ, which basically describes its magnetic response to an external field:

$$\mathbf{M} = \chi \mathbf{H} \qquad (2.1)$$

Considering a magnetic material, the total flux density $\mathbf{B}$ is given by the following relation:

$$\mathbf{B} = \mu_0 (\mathbf{M} + \mathbf{H}) = \mu_0 (1 + \chi) \mathbf{H} = \mu_0 \mu_r \mathbf{H} \qquad (2.2)$$

Measurement system	cgs	SI	Conversion factor
H	Oe (oersted)	$\dfrac{A}{m}$	$1\,Oe = \dfrac{10^3}{4\pi}\dfrac{A}{m}$
B	G (gauss)	T (tesla)	$1\,T = 10^4\,G$
M	$\dfrac{emu}{cm^3}$	$\dfrac{A}{m}$	$1\,\dfrac{emu}{cm^3} = 10^3\,\dfrac{A}{m}$

Table 2.1: A brief summary of the standard magnetic units used in cgs system and in SI

In Table 2.1, the standard magnetic units are reported.

According to its magnetic behaviour, response of a material to an external magnetic field can be identified as diamagnetic ($\mu_r < 1$), paramagnetic ($\mu_r > 1$), or ferromagnetic ($\mu_r \gg 1$). Basically, it can be said that the magnetic permeability describes if an object is attracted to an external magnetic field ($\mu_r > 1$) or repulsed by it ($\mu_r < 1$). Moreover, it can be said that magnetic materials (paramagnetic and ferromagnetic) tend to concentrate flux lines, visually depicted in Figure 2.1.
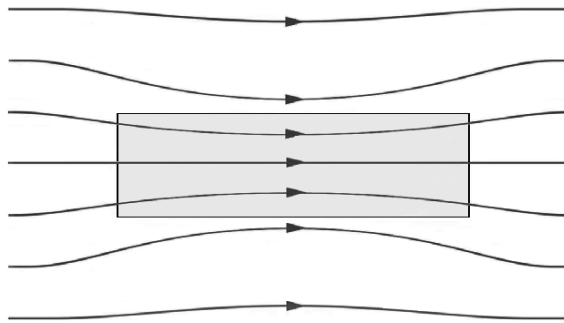
Figure 2.1: A magnetic material ($\mu_r > 1$) tends to concentrate flux lines: the higher is χ, the more concentrated are lines

A different effect emerges when the size of the object is reduced below a certain value (e.g. nanoparticles, or hemozoin crystals[21]), known as *superparamagnetism*. This behaviour is similar to ferromagnetism, but it does not exhibit a hysteresis, as shown in Figure 2.2[50]. Ferromagnetic and superparamagnetic materials exhibit a magnetization saturation if the magnetic field **H** is sufficiently high, and so do paramagnetic and diamagnetic, but with really higher fields.

When a magnetic field **H** is applied, a superparamagnetic particle behaves like a ferromagnet, due to its high μ_r. Nonetheless, when the field is removed, it doesn't show a residual magnetization and a hysteresis, acting as a paramagnetic particle. This effect is dependent on various properties, such as dimensions, temperature,
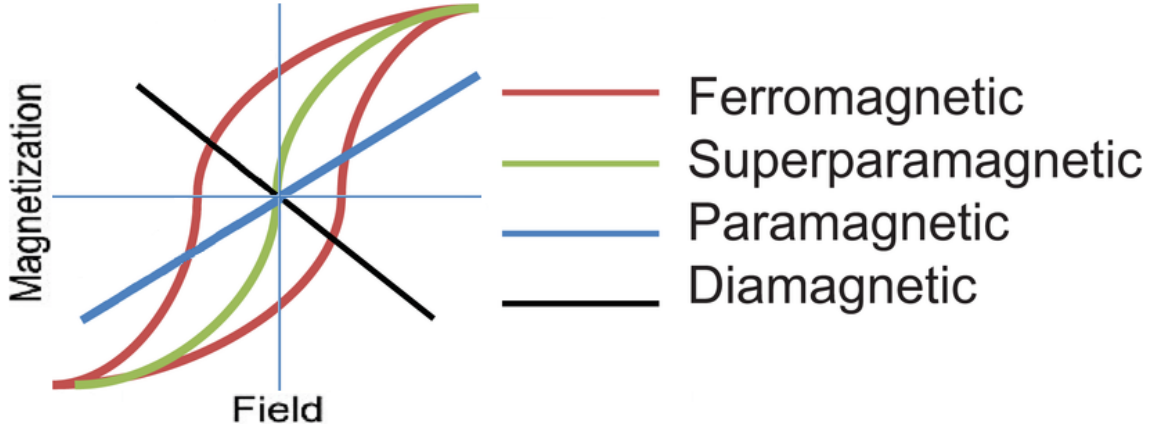
Figure 2.2: Different magnetization behaviours, reported as magnetization $\mathbf{M}$ vs. magnetic field $\mathbf{H}$[51]

and observation time, as it is connected to a transition between two different energy states[50].

Hysteresis absence means that particles like hemozoin can be isolated from a solution and suspended again when the field is removed, which is remarkably useful for biological experiments[52].

The magnetic force acting on a single particle suspended in a medium is:

$$F_m = \frac{\mu_0}{2} V_p (\chi_p - \chi_m) \nabla \mathbf{H}^2 \tag{2.3}$$

Where:

- μ_0 = Vacuum magnetic permeability

- V_p = Particle volume

- $(\chi_p - \chi_m) = \Delta\chi_p$ = Difference between particle and medium susceptibility

- $\mathbf{H}$ = Local magnetic field

With the approximation that the length scale over which the magnetic field changes is larger than the particle diameter, and assuming χ_p linear.

Notably, the magnetic force depends quadratically on the magnetic field gradient and linearly on susceptibility and volume of the particle. Therefore, being:

$$\mu_r = 1 + \chi \tag{2.4}$$

A superparamagnetic particle is subject to a great magnetic force, as its susceptibility is $\chi \gg 0$.

Moreover, the magnetic field gradient can be optimized by modifying the structures so as to concentrate field lines, for example with ferromagnetic (like nickel) microstructures, discussed in Chapter 3.

2.1.2 Fluid dynamics

It is crucial to maximize the magnetic force F_m acting on a particle, presented in Equation (2.3), in order to effectively attract it.

The magnetic force has to oppose the other forces acting on the fluid-suspended spherical particle, which can be described by the Basset-Boussinesq-Oseen equation, neglecting the fluid pressure gradient[25,53,54], as the volume height is really small:

$$\frac{4\pi r^3}{3}\rho_p \dot{v}_p = -\frac{2\pi r^3}{3}\rho_f \dot{v}_p - 6\pi\eta_f r v_p - 6\pi\eta_f r \frac{r}{\sqrt{\pi v_f}}\int_{-\infty}^{t}\frac{\dot{v}_p(t_1)}{\sqrt{t-t_1}}dt_1 - \frac{4\pi r^3}{3}g(\rho_p - \rho_f)$$

(2.5)

Where:

- r = Particle radius

- ρ_p = Particle density

- $\dot{v}_p$ = Particle acceleration

- ρ_f = Fluid density

- η_f = Fluid dynamic viscosity

- v_f = Fluid kinematic viscosity

- g = Gravity acceleration

The second member terms of Equation (2.5) represent, in order, the presence of a virtual mass (given by the resistance shown by the displaced fluid)[55], Stokes drag[56], Basset history term (drag force due to fluid vorticity)[54], and Archimedes buoyancy.

At the first order, virtual mass and Basset history term can be neglected, as the system is considered in steady state, but the magnetic force at the second member should be included[25].

For the particle to be attracted, thus having a positive first member, a magnetic force (Equation (2.3)) just greater than gravity is sufficient. The following relation can be derived:

$$\frac{\mu_0}{2}V_p(\chi_p - \chi_m)\nabla\mathbf{H}^2 > \frac{4\pi r^3}{3}g(\rho_p - \rho_f) + 6\pi\eta_f r v_p \tag{2.6}$$

Considering a static condition, in which drag can be neglected:

$$\frac{\mu_0}{2}V_p(\chi_p - \chi_m)\nabla\mathbf{H}^2 > \frac{4\pi r^3}{3}g(\rho_p - \rho_f) \tag{2.7}$$

Given that hemozoin $\Delta\chi_{HC}$ is higher than $\Delta\chi_{iRBC}$ by a factor of about 175 (as mentioned in Chapter 3), while $\Delta\rho = \rho_p - \rho_f$ for hemozoin is higher than erythrocytes, $\Delta\rho_{HC} > \Delta\rho_{iRBC}$ by a factor of 4, the magnetic field gradient needed to attract hemozoin is lower than the one necessary for red blood cells by a factor of about 45.

2.2 Electrical impedance spectroscopy

After magnetic separation, it is important to quantify the number of attracted infected particles by means of an impedance detection. To count the number of infected cells, electrical impedance spectroscopy can be a powerful experimental technique. It consists of an electrical excitation of a device with a subsequent measure of its response. It usually involves a frequency-varying voltage applied to the device, and a measure of the current flowing through it (Figure 2.3), in order to determine its impedance, according to generalized Ohm's first law[42,57]:

$$Z = \frac{V}{I} \tag{2.8}$$

This kind of approach is rather useful not only for electrochemical purposes[58], but also in biomedical applications, for its promising properties, such as being label-free, real-time, and non-invasive above all[16,35,59].

It may require immobilization of the element under test, or it can involve a microfluidic channel, and in both configurations it has exhibited its high sensitivity and effectiveness[3,9]. Moreover, it was demonstrated that it is possible to use impedance spectroscopy directly on blood[9], which is quite valuable for a disposable sensor like this one.

In recent years, diffusion of lithographic processes enabled the downscaling of sensors to micrometric and nanometric dimensions, which in turn enabled promising perspectives in a wide variety of fields[44].
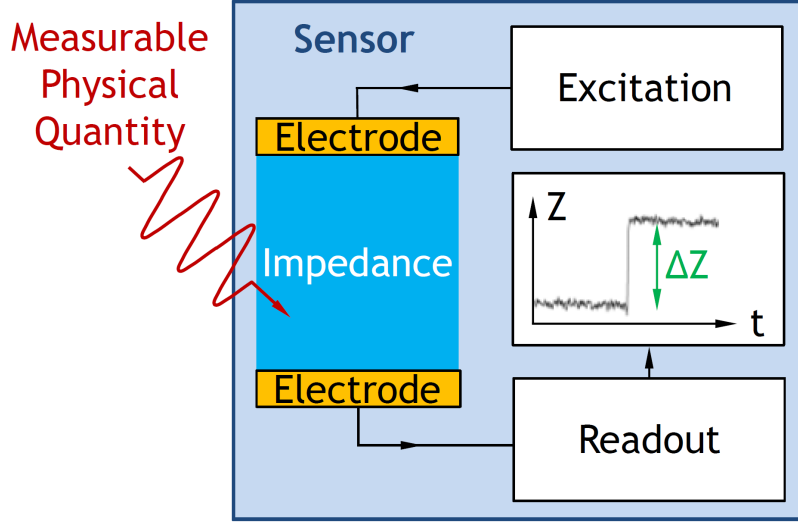
Figure 2.3: Electrical impedance spectroscopy working principle[44]

The most common configuration for impedance spectroscopy is interdigitated electrodes, and it was analyzed and used to be sure of having a functioning device, ubiquitous in bibliography, where Equation (2.9), Equation (2.10), and Equation (2.11) have been obtained from[42]:

$$R_{sol} = \frac{K_{cell}}{\sigma_{sol}} \tag{2.9}$$

$$K_{cell} = \frac{2}{(N-1) \cdot L} \cdot \frac{K(k)}{K(\sqrt{1-k^2})} \tag{2.10}$$

$$K(k) = \int_0^1 \frac{1}{\sqrt{(1-t^2) \cdot (1-k^2 t^2)}} \, dt, \qquad k = cos\left(\frac{\pi}{2} \cdot \frac{W}{S+W}\right) \tag{2.11}$$

$$C_{cell} = \frac{\varepsilon_0 \cdot \varepsilon_{sol}}{K_{cell}} \tag{2.12}$$

$$C_{dl} = \frac{1}{2} \cdot W \cdot L \cdot N \cdot C_{dl}^0 \tag{2.13}$$

Where:

- R_{sol} = Solution resistance, seen from the electrodes

- σ_{sol} = Solution conductivity

- N = Electrode number

- L = Electrodes length

- W = Electrodes width

- S = Electrodes spacing

- C_{cell} = Capacitance resulting from direct capacitive coupling between electrodes

- C_{dl} = Double-layer capacitance, explained in Subsection 2.3.2

- C_{dl}^0 = Characteristic capacitance of the system, per unit area
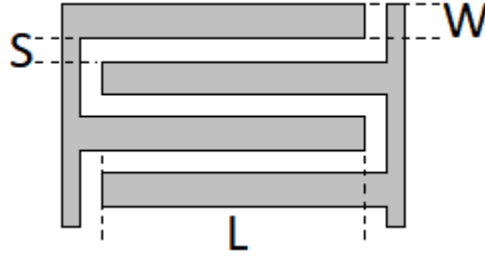
Figure 2.4: Visual representation of the geometrical parameters used for interdigitated electrodes[42]

The meaning of some parameters is also visually represented in Figure 2.4. A good approximation of the integral form is given by Equation (2.14):

$$R_{sol} \simeq \frac{2}{\sigma_{sol} \cdot (N-1) \cdot L} \cdot \sqrt[3]{\left(\frac{S}{W}\right)} \tag{2.14}$$

Equation (2.14) holds for $0.1 < {}^S\!/\!{}_W < 10$, namely most of the currently employed geometries. This relation was validated by means of COMSOL Multiphysics, which returned values similar to the theoretical ones, provided that the electrodes number is sufficiently high, like in Figure 2.5[60].

However, as far as this project is concerned, there is no need to know the exact resistance value, but only its order of magnitude, in order to predict correctly the expected thermal noise and the percentage variation given by infected cells. It is mandatory to know precisely the prospected resistance variation instead, in order to maximize it with a given electrode configuration.

To predict the impedance variation it is important to understand how the impedance changes once the solution is perturbed. Equation (2.15) was derived from Maxwell
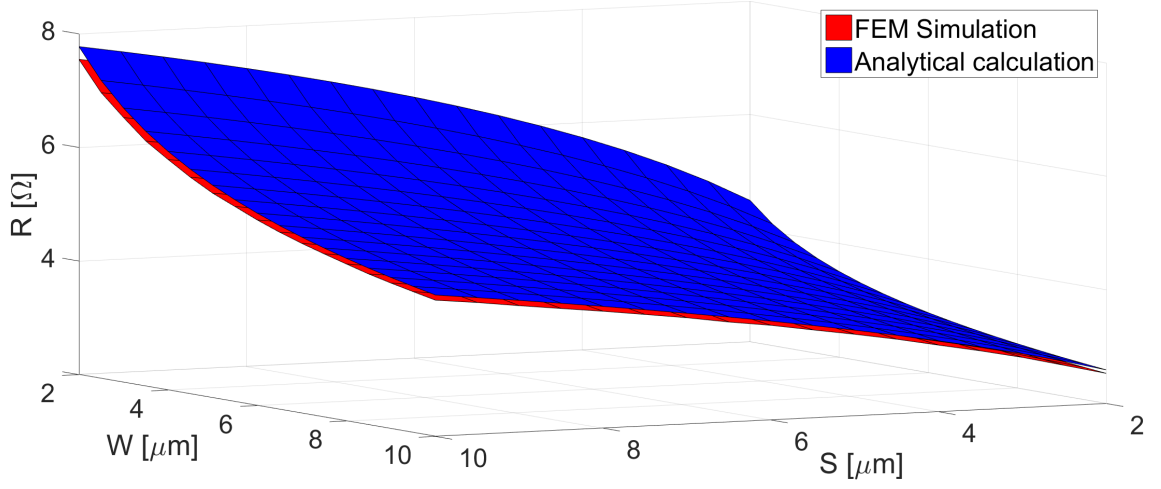
Figure 2.5: Validation of width W and spacing S dependence of Equation (2.14)

mixture theory[16,37,61]:

$$\sigma_{mix} = \sigma_m \cdot \frac{1 + 2\Phi \cdot \left(\dfrac{\sigma_p - \sigma_m}{\sigma_p + 2\sigma_m}\right)}{1 - \Phi \cdot \left(\dfrac{\sigma_p - \sigma_m}{\sigma_p + 2\sigma_m}\right)} \tag{2.15}$$

Supposing the volume fraction $\Phi \ll 1$, it can be approximated to:

$$\sigma_{mix} \simeq \sigma_m \cdot \left(1 + 3\Phi \frac{\sigma_p - \sigma_m}{\sigma_p + 2\sigma_m}\right) \tag{2.16}$$

Hence, by assuming $\sigma_p \ll \sigma_m$, Equation (2.17) can be derived:

$$\rho_{mix} \simeq \rho_m \cdot \left(1 + \frac{3}{2}\Phi\right) \tag{2.17}$$

Where:

- σ_{mix} = Mixture conductivity

- σ_m = Medium conductivity (plasma or PBS)

- σ_p = Particle conductivity (iRBC or HC)

- ρ_{mix} = Mixture resistivity

- ρ_m = Medium resistivity

- Φ = Volume fraction

Equation (2.17) suggests that it is expected a linear relation between resistance variation and attracted particles, as the former depends only on the volume fraction. The validation of Equation (2.17) is given by Figure 2.6, obtained with cells right on interdigitated electrodes.
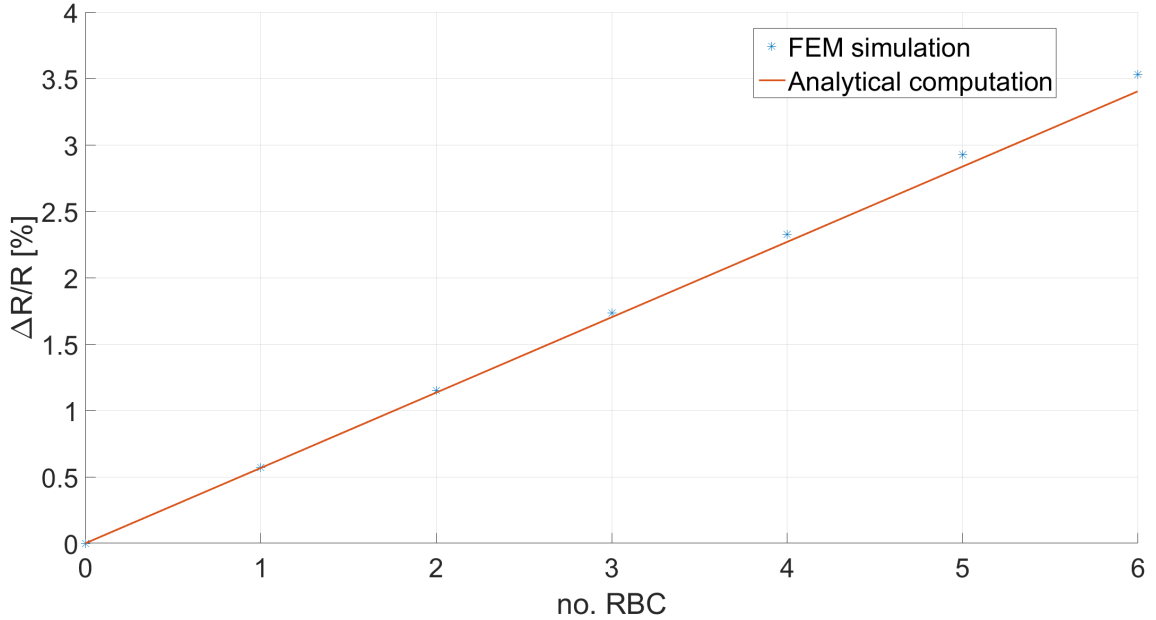
Figure 2.6: Validation of Equation (2.17), it can be clearly seen that the impedance variation is proportional to the number of RBCs

2.2.1 Percentage variation

The impedance variation is the key detection parameter, as the readout electronics focuses around this value to discern between infected and non-infected blood. Moreover, its percentage is important, instead of the absolute differential value, because of two main issues.

The first one concerns temperature variation of the solution over time, since this is expected to be a slow measurement. The solution resistivity changes of about 2% per K, which is of the same order of magnitude (or even higher) with respect to the expected impedance variation due to the particles.

The second one regards noise. The dominant contribution is the well-known Johnson-Nyquist noise[62], also known as *thermal noise*, originated from the brownian motion of electrons in an equilibrium conductor, which leads to a voltage spectral

density:

$$\overline{E_n^2} = 4 \cdot k_b \cdot T \cdot R_{sol} \tag{2.18}$$

Where:

- k_b = Boltzmann constant $\left[\dfrac{J}{K}\right]$

- T = Temperature of the conductor $[K]$

- R = Resistance of the conductor $[\Omega]$

In this device the most relevant contribution is the very own solution, as it is the highest resistance. The total voltage noise can thus be approximated to:

$$\overline{E_n^2} = 4 \cdot k_b \cdot T \cdot R_{sol} \tag{2.19}$$

Or expressed with a current relation:

$$\overline{I_n^2} = \frac{4 \cdot k_b \cdot T}{R_{sol}} \tag{2.20}$$

Flicker noise isn't of much interest, since its contribution becomes absolutely negligible in the MHz range[63].

Supposing $W = S$, R_{sol} analytical expression becomes:

$$R_{sol} = \frac{2}{\sigma_{sol} \cdot (N-1) \cdot L} \tag{2.21}$$

By combining Equation (2.14) and Equation (2.17):

$$\Delta R = R_{mix} - R_{sol} = \frac{2}{\sigma_{mix} \cdot (N-1) \cdot L} - \frac{2}{\sigma_{sol} \cdot (N-1) \cdot L} \tag{2.22}$$

Which yields the percentage variation of the resistance:

$$\frac{\Delta R}{R} = \frac{3}{2} \cdot \frac{V_p}{(2N-1) \cdot L \cdot W \cdot H} \tag{2.23}$$

Where:

- V_p = Total particles volume

- H = Sensitive height of the electrodes

It can be noted that σ_{sol} does not appear in the relation. Equation (2.23) is confirmed by FEM simulations in Figure 2.7.

The total blood drop height H_0, given by the distance at which the magnets can attract particles, does not play a role in the resistance variation, shown in Figure 2.7c, as the sensitivity of the electrodes fades as the particles drift away. The electric field protrudes in the vertical direction for a distance equal to about S[44], which is in turn equal to W in this case, making the effective sensitive height H different from the total volume height H_0. Supposing then $H = W$, further confirmed by FEM simulations, Equation (2.23) for a RBC yields:

$$\frac{\Delta R}{R} = \frac{3}{2} \cdot \frac{N_{iRBC} \cdot V_{iRBC}^0}{(2N - 1) \cdot L \cdot W^2} \tag{2.24}$$

The chip total area is first estimated in $1\ cm^2$, a good trade-off between sample manageability and having a sufficient number of iRBCs inside the volume, subsequently divided in 9 areas, to have statistical significance:

$$\frac{\Delta R}{R} = \frac{1}{9} \cdot \frac{3}{2} \cdot \frac{N_{iRBC} \cdot V_{iRBC}^0}{(2N - 1) \cdot L \cdot W^2} = \frac{1}{6} \cdot \frac{N_{iRBC} \cdot V_{iRBC}^0}{(2N - 1) \cdot L \cdot W^2} \tag{2.25}$$

Where:

- N_{iRBC} = Parasitemia

- V_{iRBC}^0 = Single iRBC volume

Considering Figure 2.8 and a total volume of 5 μL (so a drop height of 50 μm), the magnets spaced 150 μm (as discussed in Chapter 3, this is the radial distance at which magnets can attract particles), 22 electrodes pairs are present in a 3.33 $mm \times$3.33 mm area. It is consequently possible to put some plausible values into Equation (2.25)[16]:

- $N_{iRBC} = 50$

- $V_{iRBC}^0 = 7.06858 \cdot 10^{-17}\,[m^3]$

- $N = 2 \cdot 22 = 44$

- $L = 3.33\,[mm]$

- $W = 2\,[\mu m]$
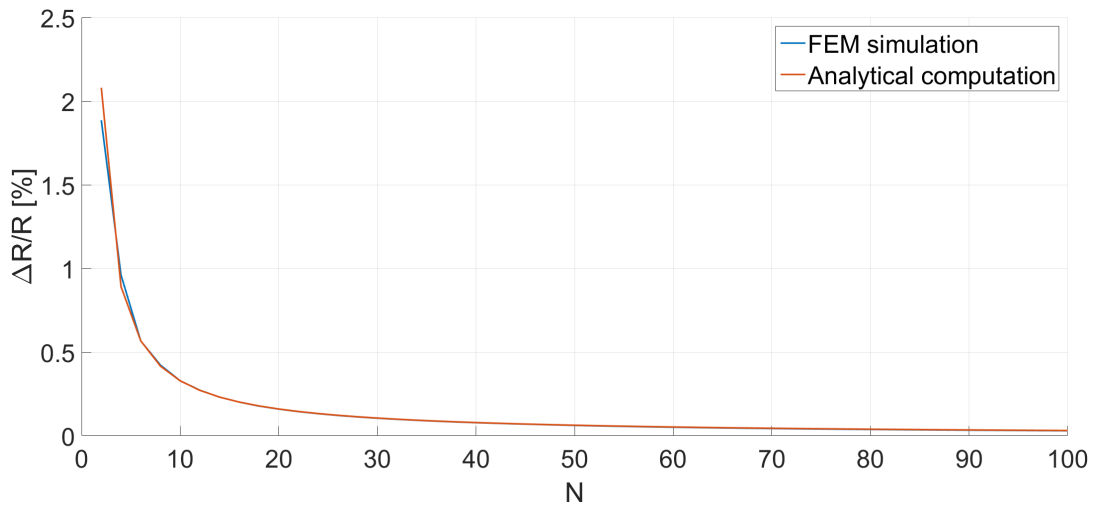
(a) $\Delta R/R$ vs. N
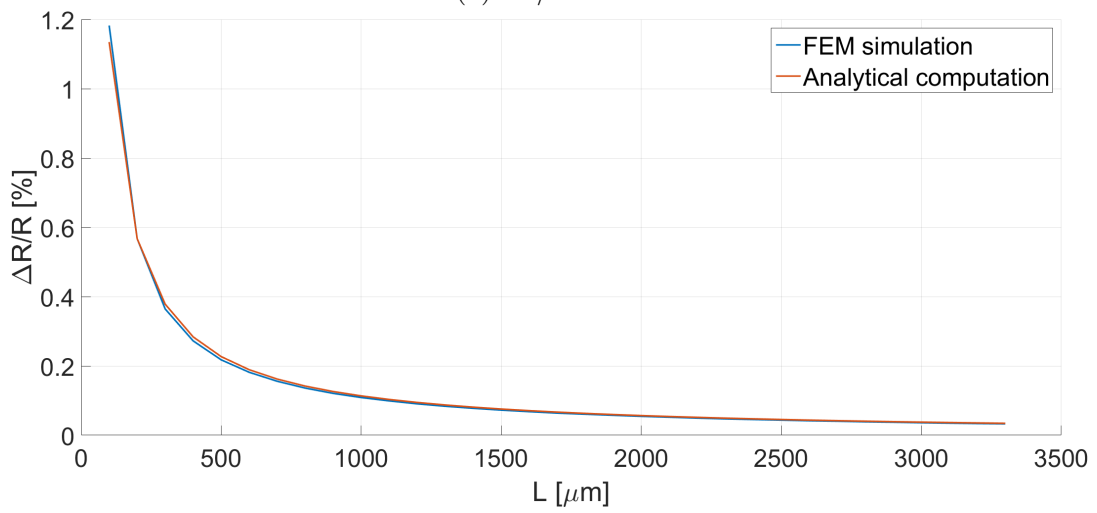
(b) $\Delta R/R$ vs. L
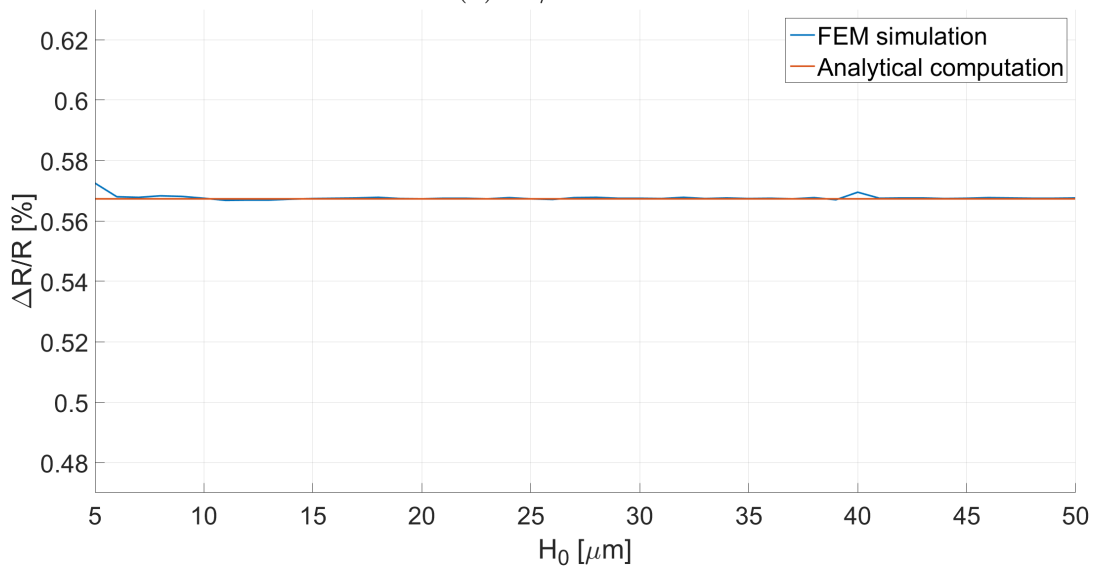
(c) $\Delta R/R$ vs. H_0

Figure 2.7: Validation of Equation (2.23) versus its main parameters
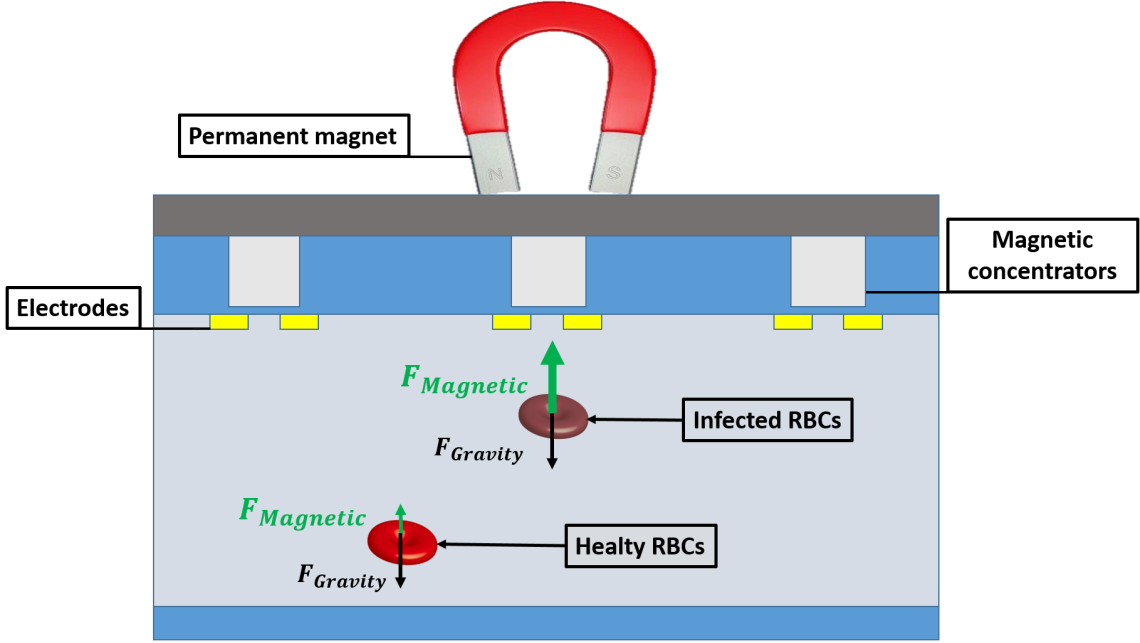
Figure 2.8: Schematic structure of the device, with external magnet and magnetic microconcentrators above electrodes

Finally, it is possible to obtain a first order estimate of the expected percentage variation of the resistance:

$$\frac{\Delta R}{R} = \frac{1}{6} \cdot \frac{50 \cdot 7.06858 \cdot 10^{-17} [m^3]}{(2 \cdot 44 - 1) \cdot 3.33 \cdot 10^{-3} [m] \cdot (2 \cdot 10^{-6} [m])^2} \tag{2.26}$$

$$\frac{\Delta R}{R} = 0.000867 = 0.0867\% \tag{2.27}$$

Equation (2.27) agrees with FEM simulations. Nevertheless, it is a very low variation, which would require immense efforts to be measured correctly, and finding a different solution is then preferable. Discerning the actual signal from the external disturbs and noise is extremely problematic and demanding, mainly due to the medium fluctuations, such as temperature variation, and internal flows causing imbalances in ionic concentrations[16,64]. Also hematocrit level can be a source of noise, as it accounts for about 45% of the total volume of a blood drop, and even once the corpuscles deposit they continue to move about. However, if the drop is sufficiently thick ($H_0 \gg H$) the hematocrit level should not affect the sensitive height H.

The most logical solution to said problems at this point is to modify the geometry, so that it can be tailored to the magnetic layer configuration, in view of the fact that, despite common interdigitated electrodes are remarkably popular and simple to use, they are absolutely not optimized for the detection of such a scarce parasitemia.

Interdigitated electrodes are made to sense diffused corpuscles, while in this device there are supposedly few concentrated particles just on the magnetic concentrators, so it makes sense to optimize also the detection electrodes, in order to weigh only the points where the cells are actually located, adding degrees of freedom and optimization. This is treated in-depth in Chapter 3.

2.3 Electrical model

The most significant component at the measurement frequency of the impedance should be the solution resistance R_{sol}[37,42], in order to see only its variation as a signal. However, some unsought effects are present.

2.3.1 Parasitic effects

A *parasitic effect* can be defined as an unwanted behaviour for an electrical component, namely a property which is not desired for the specific purpose of an element.

In these kinds of sensors and electrodes, parasitic components are typically capacitances, more rarely resistances or inductances. Two main parasitic contributions are expected in this device, namely due to substrate and solution, plus other parasitic components shown in Figure 2.11.

The former is present only in conductive substrates (like silicon), as the SiO_2 coat acts as a dielectric material between the conductive substrate and the gold electrodes, that is precisely a parallel-plate capacitance. It shows a low impedance at medium-to-high frequency, resulting in current flowing through the substrate. It is very detrimental for the measure, as it is in parallel with the solution resistance R_{sol}, as shown in Figure 2.11. This phenomenon obviously does not happen in glass substrates, as it is insulating as a whole, and the preferential path is then the solution itself. For this reason, electrodes on both silicon and glass substrates were fabricated. This effect is directly dependent on the total gold area A deposited on the substrate (electrodes, traces, and pads), and inversely proportional to the thickness of the silicon oxide d, according to the parallel-plate capacitance formula:

$$C = \varepsilon_r \varepsilon_0 \frac{A}{d} \qquad (2.28)$$

For this configuration, connection pads are the bigger contribution to this effect, being usually almost an order of magnitude larger than the total remaining

area combined. This contribution can be reduced or eliminated altogether by removing the pad and directly bonding the traces to an external PCB, treated in Subsection 4.6.2, even though there is still a trade-off between the series resistance of wirings and traces and their substrate capacitance, covered in Section 3.4.

On the other hand, the solution acts as a dielectric material at sufficiently high frequency, so that conductive electrodes and wirings with different polarity make approximately a capacitance. The effect of the electrodes capacitance is evident at high frequency though, well beyond the measurement one, while the capacitance due to the wirings is described in-depth in Section 3.4, and its contribution is dominant over the electrodes one.

An effect known as *double-layer* arises instead at low-to-medium frequency, covered in the following subsection.

Regarding resistive contributions, it can be said that the biggest problem is given by the series resistance of the wirings from electrodes to pads. This can easily surmount R_{sol} if overlooked, jeopardizing the whole measurement.

2.3.2 Double-layer capacitance

There are two kinds of electrodes, known as polarizable and non-polarizable[44,65–67].

The former behaves like a capacitor, and only non-faradaic currents can flow through it. An example is given by inert metal electrodes (like gold, platinum, and titanium) in contact with an electrolyte solution, such as phosphate buffered saline (PBS). There is an intrinsic charge density due to an excess of electrons at the electrode-electrolyte interface[43,65,68–70]. This is due to the fact that, being the metal inert[67], the ions cannot react with it, and they therefore accumulate in a thin layer near the electrodes (up to a few nanometers), illustrated in Figure 2.9. Its value for unit area can be estimated, about $C_{dl}^0 = 0.1 - 0.2 \, [^F/_{m^2}]$.

Double-layer capacitance is a capacitor in series with the solution resistance, and it is clear that at low frequency it is the most predominant contribution of the total impedance[16].

The two models presented in Figure 2.10 differ only for the component at the electrode-electrolyte interface, either an ideal capacitor C_{dl} or a constant phase element (CPE). Empirical data show that the phase of the impedance is constant over frequency at a value higher than -90°, making CPE a better model for the
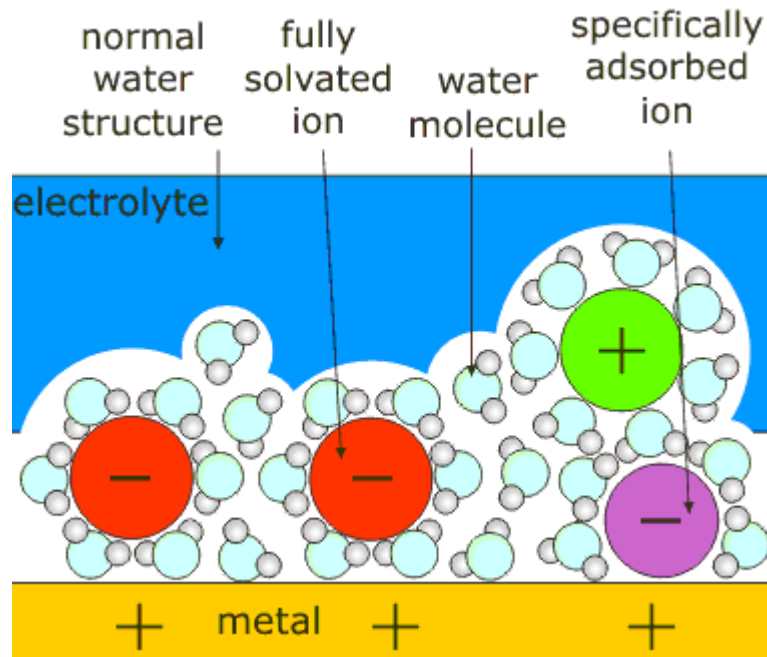
Figure 2.9: Scheme of the formation of a double-layer on a metal[71]

(a) C_{dl} model

(b) CPE model
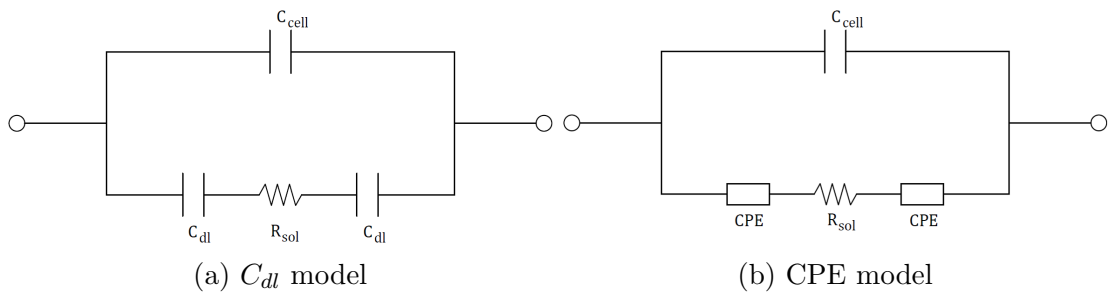
Figure 2.10: Different ways to model electrical double-layer

electrode-electrolyte interface response to AC signals[43]:

$$Z_{CPE} = T \cdot (j\omega)^{-P} \tag{2.29}$$

Equation (2.29) is an empirical formula, and its parameters T and P depend on the properties of both electrode and electrolyte, namely P depends mainly on roughness and porosity of the electrodes[58,66,72,73]. Typical values of P are in the range of 0.8–1.

For sake of simplicity, it will still be treated and referred to as a capacitance, as experimental values exhibit almost the same behaviour as theoretical capacitance curves[43,72]. Besides, an accurate analysis of the low frequency range is not very relevant, since this project aims at a medium-to-high frequency measurement, precisely

to avoid the double-layer effect, as the capacitance does not vary significantly if a particle deposits onto the electrodes.

Yet, it is important to minimize the frequency of the pole due to the double-layer capacitance, so as to widen the resistive plateau as much as possible. It isn't easily adjustable, as directly related to the electrode area in contact with the medium.

To decrease the pole frequency it is recommended to raise this capacitance, but enlarging the electrode area goes to the detriment of the relative variation of the solution given by a single infected cell.

A viable solution is to deliberately increase the roughness of the surface during the fabrication process[74], so that the area at microscopic layer (useful for C_{dl}) increases, but the effective electrode area (useful for the measure effectiveness) doesn't change[58,59,73,75]. However, non-standard lithographic processes should be used (like electroplating[16]), and it is preferable not to employ them during the fabrication of this device unless strictly necessary, as it compromises the reliability of the fabrication.

Conversely, a non-polarizable electrode has a stable interface potential, which remains ideally equal to its equilibrium potential, even when a high current is applied. The employment of non-polarizable electrodes is an effective way to completely remove the double-layer effect[65,66], using materials such as silver-silver chloride[76,77], which is not inert.

Ag/AgCl allows oxidations and reductions, involving the chlorine anions Cl^-, which allow the formation of a low-resistance contact between the electrode and the solution with a high concentration of Cl^-, as biological fluids. The electrode itself is made of silver, with an AgCl coating. The Cl^- ions in the solution react with the Ag electrode, thickening the AgCl layer and producing a positive electrical current from the electrode to the solution. Conversely, AgCl is corroded by losing Cl^-, thinning out and producing a negative current.

Ag/AgCl electrodes are not fabricated without difficulty in the micrometer scale. Besides, the current densities are rather big for electrodes of micrometric size, and the coating is so thin that it deteriorates very quickly (typically about 1 hour)[16,77], making this material not appropriate for employment in this device.

All in all, the described parasitic components are reported in Figure 2.11, where:

- R_{tr} = Resistance of the metallic trace connecting the pad to the active area

- R_{wir} = Resistance of the wirings (connecting the trace to the electrode) across the solution

- C_{wir} = Capacitance of the wirings across the solution

- C_{dl} = Double-layer capacitance

- C_{cell} = Capacitance of the electrodes across the solution

- R_{sub} = Substrate resistance

- C_{sub} = Substrate capacitance

- R_{sol} = Resistance of the solution, only contribution that should ideally exist
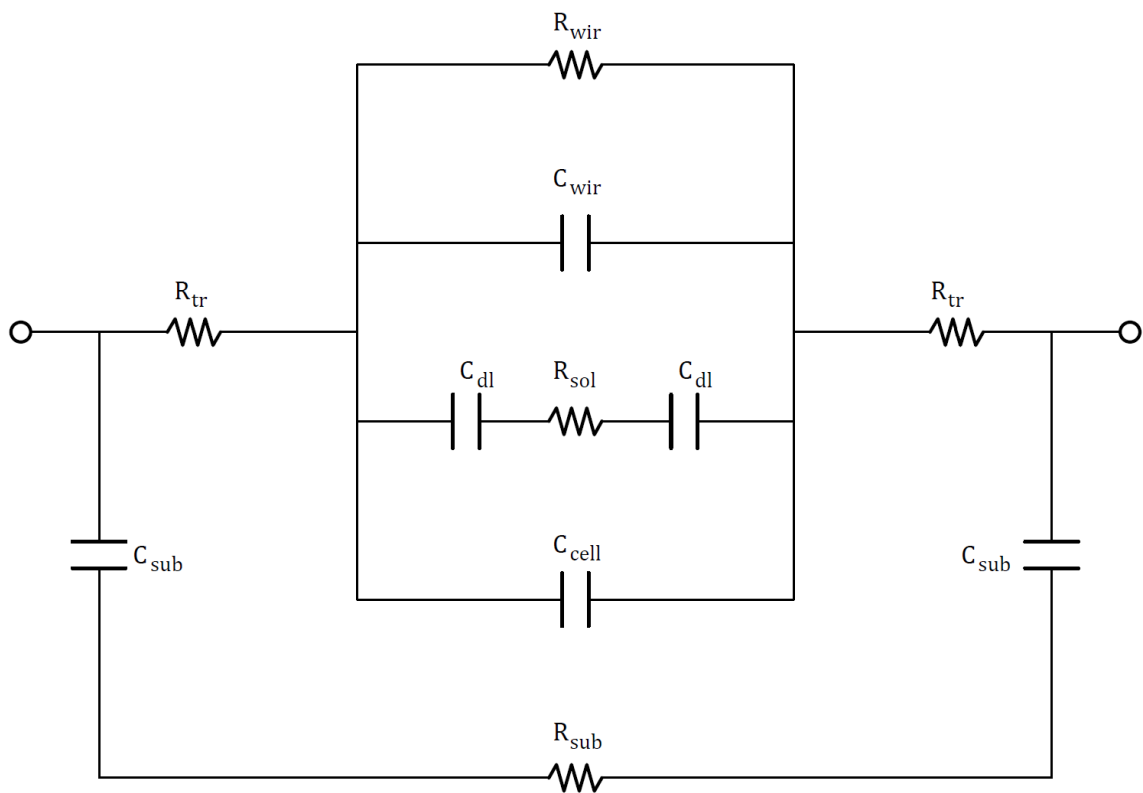
Figure 2.11: Electrical model of the device, comprehending the most significant expected components and behaviours

2.3.3 Differential measure

A differential measure can be exploited to enhance resolution and sensitivity of the system.

Medium fluctuations are relevant, as mentioned in Subsection 2.2.1, but they are approximately regular across a single droplet, and therefore they can be removed by

having a *reference electrode* close to the measurement one. The fluid fluctuations are sensed by both measure electrode and reference one, so their effect vanishes if their currents are subtracted. In an ideal situation, the current flowing through the two electrodes should be equal, and the resulting current should then be:

$$I = I_{ref} - I_{meas} = 0 \qquad (2.30)$$

An unbalance in the currents (e.g. insulating particles in contact with the measurement electrode) results thus in a net current flowing through the device, which in turn is the expected signal. Therefore, the reference electrodes must not have magnetic concentrators above, so that particles are not attracted under them.

In a real case, it is hardly possible to fabricate two perfectly identical electrodes, so the nominal current is inevitably different. This effect can be negligible, as fabricating the electrodes on the same substrate with the same process helps minimizing the structural differences, but even if it wasn't, readout electronics could in theory reduce the net nominal current, for example applying different voltages to the two signals.

The thermal drift may introduce a significant contribution, even greater that the anticipated signal. The temperature can however be assumed constant across the blood drop, and a differential measure can considerably diminish this adverse effect.

Another effect mitigated by a differential measure is the medium evaporation, which can cause a current drift dependent also on the temperature. An ionic solution increases its ion concentration if the water evaporates, lowering its impedance almost at a constant rate in time.

Half of the device area has been reserved to the differential measure and acted as a reference. Even a smaller portion of the chip can be the control area, but this configuration might introduce differences in temperature drift for example, as the current variation could be not proportional across the two areas. Furthermore, by splitting equally the device between active area and reference, the average factor is somehow identical, increasing the effectiveness of the differential measure.

Chapter 3

Design optimization

Magnetic and electrical layers were studied independently, in order for them to be optimized without being restrained by each other's requirements. Of course very specific properties and demands are needed, which are often divergent for the two different standpoints, so a trade-off is necessary.

3.1 Magnetic layer

As cleared by Equation (2.6), maximizing the magnetic field gradient $\nabla \mathbf{H}^2$ is fundamental for the attraction to be effective. To produce a locally-intense magnetic gradient, numerous micro- and nanostructure approaches can be found in literature[68,78,79]. Their magnetic effect is not sufficient to attract particles farther than hundreds of micrometers, though.

A multidimensional approach was therefore considered, by combining a *macroscopic magnet system* (shown in Figure 3.1) to long-range attract particles, and *nickel microstructures* for short-range capture and concentration. The effect of the nickel pillars can be considered negligible for distances greater than 50 μm, after which their magnetic force is one order of magnitude lower than the macroscopic magnet's. Macroscopic and microscopic magnetic simulations have been carried out in separate instances, as the two structures have incompatible size scales, centimeters and micrometers respectively.

Regarding the macroscopic magnet system, it can be said that the vertical component of the magnetic field $\nabla \mathbf{H}_z^2$ is four orders of magnitude greater than the its radial component $\nabla \mathbf{H}_r^2$. In other words, this system contributes greatly to vertical attraction, but its concentration factor is not significant. The employed permanent
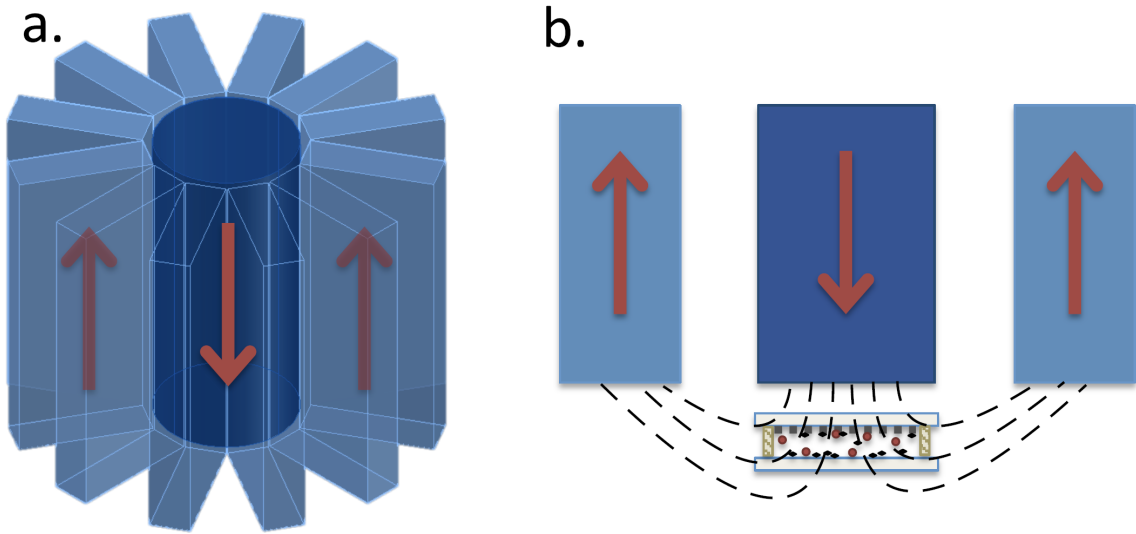
Figure 3.1: Red arrows indicate the magnetization, while black lines represent the magnetic field lines: a. Sketch of the external permanent magnet system b. Section view and positioning relative to the device

magnets are made of neodymium iron boron $Nd_2Fe_{14}B$, inside a 3D-printed poly-lactic acid (PLA) support. The central cylinder is the core of the system, while the surrounding magnets, with opposite magnetization, are needed to increase the macroscopic magnetic field gradient of the system, in fact it nearly doubles.

As deepened in Section 5.4, superparamagnetic properties of hemozoin do not exhibit at all, and its susceptibility value is $\chi_{HC} \simeq 320 \cdot 10^{-6}$ as reported in some bibliographic sources[19,20], instead of being $\chi_{HC} \simeq 3845$[21]. This result has strong implication on the design of the diagnostic device. Infected erythrocytes reveal a paramagnetic behaviour, with different susceptibility values depending on the parasite stage $(\chi_{iRBC} \simeq 0.82 - 1.8 \cdot 10^{-6})$[22,23]. The maximum attraction distance is about 500 μm for iRBCs, and about the same for hemozoin crystals.

3.1.1 Microstructures

Once the particles are attracted, they need to be concentrated by microstructures to be effectively measured. The optimal pattern for microstructures was found by means of FEM simulations in an array of nickel cylinders (shown in Figure 3.2), which is subject to various trade-offs. For optimal attraction, the cylinders need to be closer to each other, but this goes to the detriment of the electrical measure, as only a few concentration points would be optimal from an impedance variation standpoint. Also a big height-over-diameter ratio would help to increase the capture

efficiency, but the fabrication of the pillars becomes progressively more complex. The height is fixed at 20 μm by fabrication reasons, but different diameters and spacings were employed in both FEM simulations and experimental tests. Figure 3.2 is given as an example, where the diameter of the cylinders is 20 μm and their spacing (center to center) is 60 μm. It can be noted that iRBCs and HCs follow different trajectories, due to their different magnetic and viscous properties.

(a) Hemozoin crystals capture trajectories

(b) Infected red blood cells capture trajectories
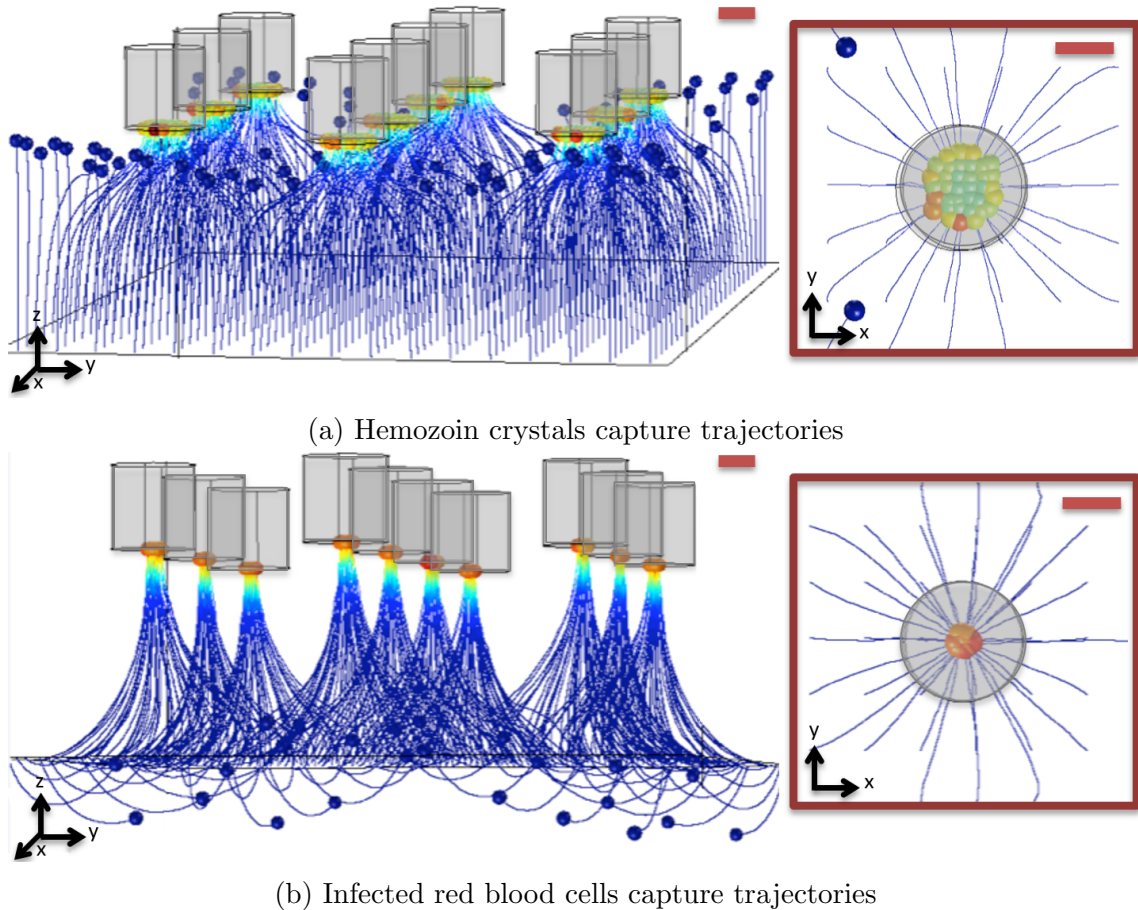
Figure 3.2: Capture trajectories of particles released at 50 μm from the surface of the chip, depicted as 3D perspective (left) and pillar top view (right). The scale bars are 10 μm, while the particles are not in scale

The condition of initial velocity does not affect significantly the attraction mechanism and its timing. Once inside the 50-μm range, HCs are captured within 5 minutes and iRBCs in less than 10 minutes. So the maximum capture time is in the 15–20 minutes scale, since also farther particles must be conveyed in the concentrators proximity, which takes about 10 minutes.

Moreover, a in important figure of merit can be defined: *capture efficiency.* Although it is not a strict definition, it can be seen as the total area of the sensor by

the concentrators capture area, namely the total area occupied by the particles once they are attracted. This figure of merit gives an idea of the concentration factor, or how far can a concentrator radially attract particles.

3.2 Frequency analysis

Unavoidably, capacitive contributions have been extensively investigated, as the choice of the measurement frequency plays a fundamental role in the success of the detection.

The cell is made of a conductive internal cytoplasm inside an insulating external membrane. Being its cut-off frequency around a few MHz, the signal frequency should be kept under 10 MHz, in order not to bypass the membrane[80]. On the other hand, a low-frequency measurement is forbidden by the so-called double-layer capacitance, explained in Subsection 2.3.2.

For all these reasons, it is extremely important to study the impedance spectrum of the electrodes, and fully understand all its contributions, to design the geometry accordingly.
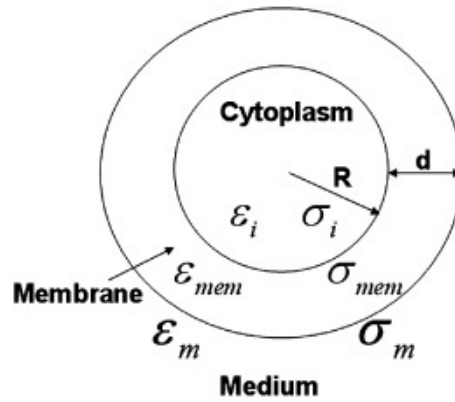
Figure 3.3: Diagram of the single shell cell model, which comprehends only an electrically insulating membrane and the inner conductive cytoplasm[16]

The adopted model is the *single shell* cell model, illustrated in Figure 3.3, and the parameters used for the COMSOL simulations are the following[16]:

- $\varepsilon_0 = 8.854 \cdot 10^{-12} \left[\dfrac{F}{m} \right]$

- $R = 3 \cdot 10^{-6} \, [m]$

- $d = 5 \cdot 10^{-9} \, [m]$

- $\varepsilon_m = 80 \cdot \varepsilon_0$

- $\varepsilon_{mem} = 5 \cdot \varepsilon_0$

- $\sigma_{mem} = 10^{-8} \left[\dfrac{S}{m} \right]$

- $\varepsilon_i = 60 \cdot \varepsilon_0$

- $\sigma_i = 0.4 \left[\dfrac{S}{m} \right]$

For the reasons explained in Section 2.3, an impedance spectrum similar to the one reported in Figure 3.4 is expected[42].
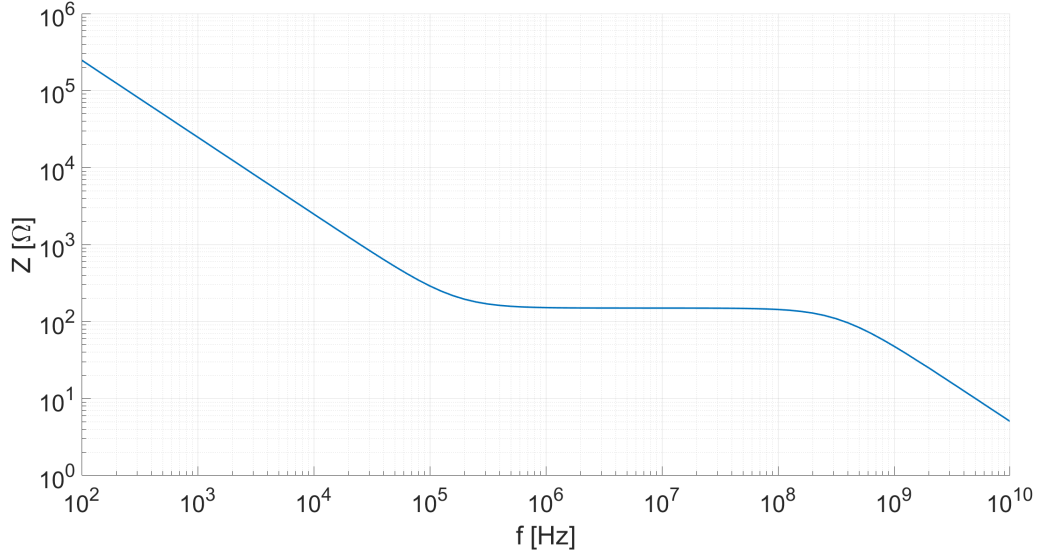
Figure 3.4: Expected impedance spectrum shown by the electrodes, where a large resistive plateau is desired

The resistive plateau is the most important section of the spectrum, as stray capacitances do not impact the impedance, and the measure should therefore be clean of spurious contributions. It is consequently essential to try to spread out the two *corner frequencies* of the resistive plateau associated to C_{dl} and C_{cell}[42]:

$$f_{low} \simeq \frac{1}{\pi \cdot R_{sol} \cdot C_{dl}} \tag{3.1}$$

$$f_{high} \simeq \frac{1}{2\pi \cdot R_{sol} \cdot C_{cell}} \tag{3.2}$$

By replacing R_{sol} with Equation (2.14), C_{dl} with Equation (2.13), and C_{cell} with

Equation (2.12), and considering $W = S$, it can be derived that[42]:

$$f_{low} \simeq \frac{\sigma_{sol}}{\frac{\pi}{2} \cdot K_{cell} \cdot W \cdot L \cdot N \cdot C_{dl}^0} \simeq \frac{\sigma_{sol}}{\pi \cdot C_{dl}^0 \cdot W} \tag{3.3}$$

$$f_{high} \simeq \frac{\sigma_{sol}}{2\pi \cdot \varepsilon_{sol}\varepsilon_0 \cdot} = \frac{1.5 \left[\frac{S}{m}\right]}{2\pi \cdot 80 \cdot 8.85 \cdot 10^{-12} \left[\frac{F}{m}\right]} \simeq 337 MHz \tag{3.4}$$

Measurement frequency should be kept as low as possible, to decrease the complexity of the readout electronics. It is clear that f_{high} does not depend on geometrical parameters, and it is not a problem anyway, being at high frequency. Yet, the plateau can be widened by moving f_{low} to lower frequency, by acting on the geometry of the electrodes. This is not an easy task though, as mentioned in Subsection 2.3.2, since also measurement efficiency must be taken into account, and this is an important trade-off.

Since increasing C_{dl} requires a considerable effort, another path can be taken, namely increasing the value of R_{sol}. This can be achieved by reducing the number of the electrodes N (and so the total area, being the capture efficiency equal), their length L, or the S/W ratio, assuming that σ_{sol} is set by the medium (plasma). However, in so doing the double-layer capacitance would decrease accordingly, and the pole due to it would remain constant. So W is the only parameter that can be truly modified without changing C_{dl} by much.

All the tested electrodes have been designed so as to have a R_{sol} value of about 50–500 Ω. It must be sufficiently high to be the predominant resistive contribution with respect to the resistance of the metallic connections. The FEM simulations were done only on a small portion of the active area (a sensing site), because of complexity and computation time reasons, so the computed R_{sol} is to be divided by the total number of sensing sites, being all in parallel. Besides, the following graphs may differ in impedance absolute value and relative variation, depending on the used parameters. Their main goal is to highlight some guidelines to observe during the fabrication process, and simulated frameworks were mostly designed to analyze a single parameter at a time.

The capture efficiency is given by the magnetic concentration, so reducing the total area is not the finest idea anyway, as this would result in a smaller blood sample, more prone to errors and false positives. The same applies for length, leaving the S/W ratio as a last resort. Nevertheless, as reported in Section 3.3, lower

spacing translates into higher detection efficiency. Therefore, increasing the capture efficiency is priority, so as to reduce N without reducing the total active area.

For electrical modelization purposes, a hemozoin crystal can be seen as a 200-nm-sized square-based parallelepiped, 700-nm thick, and it can be measured in the same way RBCs are, for they are supposedly insulating[9]. An erythrocyte instead is modelled as a cylinder, with a radius of 3 μm and a thickness of 2.5 μm.

3.3 Sensor geometry

After many FEM simulations on COMSOL Multiphysics, a few guidelines and conclusions can be deduced.

The optimal spacing is the smallest possible, clearly visible in Figure 3.5a, to reduce wasted active area, with the attracted particle interrupting almost the whole current flowing through a sensing site, in the theoretical situation. The spacing is then set by the lithography at 2 μm, in order for the process to be sufficiently reliable and reproducible. Even in frequency, taking into account the double-layer capacitance, it is clearly visible that 2 μm is the optimal spacing for this lithographic technology, as illustrated in Figure 3.6.

It is also clearly visible that an optimal measurement frequency exists around 2–2.5 MHz, a trade-off between two capacitive contributions, namely double-layer and cell membrane. This result comes from a FEM simulation, so the frequency is likely to need a slight adjustment, depending on the properties of the fabricated device, because of fabrication tolerance and quality of the deposited metals. Also, the simulation is not extremely precise, and only a couple decimal places of the impedance values (typically of the order of hundreds of $k\Omega$) can be considered accurate, depending on size and type of the simulation[81]. It gives a general idea of the expected frequency range though, and this is an important information.

A lock-in amplifier in this range is feasible, even though it is a relatively high frequency for this kind of measure.

Figure 3.7 gives an idea of the optimal geometry, realizable by a magnetic solution that differs from the original one, treated in Section 3.1.

The electrodes must protrude a lot from wirings, so that the latter don't electrically see each other, and it is even advisable to cover them with an insulating photoresist layer, to further decrease their unneeded interaction. This configuration is kind of similar to a cytometer (like a particle counter[36,82]), where the particles almost completely stop the current flowing through the electrodes, causing a drastic
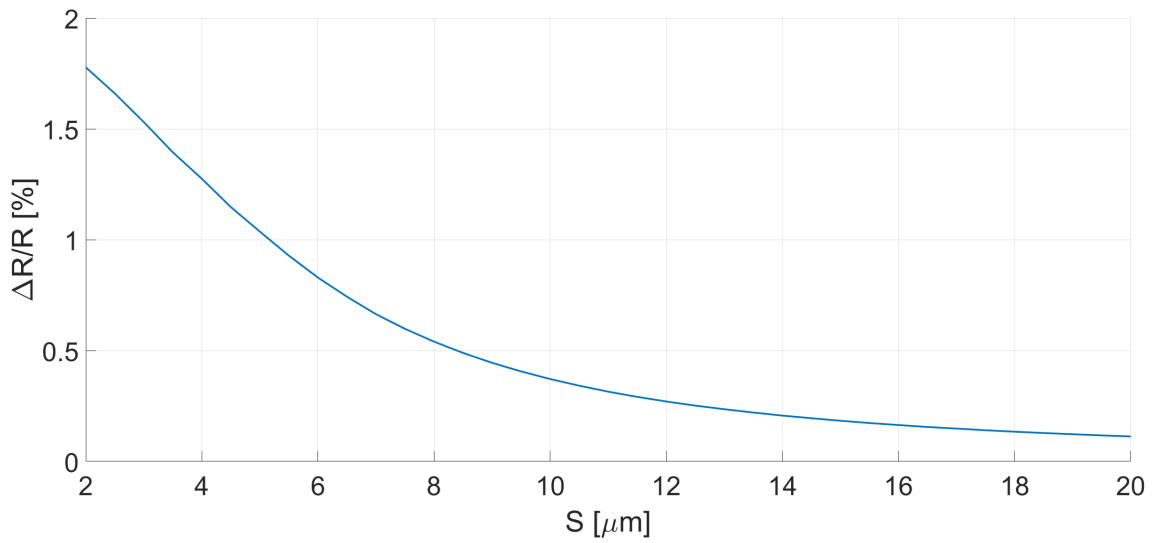
(a) $\Delta R/R$ vs. S
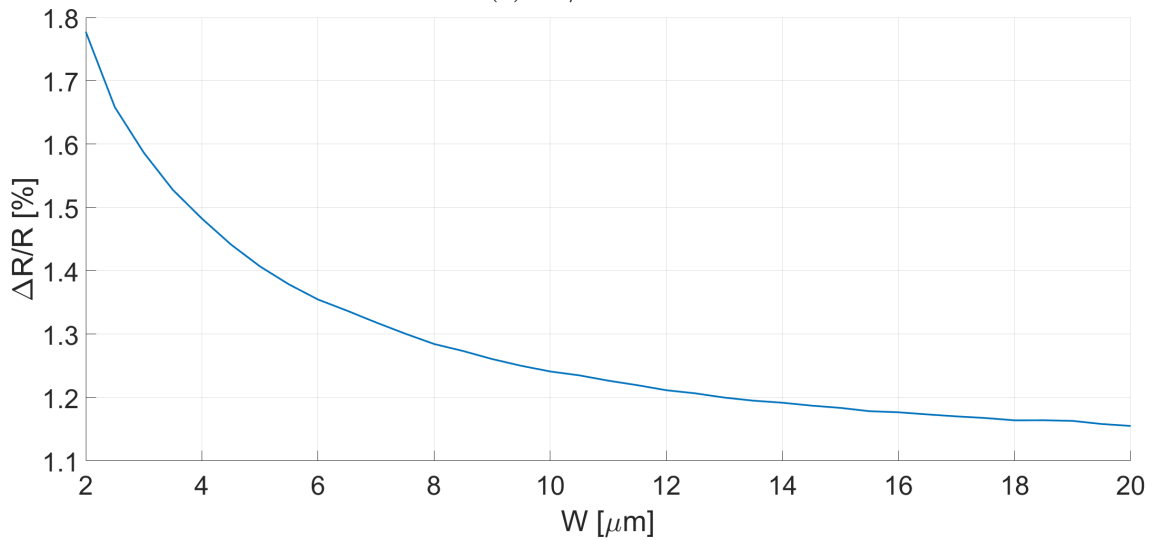
(b) $\Delta R/R$ vs. W

Figure 3.5: Dependence of the percentage variation due to a red blood cell $\Delta R/R$ versus electrode spacing S and width W, taking into account only the resistive component

impedance variation, which translates into a big sensitivity.

The visible portion (in contact with the solution) of the electrodes is best sized as two 2-μm-side squares directly on the center of the magnetic concentrators, which is the smallest (Figure 3.5b) allowed by the fabrication process resolution, while their thickness is set to 100 nm, a good compromise between detection sensitivity, series resistance of the wirings, and structural solidity. Detection sensitivity decreases if electrodes thicken, while the other two properties are better overall with thick
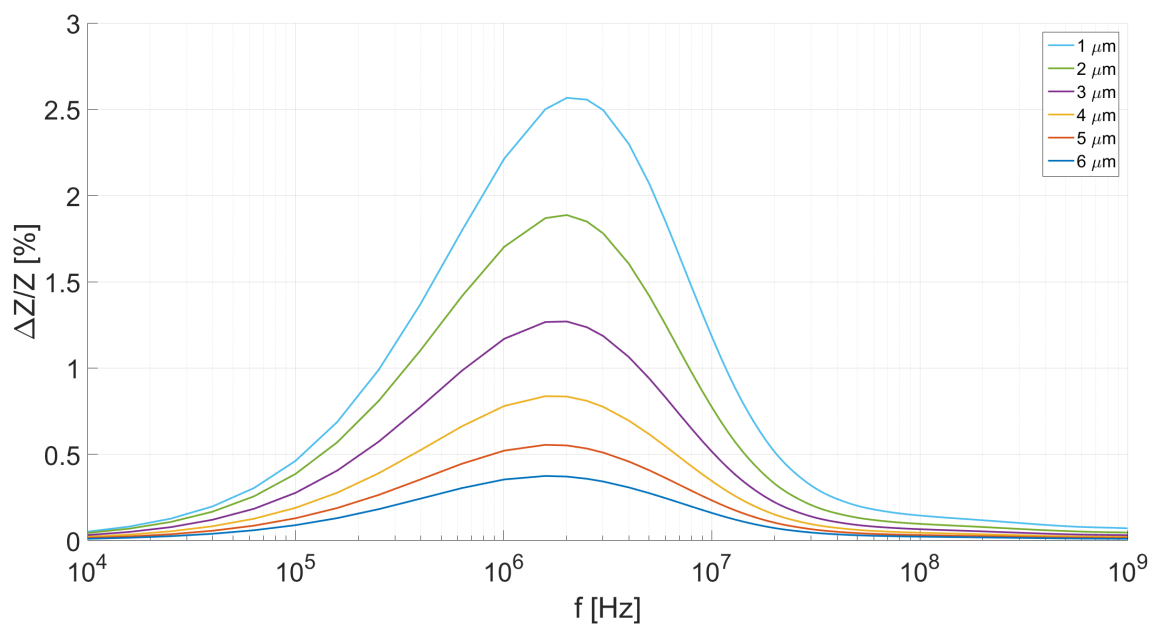
Figure 3.6: Dependence of the percentage variation $\Delta z/z$ versus electrode spacing S, considering also the double-layer capacitance contribution
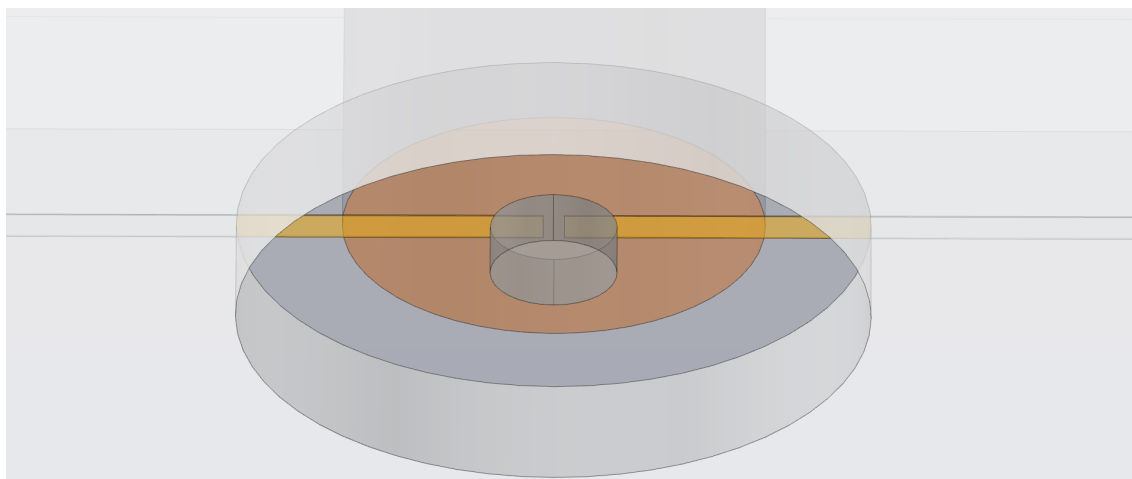
Figure 3.7: Sketch of the optimal geometry, which yields the highest sensitivity among the simulated configurations. Gold electrodes are represented in yellow, the nickel concentrator in brown, while the insulating layer (discussed in Subsection 3.4.1) is in foreground. The simulated RBC is the grey cylinder in the middle. Wirings are not visible, as electrodes protrude a lot

electrodes.

However, for alignment reasons explained in Section 4.5, it is better to leave all the concentration area uncovered.

To wire out the electrodes with a single photolithographic step, a planar structure is needed, with wirings 20-μm wide, spaced 150 μm, namely the distance between

the concentrators. The 2-μm-wide electrodes stick out by 64.5 μm, and there is a pair of them every 150 μm.

This system is more complex and the device is harder to fabricate with respect to a simple IDE configuration, but it allows the attraction of farther particles, namely about 500 μm for erythrocytes and for hemozoin crystals, instead of 50 μm like initially hypothesized. The standard silicon wafer is thick about 300–500 μm, meaning that the new structure allows bigger volumes, being area and parasitemia equal (the set limit of detection is 10 $^{iRBC}\!/_{\mu L}$).

3.3.1 Variation estimate

Considering a blood sample containing 10 iRBCs per μL, and a volume of about 500 $\mu m \times 1$ cm$\times 1$ cm for RBCs, which translates into 50 μL, there should be approximately 500 iRBCs in a blood drop. Since there is a magnetic concentrator every 150 μm along both axes, there are 66 rows and 66 columns of them, meaning a total of 4356 sensing sites. However, half of the total area is reserved as a control and the underlying particles are then lost, meaning 2178 active sites with cylinders where particles are attracted, it is therefore reasonable to consider one iRBC every 9 concentrators. Hemozoin was supposed to be insulating, so the same can be said about HCs, still taking into account a 500-μm-thick blood smear and about 20 HCs per iRBC, leading to a conservative estimate of 2 HCs per concentrator. These numbers are not definitive, but only a reasonable evaluation, as they depend also on the magnetic geometry, which is not fully defined yet.

This leads to a 5% impedance variation for the former and 0.6% for the latter, that is respectively two and one orders of magnitude greater than the first estimates without optimized geometry.

Even though iRBCs are fewer than HCs, they are greater in size, so the erythrocytes give a much bigger signal with respect to hemozoin crystals.

From an electrical point of view is then far easier to detect iRBCs, in contrast with the magnetic standpoint, which considers simpler to attract HCs. The presence of hemozoin implies also iRBCs, so both detection means can be adopted, even at the same time. This theoretically increases the impedance variation, but the two particles are so dissimilar in size and viscous properties that their attraction times are slightly different, as mentioned in Section 3.1.

It is still unclear which particle suits better the combination of magnetic attraction and electrical detection, so both ways are still under investigation.

3.3.2   Alternative geometries

Particles don't follow the expected behaviour, that is being attracted exactly in the center of the concentrators, as shown in Figure 3.2.

The optimal configuration was designed keeping in mind that prediction, which was later disproved by experimental results, discussed in Section 5.2, which in turn highlighted the fact that particles were mostly attracted to the edges of the cylindrical concentrators. Obviously, the geometry had to be adapted to the different attraction pattern, as shown in Figure 3.8a. This comes at the cost of an efficiency loss, as particles are obviously less concentrated, but it is the simplest way of monitoring every possible capture spot.
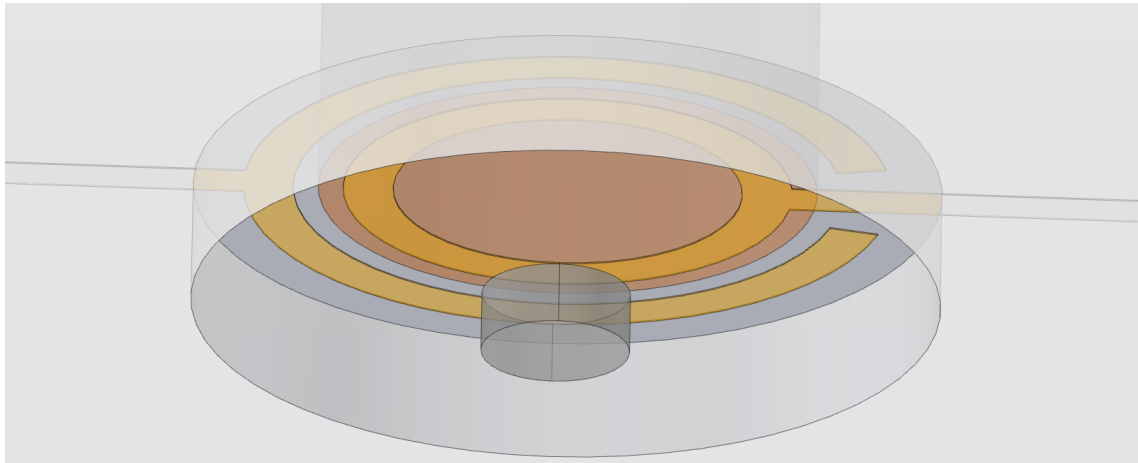
(a) Sketch of the circular geometry, used for most of the experimental tests
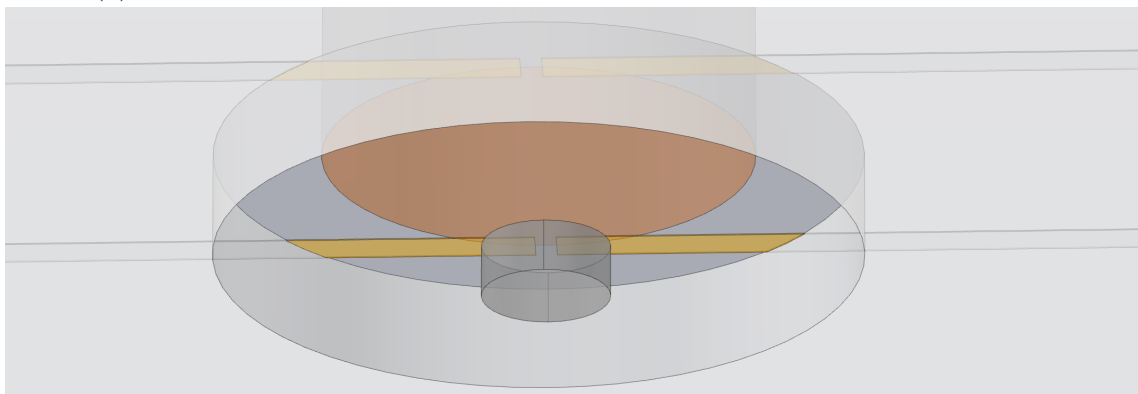
(b) Sketch of the geometry needing in-plane magnetic field to create points of attraction

Figure 3.8: New geometry configurations, designed to adapt to the experimental behaviour of the cylindrical concentrators

This was the adopted geometry for preliminary tests on a dummy device, primarily because of the simplicity of fabrication and utilization.

In order to increase the capture efficiency, a possibility is to add an *in-plane magnetic field*, which would steer the particles towards two opposite vertices of the concentrator once attracted, as illustrated in Figure 3.8b. This is still not an ideal solution, since the capture efficiency is obviously lowered, but the results given by this geometry differ from the optimum by only a factor of 2.

The setup is more complex though, for it needs an additional external magnetic field, and that is why it was not adopted during preliminary tests.

The frequency needs to be slightly adapted depending on the adopted geometry, but it remains anyway in the MHz range.

3.4   Wirings

Width and spacing of the wirings affect mainly three parameters:

- Series resistance of the wirings

- Parallel resistance of the wirings through the solution

- Capacitance through the solution

Ideally the wirings should be as far as possible from each other and quite slim, as the last two parameters are of the utmost importance and their effect vanishes rather quickly as the wirings spread out and thin out. This is not possible though, because the series resistance of the wirings would be higher than the resistance of the solution between the two electrodes. The series resistance can be estimated using Ohm's second law:

$$R = \rho \cdot \frac{L}{A} = \rho_{Au} \cdot \frac{L}{t \cdot W} \tag{3.5}$$

Where:

- ρ_{Au} = Gold resistivity $[\mu\Omega \cdot cm]$

- L = Length of the wiring $[\mu m]$

- t = Thickness of the deposited gold $[nm]$

- W = Width of the wiring $[\mu m]$

The chromium layer needed to make gold adhere to the silicon substrate can be neglected, since it is thinner than gold and it is also less conductive. Gold resistivity is $\sim 2.44 \ \mu\Omega \cdot cm$ for bulk material[83], not varying by much for sputtered thin films of 100 nm[84,85].

Their spacing has to be equal to the concentrator spacing, which depends only on the capture efficiency. Hence, the only parameter which can be acted on to reduce their series resistance is the width W, as also the thickness t is fixed.

On the other hand, L is equal to the device length, as current has to follow the path from the positive terminal, flow through the solution, and then reach the negative terminal by passing the remaining branch of the electrode. In order for the wiring series resistance to be 50 times smaller than the solution's, their width has been set to 20 μm. By reducing their width, therefore additionally separating them from each other, their resistive contribution through the solution decreases, as a consequence the frequency of the pole due to the wirings increases, but it is not sufficiently high even for 20-μm-wide wirings. In Figure 3.9 the main electrical parameters are shown.
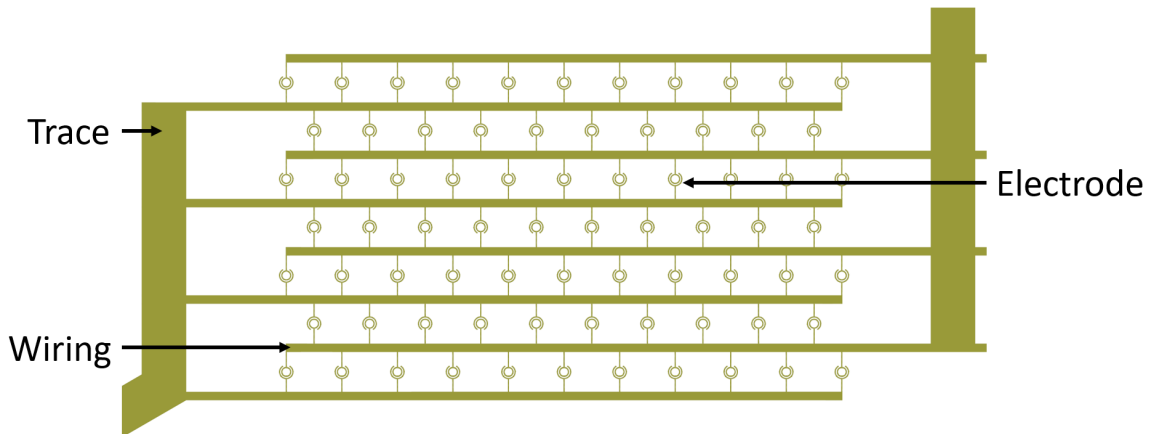
Figure 3.9: Design layout of the active area of the device, highlighting the main electrical parameters for the circular geometry shown in Figure 3.8a. On the right side there are wirings going to the reference electrode, explained in Subsection 2.3.3.

3.4.1 Insulating layer

To further decrease the wiring contributions through the solution, a thick insulating photoresist layer is required to be laid onto the entire surface of the device, leaving uncovered only the active areas over the magnetic concentrators and electrodes. In so doing, the parallel resistance becomes huge, negligible with respect to the solution.
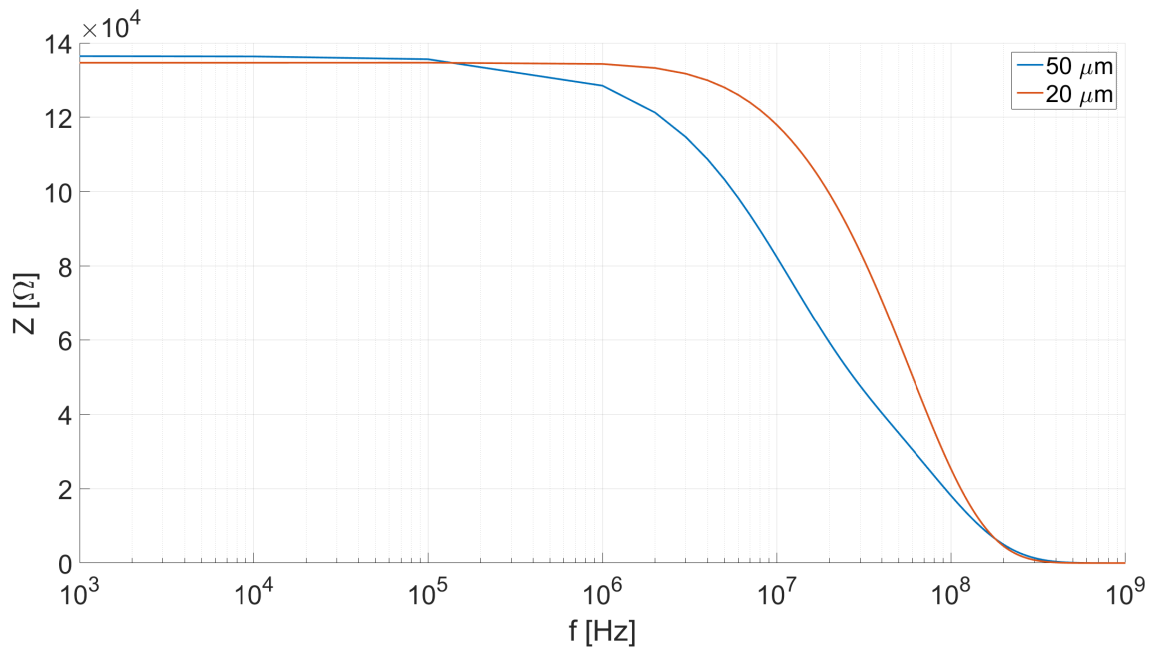
(a) Impedance of the device
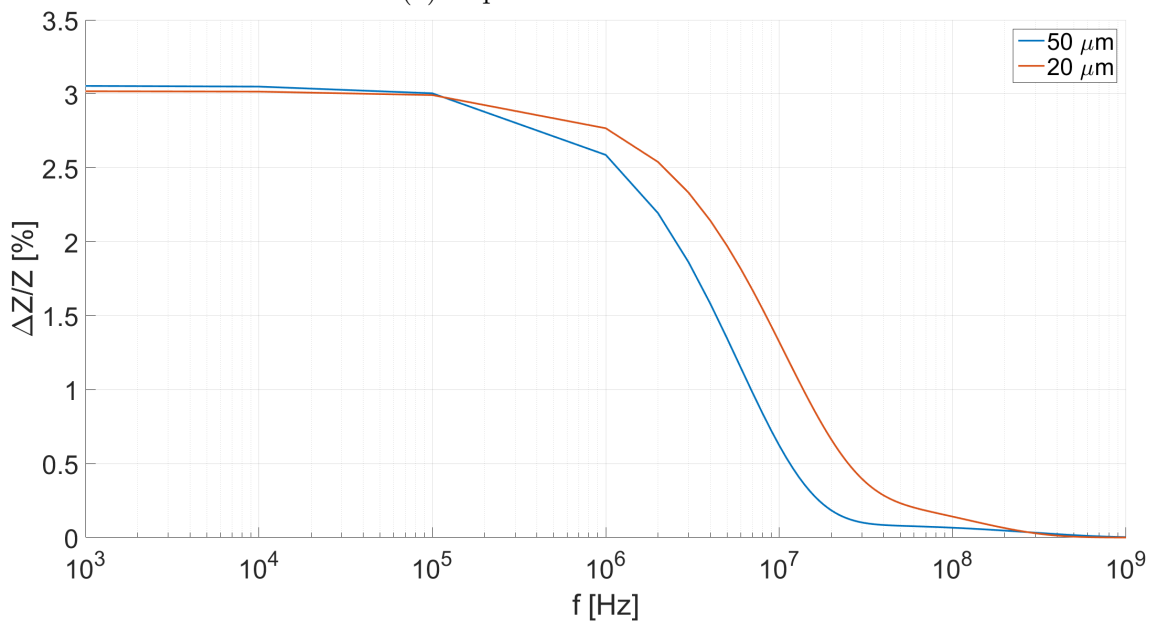
(b) Impedance variation

Figure 3.10: Reducing the width of the wirings moves the pole towards higher frequency, improving the frequency response of the device

The difference between wirings wide 50 μm and 20 μm is provided as an example in Figure 3.10a, where the double-layer has been neglected. However, in Figure 3.10b it can be noted that the impedance variation starts to have a decreasing trend before reaching 10 MHz, so it is better to keep the test frequency as low as possible.

These are only test curves though, only to show the divergence between the different configurations, so the impedance and its variation are not actual values.

There is yet another trade-off, as this layer cannot be too thick, in order for the form factor of the cavities to be rather low, which would remarkably simplify the lithography fabrication and reliability. The footprint of the electrode area is of the order of some micrometers, so the thickness of the insulating layer has to be accordingly set to a few microns. This layer can be made of either SiO_2 or SU-8 photoresist.

During experimental tests SU-8 was used, to simplify and speed up the fabrication process, but SiO_2 is also a viable solution, less affected by temperature stress for example. However, it is harder and more expensive to grow silicon dioxide than to deposit SU-8, so the latter is the better choice overall, as it can be 5-μm thick, or even more. According to Equation (2.28), it is better to have a thicker dielectric layer, in order to obtain a smaller capacitance, resulting in a pole at higher frequency.
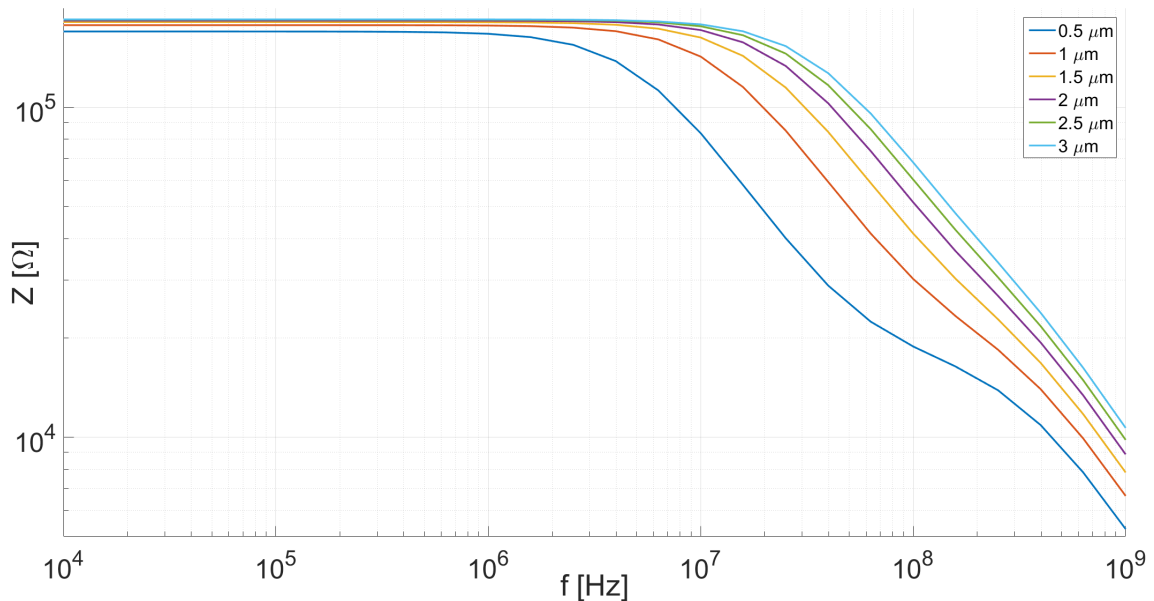
Figure 3.11: Impedance dependence as the insulating layer thickens, not taking into account the double-layer capacitance

It can be noted in Figure 3.11 that the pole moves towards high frequency by about a factor of 6 while the thickness increases accordingly, as a result of the capacitance relation mentioned in Equation (2.28).

Another very important conclusion that can be drawn from Figure 3.11 is that curves don't maintain the same shape as thickness increases. This is due to the

fact that with a photoresist thickness of 0.5 μm two capacitive contributions are visible, namely C_{wir} and C_{ins}, which are the capacitance of the wirings through the solution and the capacitance related to the insulating layer, respectively. As the thickness increases over 1.5 μm, its effect fades with respect to C_{wir}, and it eventually becomes absolutely negligible, for example with a 3-μm-thick layer. Moreover, the resemblance of a resistive plateau visible at about 100 MHz is the resistance of the wirings through the solution once the pole of the insulating layer occurred.

Further thickening the insulating layer is not expected to enhance by much the frequency response of the device, as the pole would be higher than the required 10 MHz in any case. 5 μm is the minimum thickness that can be laid down with SU-8 photoresist, as clarified in Section 4.5, which is more than enough. The R_{sol} value reported in this graph is about 180 $k\Omega$, as for complexity issues only one sensing site was simulated. This value needs to be divided by the total number of active sites (2178), and it still is an approximate value, as the goal of this simulation was to highlight the advantages of the insulating layer. Yet, 82 Ω is pretty close to the expected value of the device nominal plateau resistance, to be validated during experimental tests.

The total area of the wirings affects also the substrate capacitance, covered in Subsection 2.3.1, but it is negligible with respect to the effects presented here, and it introduces a smaller effect than pads for example. Since the capacitance is related to the gold area deposited on the silicon substrate, even wider traces, which connect the wirings to the pads, contribute a lot more than wirings and electrodes.

Chapter 4

Device fabrication

4.1 Fabrication environment

All the processes used for the realization of the device were conducted at PoliFab, a cleanroom facility property of Politecnico di Milano.

A cleanroom is an environment characterized by a low level of environmental pollutants like dust, airborne microbes, chemical vapours, and aerosol particles, typically used in manufacturing of semiconductor devices and pharmaceutical products, as well as food industry applications. A cleanroom has a controlled level of air quality and temperature, so as to allow controlled and extremely precise fabrication processes.

Cleanroom classification is based on the number and size of particles permitted per air volume, according to ISO 14644-1, a non-governmental standard developed by the International Organization for Standardization, summed up in Table 4.1[86].

The air entering a cleanroom is filtered to keep out dust and contaminants, and the air inside is continuously recirculated through high-efficiency particulate air (HEPA) or ultra-low particulate air (ULPA) filters, in order to eject internally generated dust, sometimes using both HEPA and ULPA filters for higher efficiency.

Staff must enter and leave through airlocks (sometimes including an air shower stage), and wear protective vestures like hoods, face masks, gloves, boots, and coveralls. For these reasons, it is usually forbidden to bring paper, pencils, and natural fibers fabrics inside a cleanroom, and alternatives are given (e.g. cleanroom paper, that is a special paper designed to minimize deterioration and dust creation). Also internal equipment is designed to minimize the generated air contamination.

PoliFab includes a 370 m² cleanroom, which provides fast device prototyping for

Class	Maximum particles per m³					
	$\geq 0.1\,\mu m$	$\geq 0.2\,\mu m$	$\geq 0.3\,\mu m$	$\geq 0.5\,\mu m$	$\geq 1\,\mu m$	$\geq 5\,\mu m$
ISO 01	10	N/A	N/A	N/A	N/A	N/A
ISO 02	100	24	10	N/A	N/A	N/A
ISO 03	1000	237	102	35	N/A	N/A
ISO 04	10 000	2370	1020	352	83	N/A
ISO 05	100 000	23 700	10 200	3520	832	N/A
ISO 06	1 000 000	237 000	102 000	35 200	8320	293
ISO 07	N/A	N/A	N/A	352 000	83 200	2930
ISO 08	N/A	N/A	N/A	3 520 000	832 000	29 300
ISO 09	N/A	N/A	N/A	35 200 000	8 320 000	293 000

Table 4.1: A short recap of the different ISO classes of a cleanroom

innovative designs, mainly for photonics, microfluidics, micromechanics, spintronics, and electronic devices[87]. It is divided in two contiguous areas, namely a 220 m^2 ISO 08 grey area, and a 150 m^2 ISO 06 white area.

4.2 Fabrication overview

The fabrication of this multi-layer device, possible through numerous production steps, can be split in two macro-processes, each one regarding a specific device layer: the underlying macro-layer concerns magnetic attraction, while the above one is needed for electrical detection. Every process step must be accomplished with the so-called *planar process*[88], widely used in the semiconductor industry, whose key concept is to view a device as a layered two-dimensional plane, each layer representing a step.

The macro-layers must be electrically isolated, and the magnetic layer acts as a substrate for the electrical one, since the latter is fabricated right on top of the former.

First of all, a 1-μm SiO₂ layer needs to be deposited on a 6-inch silicon wafer, so to avoid electrical connection with the conductive silicon substrate itself. This process is carried out with STS Multiplex, which employs plasma-enhanced chemical vapour deposition (PECVD).

The next procedure is wafer cutting, to easily handle roughly 2 $cm \times 2\ cm$ samples instead of a full 6-inch wafer. Besides, from a process optimization standpoint, it is considerably more convenient to have a lot of samples to try the process on.

Then the construction of the magnetic layer is needed. This involves lithography

to create a mask of the magnetic geometry described in Section 3.1, reactive ion etching to bore apertures in the sample, and subsequent deposition of the nickel pillars, which can either be evaporated or electroplated on the substrate. Evaporation is not ideal for this kind of structures, as after a thickness of 100–150 nm the evaporated material is structurally unstable and starts to peel off, so electroplating was chosen.

Then another 1-μm-thick SiO_2 capping layer is deposited, again with STS Multiplex, to both insulate the different structures and to have a planar substrate for the upper layers.

The second-to-last process is the electrode deposition, preceded obviously by photolithography. The electrodes are made of a sputtered 30-nm chrome layer and of 100 nm of gold on top of it, which constitutes the actual electrodes. The whole surface is to be covered by a SU-8 photoresist coat, with holes just in correspondence of the electrodes, on both active and reference area.

The electrodes are finally bonded to a PCB board, which provides connections to the external world, and the signal given by the electrodes can be read by a commercial or custom lock-in amplifier.

4.3 Magnetic layer

4.3.1 Reactive ion etching

Reactive ion etching (RIE) is needed to dig an array of 20-μm-thick cylindrical holes in the wafers, so that nickel concentrators can be electroplated inside them. RIE employs chemically reactive plasma to remove materials deposited on silicon wafers, like SiO_2 or silicon itself.

The plasma is generated under vacuum by an electromagnetic field, then highly energetic ions from the plasma impact the wafer surface and react with it. It is therefore categorized as a dry etching technology.

In inductively coupled plasma (ICP) type of systems, the plasma is generated with an RF-powered magnetic field. Very high plasma densities can be achieved, though etch profiles tend to be more isotropic.

Differently from wet etching techniques, RIE is considerably directional. This property is useful to etch only in the vertical axis, allowing very sharp edges. Nevertheless, being the ions *reactive*, the smoothness of the surfaces is increased with respect to a pure physical etching, as ions also chemically etch the substrate, making

this process kind of a hybrid technology.

The substrate mask was made of AZ40XT positive photoresist[89], and the etching process was performed at INPHOTEC. The depth of the holes was constant (20 μm), while diameter and spacing weren't. The diameters of the cylinders were 20 μm, 30 μm, and 40 μm, and the center-to-center spacings respectively 60 μm, 80 μm, and 160 μm.

As mentioned, RIE is a hybrid process, and it etches different materials at different rates, in fact while the etched holes in the silicon are 20-μm deep, the AZ40XT photoresist is evenly etched by only 5 μm.

4.3.2 Electroplating

Electrochemical deposition, also known as *electroplating*, is a growth process involving the formation of a metallic coat onto a substrate, occurring through electrochemical reduction of metal ions in solution. Its working principle is depicted in Figure 4.1.
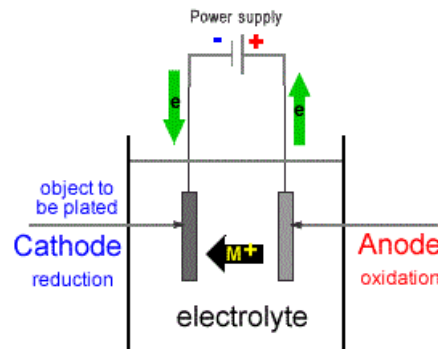
Figure 4.1: Working principle of the electroplating process[90]

An electrolytic cell is needed to drive the non-spontaneous redox reaction, by means of a certain amount of electrical energy (current), similar to a reverse galvanic cell. The working (cathode) and counter (anode) electrodes are immersed in an electrolyte solution, whose high conductivity is given by the presence of positive and negative ions. After a positive voltage is applied to the terminals, the negative ions tend to migrate towards the anode, and conversely the positive ions are drawn to the cathode. At the cathode-solution interface, the metal ions are reduced to metal atoms, eventually coating the surface. The anode, on the other hand, can provide ions by dissolution, due to oxidation of its atoms. Alternatively, ions can be supplied by the solution itself, given that metal salts are externally dissolved in it.

In this case, the solution must be progressively replenished as ions deposit on the substrate[91].

Standard electroplating uses direct currents, but in *pulse platings*, alternate currents are involved. The power supply applies short current pulses, usually in the range of 500–10 000 Hz, which favour the formation of grain nuclei and increases the total number of grains per unit area. This results in overall improved properties with respect to conventional electroplated films, such as better distribution, lower porosity, higher uniformity, higher hardness, and less metal usage[92].

The quality of the plated material is crucial, and so is its thickness, as in this process the concentrators must barely fill up the etched holes to create a planar surface.

The material thickness T is regulated by the following equation[91]:

$$T = \frac{A}{n \cdot F \cdot \rho} \cdot \frac{I \cdot t}{S} = B \cdot \frac{I \cdot t}{S} \qquad (4.1)$$

Where:

- A = Atomic weight of the material $\left[\dfrac{g}{mol} \right]$

- n = Valence of the dissolved metal in the solution $\left[\dfrac{1}{mol} \right]$

- F = Faraday constant $\left(96485.309 \left[\dfrac{C}{mol} \right] \right)$

- ρ = Material density $\left[\dfrac{g}{cm^3} \right]$

- I = Current $[A]$

- t = Plating time $[s]$

- S = Surface area $[cm^2]$

For a defined material reaction, the first term B remains constant, and only current and time can be optimized.

Given that the nickel structures are, relatively speaking, quite big, the planarization must be remarkably effective. As mentioned before, a planar surface is fundamental for the subsequent fabrication of the electric layer, forcing this procedure to be extremely precise, accurate, and reproducible. A full 20-μm planarization, needed in a situation like the one reported in Figure 4.2, is quite complex from a
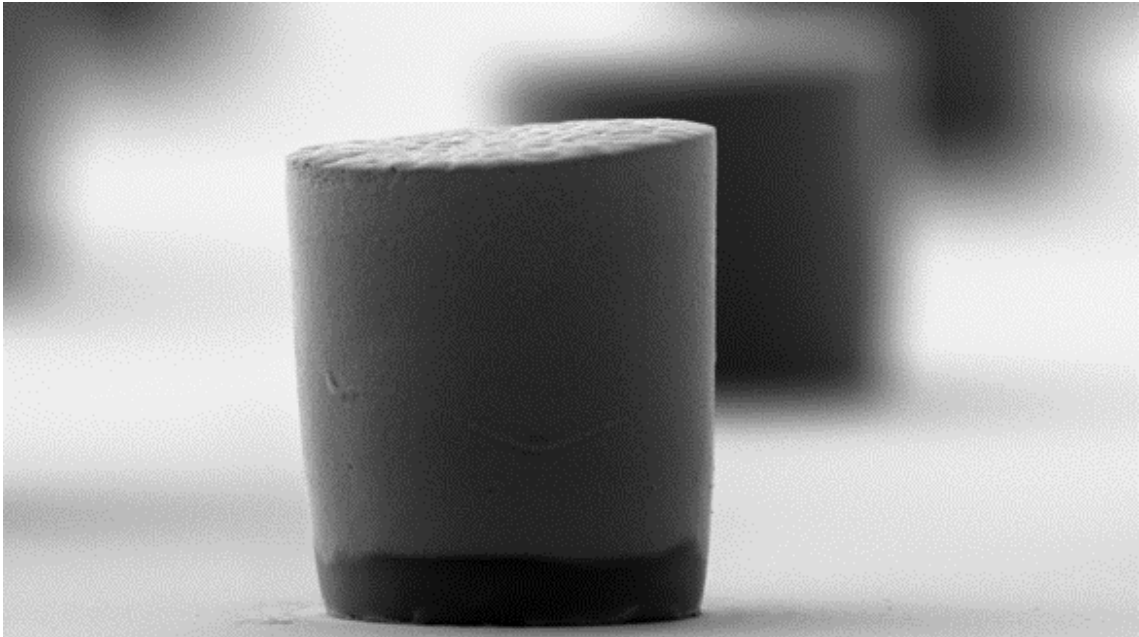
Figure 4.2: SEM image of a sample with nickel electroplated directly on a *seed layer* after the deposition of a resist mask (that is without RIE) and subsequent lift-off. A seed layer is a nickel thin film deposited on the sample, to enhance electroplating properties

fabrication standpoint. Various techniques were considered, such as planarization with photoresist[93,94], polymers[95], plasma[96], or chemical-mechanical planarization (CMP)[97], but these kind of processes require multiple steps to have a sufficiently planar surface.
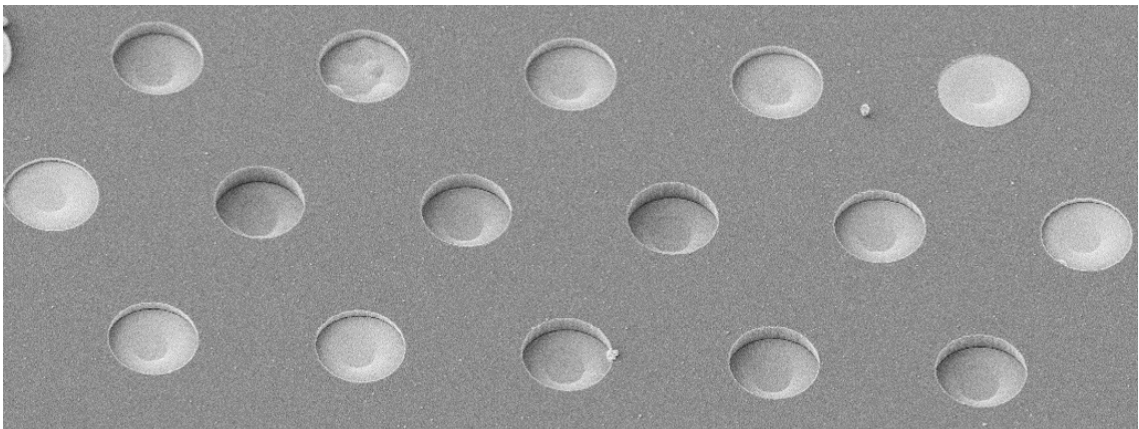
Figure 4.3: SEM image of the magnetic pattern, in which some etched holes are not completely filled by nickel

For these reasons, RIE was the preferred process to grow nickel concentrators.

The electroplated pillars and the substrate are still not perfectly even (shown in Figure 4.3), so a SiO$_2$ capping layer is necessary to help having a flat surface. However, from a fabrication standpoint, this procedure is fairly effortless with respect to a full 20-μm planarization.

4.4 Electric layer

4.4.1 Photolithography

Photolithography is the main fabrication step for the realization of the electrodes, for it allows the exposition of a pattern on mainly silicon or glass substrates[98].

Before the actual lithography process, sample preparation is mandatory to remove possible dust on the sample itself, as it would be detrimental for the success of the exposition. It is therefore necessary to clean the sample with acetone and isopropanol (IPA), lightly polishing it with a wiper cloth. As mentioned in Subsection 2.3.1, both silicon and glass substrates were fabricated. To ensure the actual cleanness of a glass slide it is recommended to clean and polish both sides of it.

Sample preparation for glass also involves the deposition of the so-called adhesion promoter, necessary to enhance the resist grip to the substrate. The MicroChemicals Ti-Prime Primer has to be deposited on the sample through a procedure known as *spincoating* (Figure 4.4), which requires a spinning treatment. On Karl Süss Spin Coater RC8, for example, the sample needs to be spinned at 4500 RPM for 45 s, and then placed on Sawatec Hotplate HP401 to be baked at 120°C for 120 s[99].
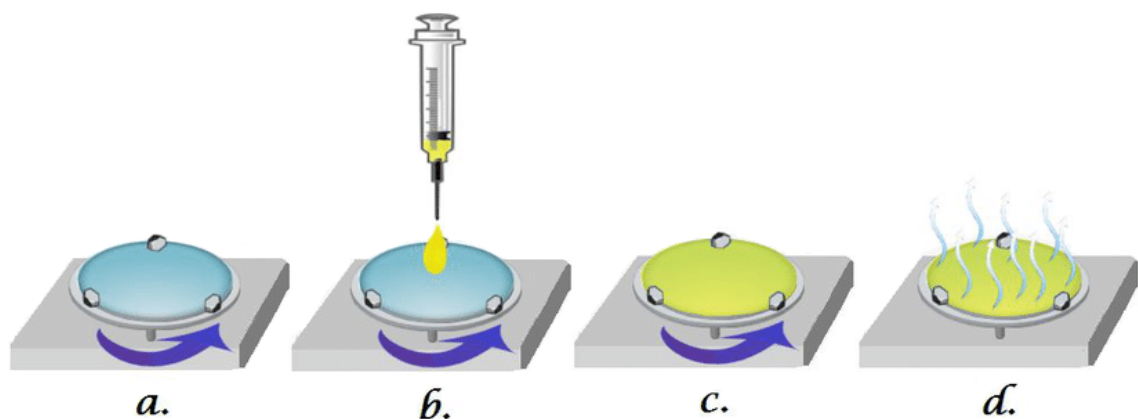
Figure 4.4: a. Placement of the sample on the spincoater   b. Deployment of the liquid photoresist or primer   c. Spinning phase, the liquid reaches the desired thickness   d. Evaporation of the solvent, facilitated by employing a hotplate[100]

This procedure is suggested also for silicon samples if the structures are really tiny, in order to enhance the photoresist adhesion, avoiding then the detachment of micrometric features.

The next step involves the deposition of MicroChem AZ5214e photoresist, employing once again the Spin Coater at 6000 RPM for 60 s, in order to have a 1.4-μm-thick layer and then facilitate the solvent evaporation by means of a 110°C bake for 100 s[101]. Polishing the back side of the glass slide is an astute expedient, as resist leftovers may obstruct the view of the exposed pattern.

It is essential to avoid bubbles forming inside the photoresist during deposition and bake, thus being recommended to heat the sample up following a temperature gradient, for example at 60°C first, and then at the proper baking temperature.
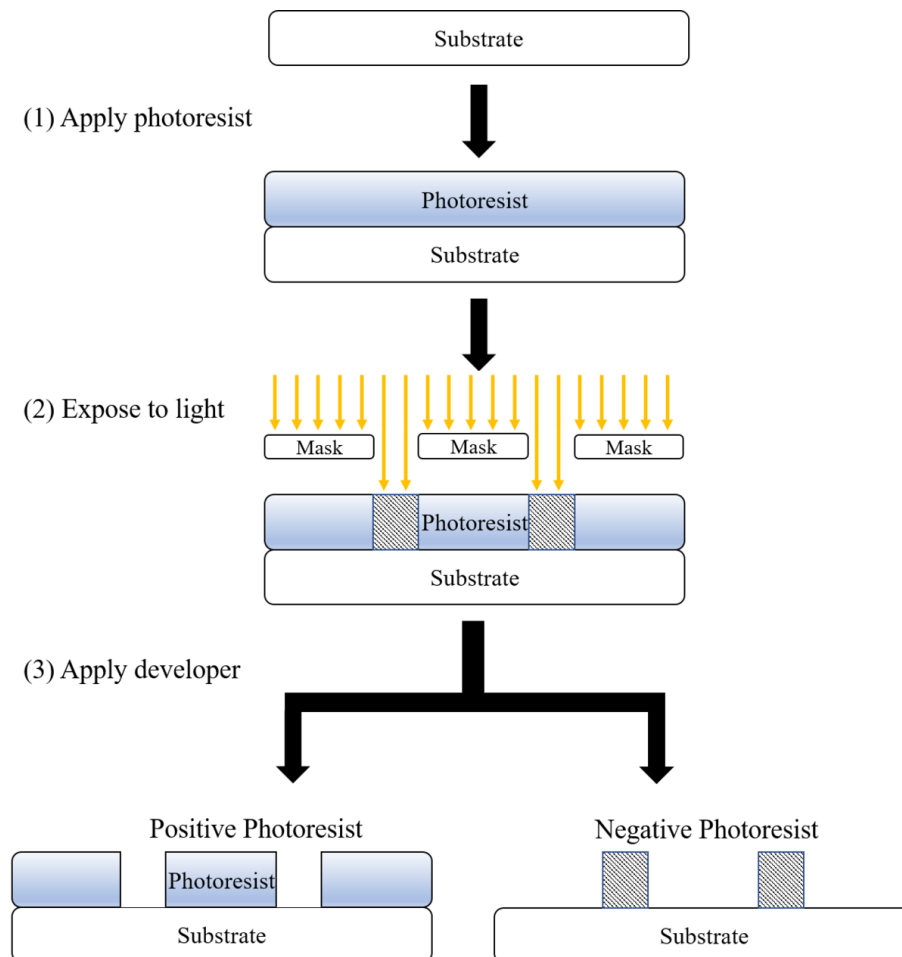
Figure 4.5: Main steps of positive and negative photolithography: (1) Photoresist application, needs to be spincoated   (2) Exposition phase, achieved with mask or maskless exposure   (3) Development stage, with clear differences between positive and negative photoresist[102]

The ensuing step is the actual lithography, shown in Figure 4.5, fulfilled with Karl Süss Mask Aligner MA6/BA8, and it consist in placing an optically insulating mask over the sample, and selectively exposing the photosensitive resist to ultraviolet light:

- In positive photolithography the exposed resist is weakened and then easily removable

- With a negative resist, after the so-called *reversal bake* the exposed part cross-links with the substrate and is hardened with respect to the non-exposed section, and the removed pattern is therefore the latter[98]

The correct exposure dose is 29 $\mathrm{mJ/cm^2}$ for positive photolithography of AZ5214e, and 23 $\mathrm{mJ/cm^2}$ for the negative procedure. The lamp of the mask aligner gives a power of 5.1 $\mathrm{mW/cm^2}$, so the sample must be exposed for 5.7 s and 4.5 s respectively.

Due to absorption of the photoactive compound (PAC), which attenuates the light during the exposure phase (so-called *bulk effect*), positive photolithography yields structures with positive slopes of 75°–85°, which make it not ideally suited for lift-off[101]. Slopes are reversed in negative photolithography, since the exposed resist remains on the sample[98,103].

A possible variation consists of employing a different kind of lithography, known as maskless, since it doesn't involve an insulating mask, but a laser ray directly exposes the photoresist, as illustrated in Figure 4.6.

The used equipment is Heidelberg MaskLess Aligner MLA100, which illuminates the substrate without contacting or touching it whatsoever, diminishing the possibility of scratching or damaging the sample.

Another advantage of this technique is to overcome some intrinsic limitations of the mask lithography, namely the chance to import the desired pattern from an AutoCAD drawing, so not to wait for an external company to physically fabricate the mask, or also the possibility of sweeping the exposure parameters, especially useful to develop the best recipe while optimizing the process[104].

The correct exposure dose for negative AZ5214e is 32 $\mathrm{mJ/cm^2}$, given by the internal laser of the maskless aligner. This dose is not a true energy value though, as it is handled internally by the machine. Nonetheless, this value gives an approximate idea of the energy furnished to the resist.

The MLA100 exposes the section of the resist that will not be removed during the development, meaning it performs a negative lithography, which requires a reversal
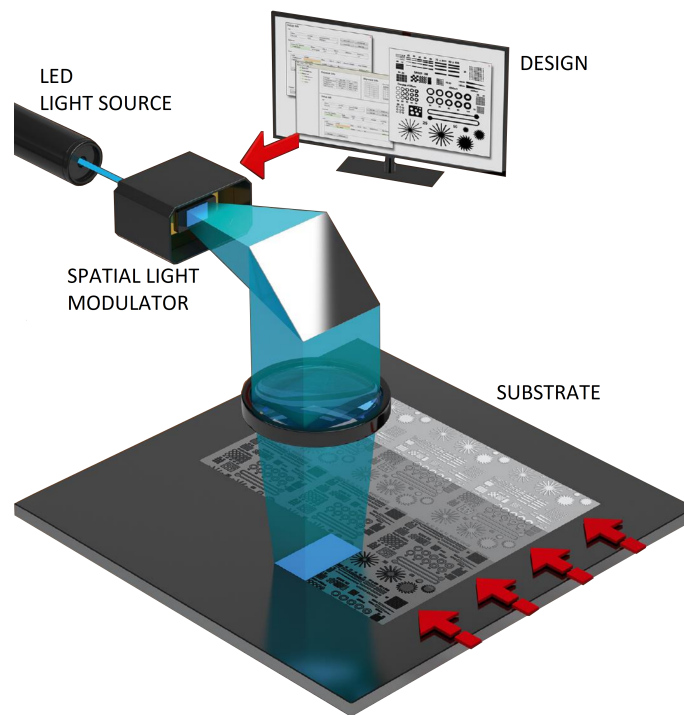
Figure 4.6: Working principle of a maskless photolithographic process, in which a design is promptly loaded on the machine, without turning to an external company[104]

bake at 115°C for 90 s, to supply the necessary energy for the resist to cross-link. Reversal bake temperature is the most critical parameter, and once optimized it must stay ±1°C within the optimal one[101].

Then, a 90 s flood exposure is needed to weaken the non-cross-linked resist, carried out by means of the lamp test program of Karl Süss Mask Aligner MA6/BA8. Flood exposure is needed to apply sufficient energy for the unexposed area to become soluble to the developer. While it is not a critical step at all, about 150–500 $^{mJ}/_{cm^2}$ must be supplied to the sample[101].

The last lithographic step is the development, that is the immersion and mild agitation of the sample in AZ726MIF Developer for about 30 s, when all the weakened resist should have come off. The sample has to be washed with deionized (DI) water afterwards. This process has to be repeated until all the pattern is resist-free, but one has to be keen not to overdevelop the structures, and that is why this is a critical step too. Overdeveloped resist usually causes blunt edges and structural yielding, while underdeveloping a sample may result in undesired resist or structures with unexpected width.

4.4.2 Sputtering

After an optical verification of the lithography success, possibly even with KLA Tencor P-15 Profiler, gold deposition takes place.

The employed technique is known as *sputtering*[105,106], carried out with Magnetron Sputtering System Leybold LH Z400.
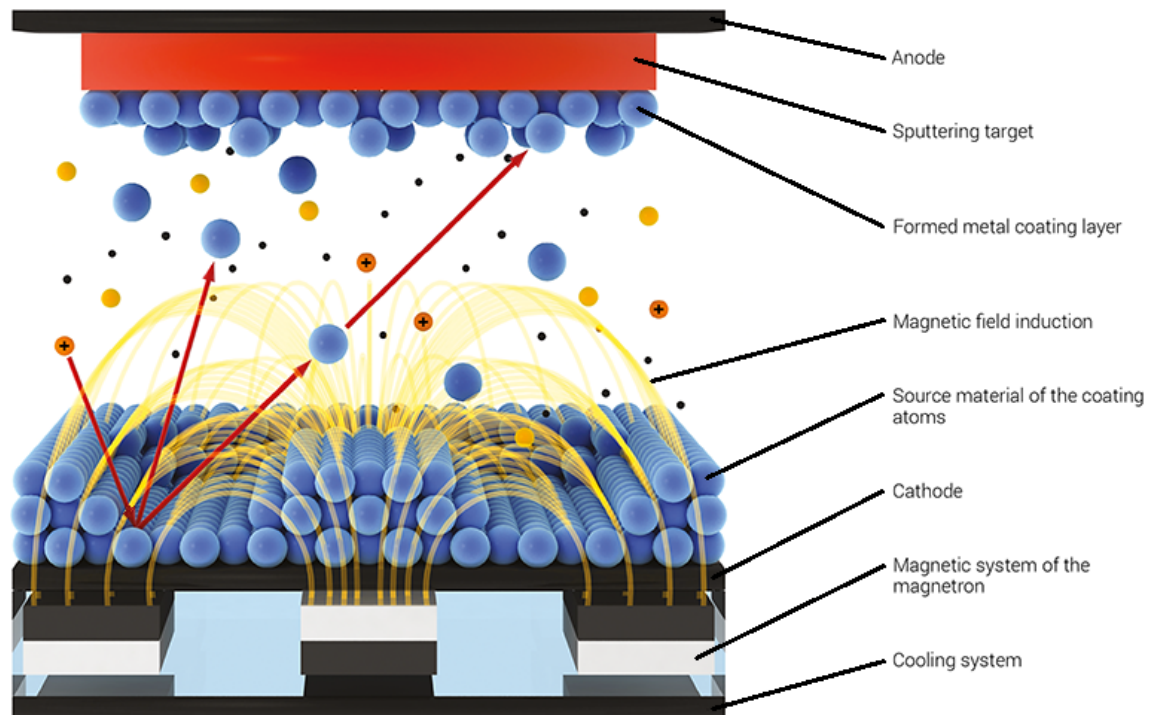
Figure 4.7: Working principle of a magnetron sputtering system. The Ar$^+$ ions are visible in orange[107]

Magnetron sputtering[106,108], whose working principle is displayed in Figure 4.7, is a physical vapour deposition technique, which allows a good film adhesion to the substrate, and a high control on the thickness, uniformity and composition of the deposited material[87].

By first creating a gaseous *plasma* and then accelerating the ions from this plasma into some source material, said material is eroded by the arriving ions via energy transfer and is ejected in the form of neutral particles, either individual atoms, clusters of atoms or molecules. As these neutral particles are ejected, they will travel in a straight line unless they come into contact with something, namely other particles or a nearby surface.

If a target such as a silicon wafer is placed in the path of these ejected particles, it will be coated by a thin film of the source material.

In order to create the plasma, atoms of an inert gas (frequently argon) are introduced into the high vacuum (HV) chamber and a negative bias voltage is applied to the source. Free electrons are immediately accelerated by the electric field in proximity to the source material and ionize by collision the argon atoms leaving Ar^+ ions. This cascade process ignites the plasma. At this point, positively charged Ar^+ ions are accelerated towards the negatively biased electrode, striking the surface and releasing source material and more free electrons by energy transfer.

In magnetron sputtering, permanent magnets are located behind the cathode in order to confine the free electrons by means of a magnetic field directly above the source material surface[108]. This provides a two-fold advantage: on the one hand the free electrons, which are rejected by the negatively charged cathode, are prevented from bombarding the target, which would cause overheating and structural damage, on the other hand the circuitous path carved by the free electrons along the lines of the magnetic field enhances the probability of ionizing neutral argon atoms by several orders of magnitude. The increased ion availability significantly boosts the rate at which the source material is eroded and subsequently deposited onto the target.

Before the sputtering operation, it is suggested to prepare the sample by breaking its surface bonds and improve chrome adhesion to the substrate[109,110], by means of Plasma Asher PVA Tepla 200, in which 200 W for 8 minutes should suffice. Another advantage of the plasma treatment is to remove organic materials, like resist residuals, from the pattern.

In this process, monoatomic oxygen plasma is created by exposing oxygen gas at a low pressure (typically 0.5–1.5 mbar) to high power radio waves, which ionize it. This operation is performed under vacuum and it leads to formation of plasma in the chamber. As the plasma is formed, many free radicals are created, and used to strip the first atomic layers away from the sample surface[109].

At this point, one must be quick to transfer the samples inside the HV chamber of the Magnetron Sputtering System, in order not to let the substrate's dangling bonds react with air.

The following step is to rough pump the chamber, so as to reach a sufficient vacuum level, and only then turn on the turbo pump, which brings the chamber vacuum down to $\sim 2 \cdot 10^{-5}$ mbar in about an hour. After that, the actual sputtering operation begins.

First of all, a 30-nm chrome layer has to be deposited, so that 100 nm of gold can adhere to the silicon or glass substrate. To do so, it is recommended to remove the

first oxidized chrome layer from the target through a preliminary operation, in which no target is present, called pre-sputtering, therefore depositing pure chrome on the target. The argon flow during chrome sputtering is 70 standard cubic centimeters per minute (SCCM), which corresponds to 20 nm per minute, so the sample must be left over the chrome target for exactly 1 minute and 20 seconds.

The argon rate for gold deposition is 50 SCCM instead, which translates into 26 nm per minute, needing then a 4 minutes deposition to get the desired 100 nm.

Since the sputtering process is not selective, the sample now appears as fully coated with gold, with only a glimpse of the exposed pattern.

4.4.3   Lift-off

The undesired metal sections are now to be removed, by means of the so-called lift-off.

Since the chrome clings to the underlying material, being substrate or photoresist, the obvious thing to do is dissolving the resist, leaving only the substrate-adhered chrome and gold, that is the pattern. The resist can be melted by either generic chemical solvents like acetone[111], or by specific products, such as AZ100 Remover.

The first step is the immersion of the sample in acetone for 15 minutes, roughly dissolving most of the resist, which will leave chrome-gold flakes in the beaker. The acetone must therefore be replaced with clean one, and the beaker emptied and cleaned, as flakes may deposit on the patterns, creating dangerous short-circuits, in which case the electrodes can oftentimes be useless. To prevent this from happening, the sample should never dry off, and must be carefully immersed in isopropanol while replacing acetone.

Afterwards, to facilitate the process, low-power ultrasound waves can be employed, being careful not to increase the power too much, for the structures may crumble or even collapse. Another 15 minutes in acetone should be enough to remove all the resist, but it is a good habit to verify the lift-off success by means of an optical microscope, and repeat the process again if needed, until all the resist hasn't come off.

When the sample is completely resist-free, it can be washed with IPA and dried with nitrogen, it can finally be put into a Petri dish, to avoid dust contamination.

4.5   Insulating layer

The process for the fabrication of the second layer, made of SU-8 2005 photoresist, consists just of a single photolithographic step.

MicroChem SU-8 2005 is a high contrast, epoxy-based photoresist, capable of producing high-aspect-ratio structures, particularly suited for permanent applications[103,112–114]. Its adhesion to a silicon substrate is decent, so it does not need an adhesion promoter, so the first step, after cleaning the sample, is to spincoat the SU-8 at 4000 RPM for 30 s. For our purposes, 5 μm is more than enough (Figure 4.8), so this spin speed was chosen to have a more uniform layer.
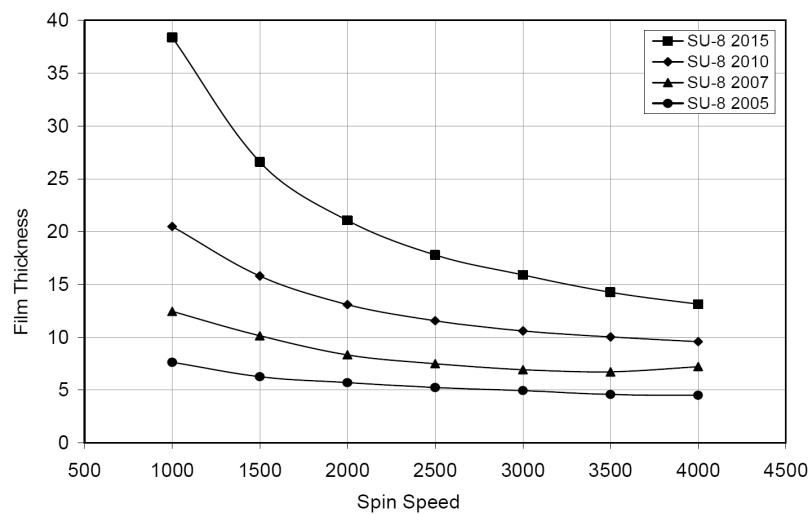
Figure 4.8: Expected thickness of spincoated SU-8. Spin speed is expressed in RPM, while film thickness in μm. The first two digits of the rightmost number represent the photoresist series, while the latter digits give an idea of the thickness obtainable with the resist[112]

It is recommended to bake the sample on a hotplate, as in a convection oven a skin may form on the resist, and the evolution of the solvent can be inhibited. To optimize the heating conditions, it is suggested to bake the sample for a few minutes, let it cool down to room temperature, and re-heat it until the film does not show wrinkles on it. For this device, a 3-minute bake at 95°C is sufficient to let the whole solvent dry out.

During exposure with the MLA 100, the optimal dose for this structures is 700 $^{mJ}/_{cm^2}$ for silicon substrates, and 1200 $^{mJ}/_{cm^2}$ for glass.

An *alignment* procedure is required, as the SU-8 holes must be right on the electrodes. The MLA 100 guarantees an alignment tolerance of 500 nm along both

axes, but the error can be higher, as the alignment procedure must be done man-
ually by exploiting its internal camera. Since a multi-layer device can easily result
misaligned by several micrometers, it is wise to take some additional tolerance into
account in the design phase.

A post-exposure bake at 95°C for 2 minutes is then needed to give the resist the
necessary energy for substrate cross-linking. After this bake, it is recommended to
let the substrate cool down gradually to room temperature, as thermal shocks may
structurally damage the pattern[114].

The development phase is peculiar, it differs from the one of AZ5214e for exam-
ple, since it is not needed to develop the resist for a specific amount of time. The
procedure includes an actual few-seconds-development phase in SU-8 Developer[112],
then the sample has to be washed with IPA, and then developed again if it shows a
white film due to underdeveloped (unexposed) photoresist. This operation must be
repeated until the white film is not produced anymore, and then the sample is to
be rinsed with isopropanol and dried with nitrogen.

A hard bake is suggested if the device has to be thermally treated later on, at a
temperature at least 10°C higher than the maximum expected operating tempera-
ture[112,114]. Since during the bonding of the tank for the solution a bake at 90°C is
expected, it was decided to hard bake the SU-8 layer at 115°C for 2 minutes.

Once the second layer is deposited, the device looks like the one shown in Fig-
ure 4.9.

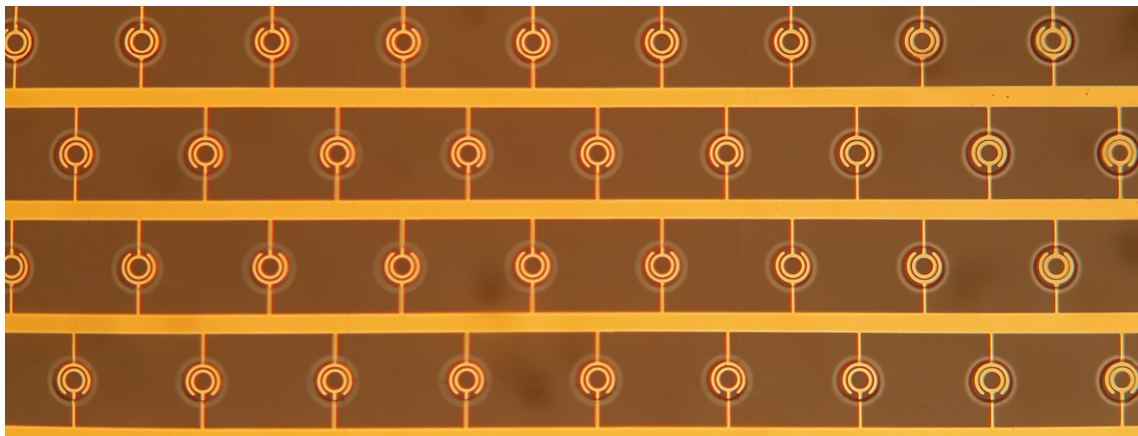
Figure 4.9: Microscopy image of the electrodes on a silicon substrate after the
deposition of the SU-8 layer, whose holes are visible in white around the electrodes.
The adopted period structure was hexagonal close packet (HCP), which is similar to
honeycomb structure, but has also an element in the center. It was chosen because
the concentrators have a higher density, to have less blind spots

4.6 Additional operations

4.6.1 PDMS bonding

A tank to contain the solution during experimental tests is necessary, polydimethyl-siloxane (PDMS) was chosen. It belongs to a group of polymeric organosilicon compounds that are commonly referred to as silicones[115,116].

PDMS is the most widely used silicon-based organic polymer, particularly known for its unusual rheological properties, and it is optically transparent, inert, non-toxic, and non-flammable[115].

Dow Corning Sylgard 184 PDMS is obtained from a base and a curing agent, which need to be mixed in a disposable container with a 10 to 1 ratio, respectively. To have a planar surface it is then suggested to pour the mixture onto a silicon piece with aluminium foil walls[116]. A huge number of undesired bubbles is inevitably present inside the PDMS, and they need to be removed by putting the whole object into a vacuum chamber for about a half hour, depending on the polymer thickness.

The result is a uniform and parallelepiped-shaped PDMS chunk, some millime-ters thick, with a perfectly flat surface. In order to solidify, it has to be baked in an oven at 85°C for about 30 minutes.

The block is therefore ready for cutting and punching. With a single piece of silicon several tanks can be usually produced, as they need to be quite small (about $1\,cm \times 1\,cm$), to fit the area amidst the pads without covering them. The tanks must not be flipped, as the perfectly flat side has to be bonded to the substrate and it's easy to misidentify the two sides.

The bonding can be carried out in two different ways:

- Preparing some additional PDMS (3 to 1 ratio), spreading it on the tank surface and gluing it to the substrate, baking the sample afterwards

- Plasma bonding the two objects, namely substrate and PDMS tank

In both cases it is needed for the hole to be exactly onto the active electrodes area, and the tank must not cover the pads or the wirings needed for the gold bonding process.

The latter method is better in terms of cleanness, required time, and structural stability, and it was therefore chosen. PVA Tepla 200 was used for this step, with a power of 50 W for 30 s[109,116]. Once the process is finished, one must be very quick

to place the PDMS tank onto the substrate, applying a moderate pressure on in, so as to bond them permanently.

A ~90°C cure for 20–30 minutes is recommended[117] to increase the effectiveness of the bonding.

4.6.2 Contacts

There are basically three different ways to contact the device to read the signal.

The first one consists of connecting the gold through a *probe station*, like SÜSS MicroTec Manual Electric Probe System PM5, in which needles are in electrical contact with ProbeHead arm and to BNC cables for electrical measurements with external electronic instrumentation. Said needles are carefully put in contact with the gold pads or wirings, so that signals can be read without need of additional operations on the sample. A drawback of this method is that the needles may scrape the gold away after many measurements, beside contacting the probes every time being slow and cumbersome. Also, the device cannot be used in inverted configuration.

Another way is to weld copper cables to the pads with *silver paste*, in order to have a steady external connection without using a solderer, which would be risky, since it needs about 400°C in order for tin to melt. This is a really slow process, as silver paste needs hours to harden, and it needs an extremely careful placement, as it is very fragile, especially when just put on the substrate. Moreover, it subsequently needs a 130°C bake to be fully effective.

The last viable method consists of *bonding* the pads or wirings to an external PCB board[118] through Kulicke and Soffa 4124 Universal Ball Bonder, which provides reliable interconnections between a device and a package. It uses a thin gold wire on a variety of materials, with a combination of heat, pressure and ultrasonic energy to make a weld at each end of the wire. The bond is very flimsy and it needs to be put a special glue on, which increases its reliability to external accidents. This is the best option, as substrate capacitances can be reduced to a minimum, and the PCB is far easier to handle than a small silicon or glass substrate. An overview of the complete fabricated device is shown in Figure 4.10, where the thin gold wires are visible and covered by the protective glue.
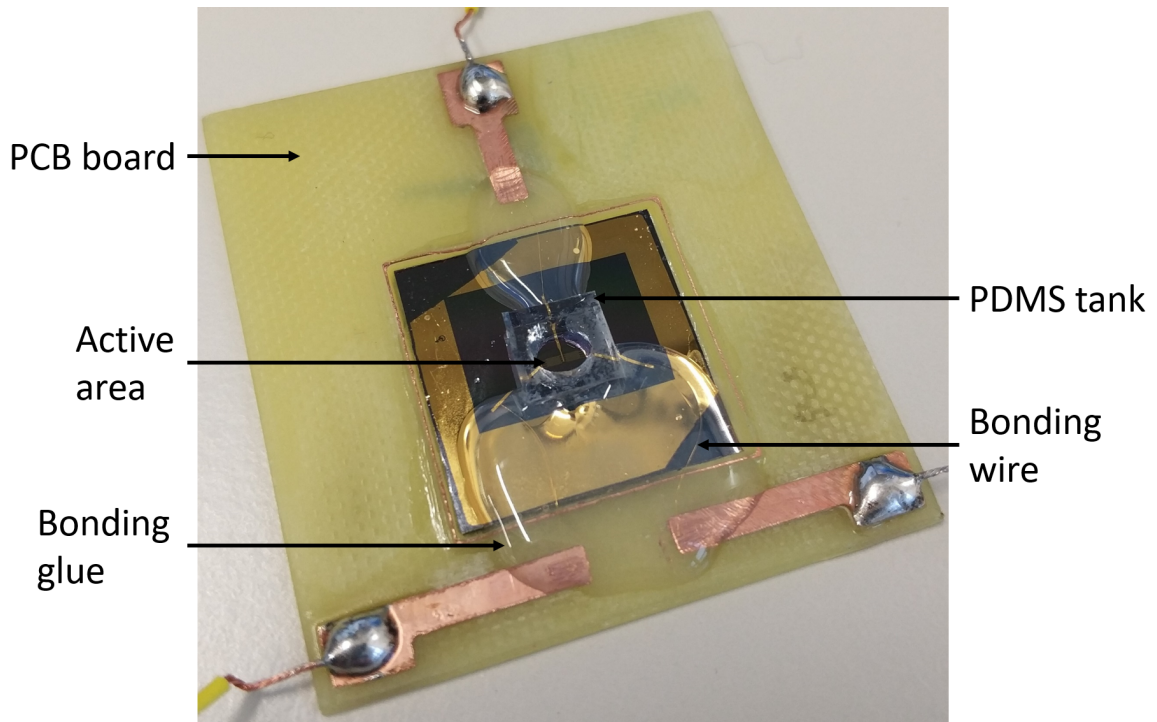
Figure 4.10: An overview of the complete test device

4.7 Experimental setup

4.7.1 Lock-in amplifier

Lock-in amplifier (LIA) is a continuous synchronous band-pass filter, and it can extract a signal modulated on a known carrier frequency[119]. It is also known as Phase-Sensitive Detector (PSD).

It is basically composed of two parts: the first one demodulates the signal through a multiplier, while the second part low-pass filters the signal. A sine wave at a given frequency stimulates the device under test (DUT) and acts as reference. The LIA analyzes then the DUT response and returns amplitude and phase (relative to the reference signal) as outputs, visually explained in Figure 4.11.

Dual-phase demodulation is the adopted technique to determine amplitude and phase of the signal[120]. The input wave is split and multiplied separately by the reference and a quadrature copy of it. The two different outputs are then low-pass filtered and the in-phase and quadrature components are obtained.

Amplitude R and phase Θ are easily derived by a cartesian-to-polar coordinates
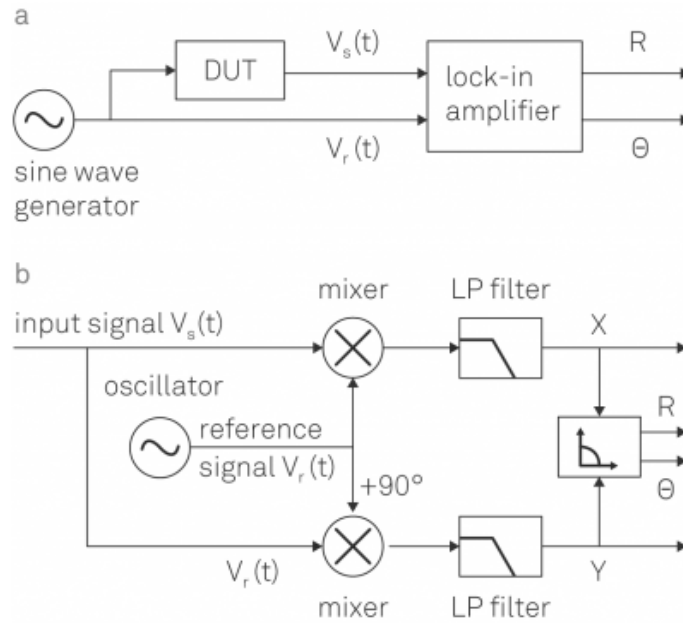
Figure 4.11: a. Working principle of a lock-in measurement   b. Schematic of a dual-phase demodulation lock-in amplifier[120]

transformation using the following relations:

$$R = \sqrt{X^2 + Y^2} \tag{4.2}$$

$$\Theta = \arctan\left(\frac{Y}{X}\right) \tag{4.3}$$

This feature can be rather useful also to acquire the DUT spectrum, discussed in Section 2.2, to have an idea of its resistive and capacitive components and parasitisms, beside choosing the optimal frequency to exploit to execute the measurement. The lock-in technique was deemed suitable for this kind of operation, as it can cover a wide range of frequencies, and it is widely used in biological impedance measurements[121].

The Zurich Instruments HF2LI (Figure 4.12) was adopted as a digital lock-in amplifier covering the frequency range between DC and 50 MHz, connected by high-speed USB interface to a PC, which allows data acquisition at high rate and a graphical user interface program, ZiControl.

The HF2TA Current Amplifier converts input currents into voltage outputs in a wide frequency range up to 50 MHz. In addition, HF2TA Current Amplifier is an active probe which can be conveniently placed close to the measurement setup, and acting as a transimpedance amplifier (TIA) it supports most applications where a
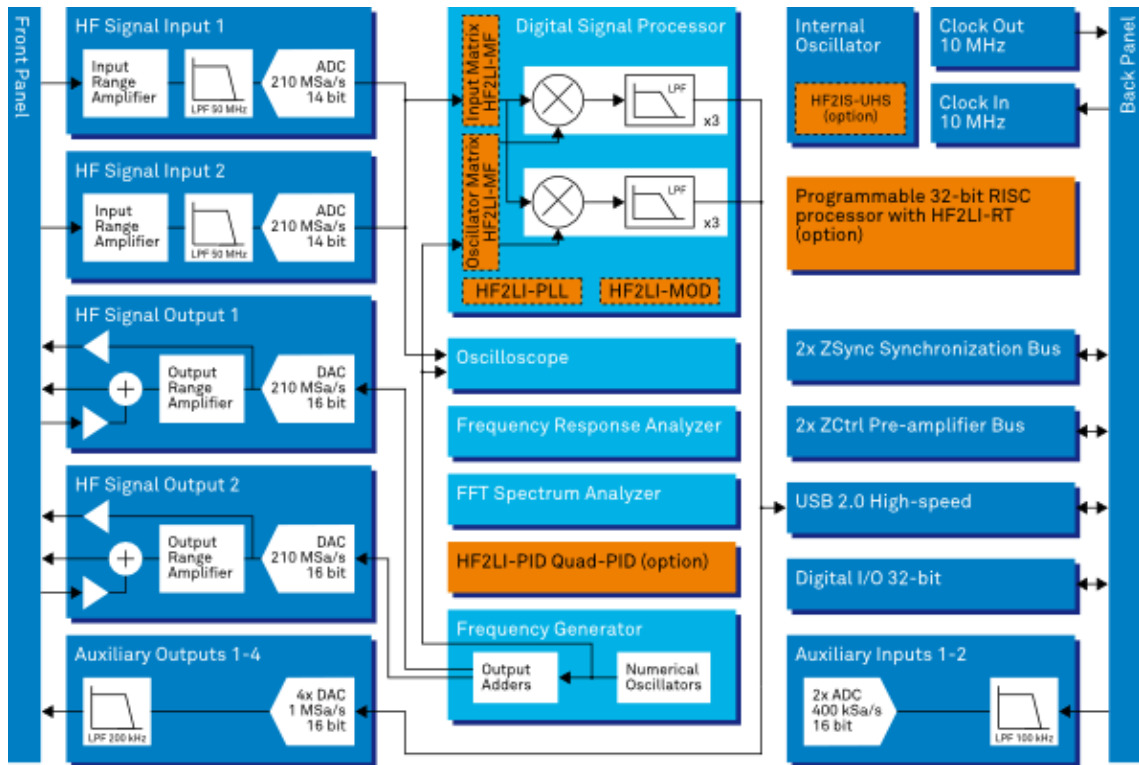
Figure 4.12: Schematic of the employed Zurich Instruments HF2LI lock-in amplifier[120]

current must be converted to a voltage. The dedicated design of the HF2TA ensures stability and a smooth operation over the entire frequency range which the HF2LI is designed for[120].

4.7.2 Custom setup

A custom setup was produced, to better comply with the required specifics, shown in Figure 4.13. It is composed of several distinct objects: a hollow aluminium rod to hold the device and the magnets, which is sustained by a composite acrylic system, which in turn is fixed to an aluminium box with BNC connectors.

Once a small drop of PBS and the particles under test are injected into the PDMS tank, the back surface of the device is bound to the hollow rod by means of double-side sticky tape. The drop does not flow out of it, even when turned upside down, because of surface tension of the PBS, as the hole in the tank is just a couple millimeters wide.

When the device is linked to the BNC connectors, the cylinder must be lowered until the solution is in contact with the underlying glass slide, and the tank is well
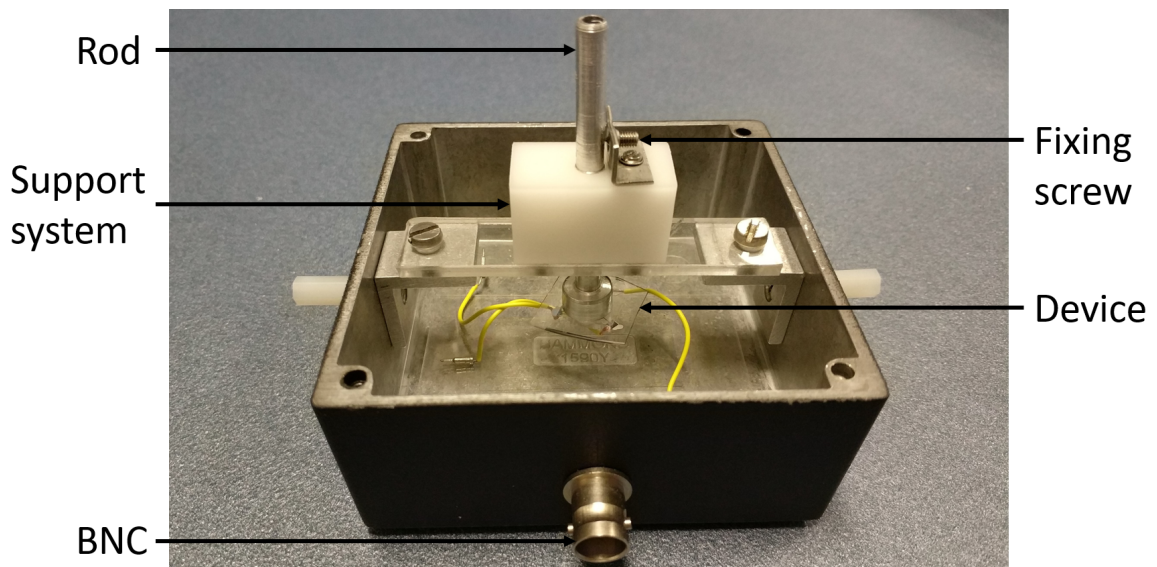
Figure 4.13: The employed custom-made setup

pressed on it, so as to create a sealed container. The saline concentration would otherwise increase as the PBS evaporates, causing consequently a lower solution impedance and a measurement drift. This operation is critical, since the PBS evaporation greatly interferes with the measure. The shaft position has to be fixed with a screw, and the aluminium box must be closed with an aluminium lid, to create a Faraday cage and keep out electromagnetic interferences.

Once the impedance value is stable around the nominal value, a column of magnets can be inserted into the rod and fixed somehow, and basically come in contact with the back side of the sample. Alternatively, the whole box can be turned upside down to let the particles sediment onto the electrodes, if the tested substance is not attracted by the magnets. Even both strategies can be adopted, to facilitate the sedimentation of magnetic particles.

4.7.3 Microscope

A Nikon ECLIPSE FN1 *optical microscope* (Figure 4.14) helped with the measurement monitoring, to have a greater understanding of the particles flow onto concentrators and electrodes, to verify the magnetic concentration during capture experiments, or to link the sedimentation to the impedance variation.

The microscope is equipped with 4× and 60× magnification lenses, to have an overview of the sample or to examine it in detail. Moreover, the 60× lens is an immersion objective, to watch more closely what happens inside the solution.
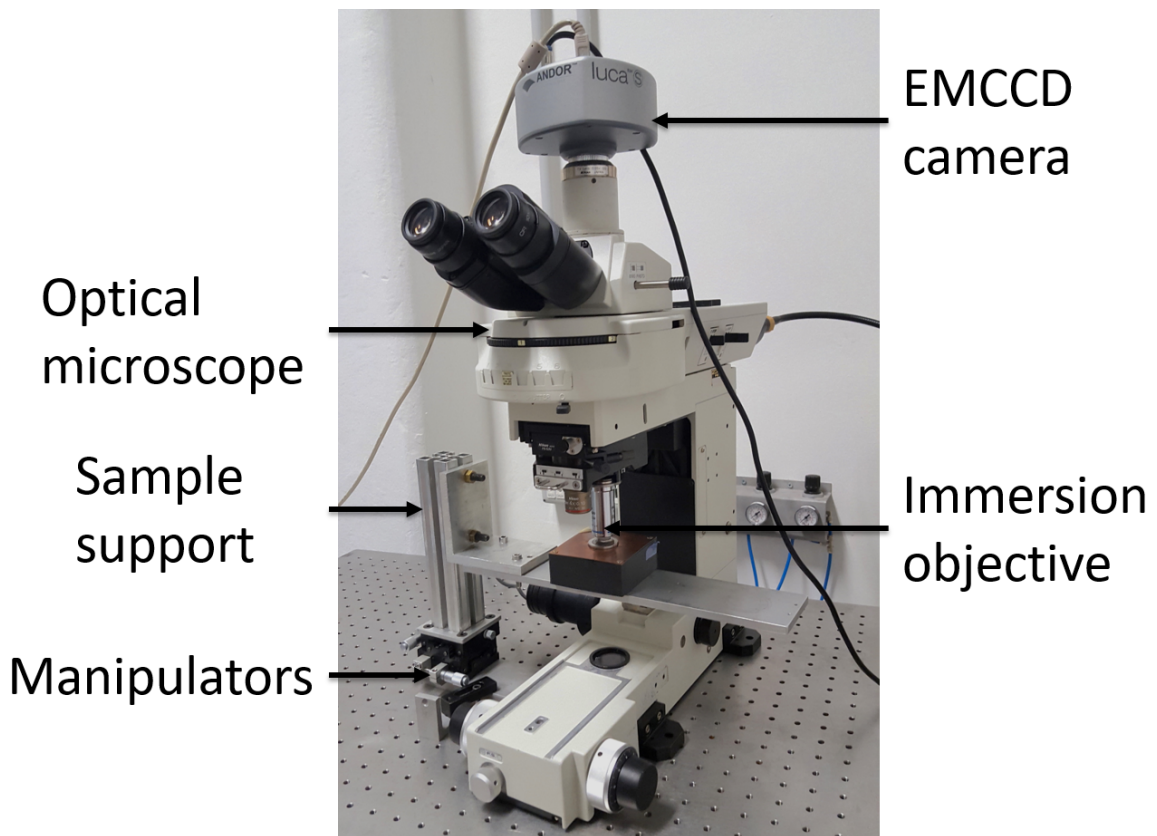
Figure 4.14: Illustration of the microscope setup used during most of the experiments

The microscope provides also two optical filters, to enhance the visibility of magnetic nanoparticles or erythrocytes by exploiting a fluorescent marker. The fluorescine isothiocyanate (FITC) filter is excited at 465–495 nm wavelength (blue) and an absorption band at 515–555 nm, while the tetramethylrhodamine isothiocyanate (TRITC) filter has an excitation band at 525–540 nm (green) and absorbs the red spectral region, 605–655 nm[122].

Besides, the microscope's software (NIS Elements) includes a counting tool, useful to clarify the actual number of beads on the electrodes once they are deposited[123].

4.7.4 Conductive atomic force microscopy

Atomic force microscopy (AFM) is a high-resolution scanning probe microscopy, with demonstrated resolution below the nanometer[87].

The Keysight 5600LS AFM system is made of a cantilever with a sharp tip at its end, acting as a probe on the sample surface. As the tip approaches the sample, forces between the two objects lead to a deflection of the cantilever, measured using

a laser beam and a photodetector, visually represented in Figure 4.15.
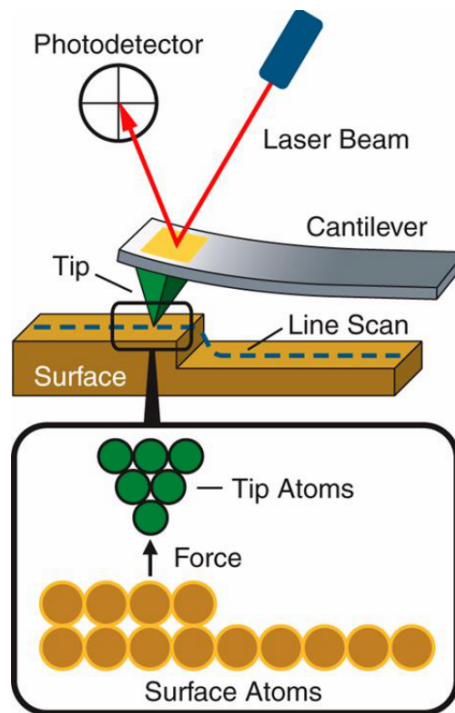
Figure 4.15: Scheme of the working principle of atomic force microscopy[87]

However, it can also be operated as current sensing AFM (CS-AFM), which allows to simultaneously measure the topography of the sample and the current flowing through it, provided that the tip is conductive.

It was used to obtain the low-frequency portion of the hemozoin impedance spectrum, as electrodes allow only a medium-to-high-frequency characterization of particles, because of double-layer effect.

Results are discussed in Section 5.4.

4.7.5 Vibrating sample magnetometer

Vibrating sample magnetometer (VSM) is an instrument capable of measuring magnetic properties of a sample immersed in an external magnetic field, whose working principle is depicted in Figure 4.16.

It measures the magnetic moment of a sample when it is vibrated perpendicularly to a uniform magnetic field[124], allowing for example to determine the magnetic moment as a function of temperature, magnetizing field, and crystallographic orientation. The vibration is provoked by piezoelectric materials or audio speakers, and perturbations of the external magnetic field are measured through a sinusoidal
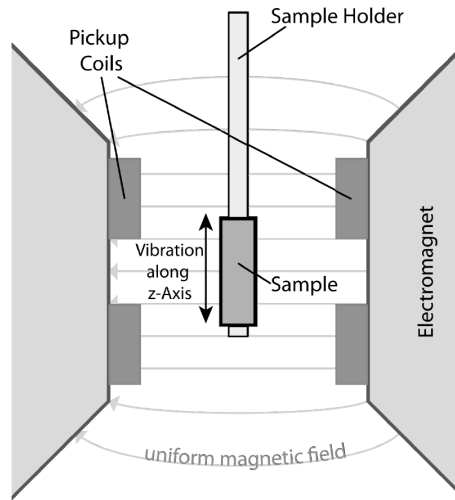
Figure 4.16: Scheme of the working principle of a vibrating sample magnetometer

electromotive force. The read voltage is proportional to the magnetic moment of
the material, according to Faraday's law of induction:

$$V = -\frac{d\Phi_{\mathbf{B}}}{dt} = -\frac{d \iint_S \mathbf{B} \cdot d\mathbf{S}}{dt} \tag{4.4}$$

Where:

- V = Read voltage $[V]$

- $d\mathbf{S} = \mathbf{n}dS$

- $\mathbf{n}$ = Vector normal to the surface S

Considering Equation (2.2), where $\mathbf{H}$ is uniform, it is:

$$V = -\iint_S \mu_0 \cdot \frac{d\mathbf{M}}{dt} d\mathbf{S} \tag{4.5}$$

Magnetic characteristics of hemozoin were still unclear, and the employment
of Microsense EZ9 VSM was required to have an accurate and confident measure
of its magnetic properties, a magnetization curve $\mathbf{M}$ vs. $\mathbf{H}$ above all, treated in
Section 5.4.

Chapter 5

Experimental results

5.1 Tested particles

Preliminary tests with isolating *polystyrene beads* were contemplated in the experimental setup to verify its correct functioning, in preparation for hemozoin and iRBCs measurements.

Differently sized brand polystyrene beads were used, which came suspended in DI water with 10% concentration, but were usually diluted in a bigger PBS volume. Also superparamagnetic beads were tested, to verify that both magnetic and electrical sections worked properly and simultaneously, using various IDE configurations and the so-called *dummy device* (Subsection 5.3.1). The beads have susceptibility $\chi_b \simeq 1$, namely about four orders of magnitude higher than hemozoin crystals, which have $\chi_{HC} \simeq 320 \cdot 10^{-6}$.

The bead solutions were diluted in PBS mainly for two reasons. The first reason is to have a signal with amplitude similar to the expected value, so to have a plausible impedance variation, as PBS has a conductivity similar to plasma. On the other hand, the Nikon counting tool really came in handy to know the actual number of particles deposited on the electrodes, and a lower concentration is visually clearer.

Further tests have been carried out on treated and untreated RBCs, provided by the μBS Lab of the Electronics, Information, and Biomedical Engineering Department of Politecnico di Milano.

A bovine blood and sodium heparin solution is centrifuged so that RBCs are separated from plasma and other blood corpuscles. Sodium heparin acts as *anticoagulant*, and the correct dose is 5000 μL per blood milliliter.

Once apart, RBCs are to be resuspended in PBS to reach the correct hematocrit

level (∼45%), and the whole solution has to be kept at 4°C until utilization. After a 20-minute oxygenation with a peristaltic pump, the suspension is divided in two samples: untreated RBCs (uRBCs), acting as control, and to-be-treated RBCs.

The latter undergo a $NaNO_2$ treatment (30 mg/mL), in order for their haemoglobin to oxidize and become methaemoglobin, thus acquiring paramagnetic properties[125]. The treated RBC (tRBC) solution must be stirred for 30 minutes and used within a day, as the treatment effectiveness is rather brief. The difference between the two samples is visually clear, as shown in Figure 5.1, due to the lack of oxygen in the treated blood.

Figure 5.1: Plain contrast between tRBCs (left) and uRBCs (right)

As a result of the tRBCs paramagnetic properties, they can be deemed as infected RBCs and are therefore an useful test bench to verify the suitability of both device and setup. Hemozoin properties are treated in-depth in Section 5.4.

5.2 Capture tests

Mainly two types of capture tests can be employed, namely direct and inverted configuration. The former consists of leaving the device with the electrodes on the bottom, so that gravity can help the sedimentation of the particles. This was done with all the magnetic particles mentioned in Section 5.1 (superparamagnetic beads, hemozoin crystals, treated erythrocytes), to verify the concentration capability of the magnetic cylinders. Inverted configuration is needed to verify that particles are

actually attracted by the magnetic system. It is also the final device configuration, where non-infected RBCs flow downwards, and only paramagnetic iRBCs and HCs are attracted upwards. Since the magnetic system is in a phase of study and optimization, no inverted-capture tests have been carried out by now on biological particles. Moreover, an inverted microscope is needed to watch particles being attracted.

Fluorescent filters of the Nikon optical microscope were exploited with RBCs labelled with CellTracker Red CMTPX Dye, to have a clearer vision during capture experiments. A TRITC marker was applied to treated and untreated RBCs, so as to exploit the 605–655 nm light spectral region and see then the RBCs as fluorescent red, as in Figure 5.2. Again, direct configuration was used for the capture fluorescence test, with 45-μm-wide and 160-μm-spaced cylinders.

Sedimentation of RBCs is faster than HCs, as they're bigger. This is clearly visible with a confrontation between Figure 5.2 and Figure 5.11, in which time scales are very different.

(a) t=0 min   (b) t=10 min   (c) t=20 min
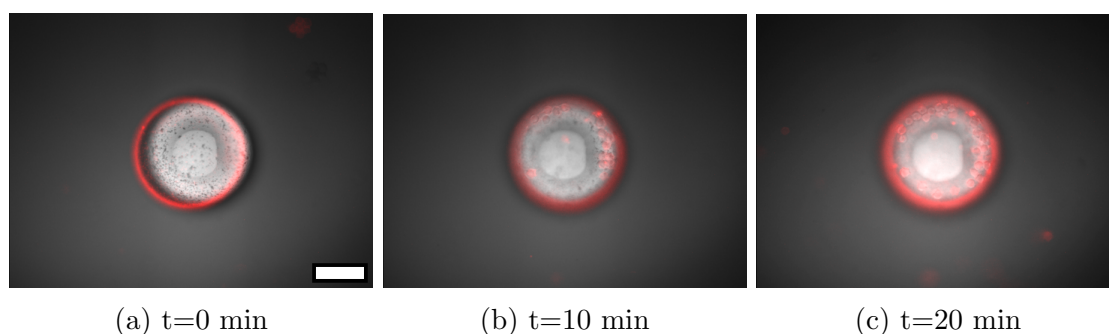
Figure 5.2: Sedimentation and concentration of tRBCs with a TRITC marker. Scale bar is 20 μm

5.3 Electrical tests

The fulfillment of the measurements was performed with the aid of well-known interdigitated electrodes first, and then the custom geometry shown in Figure 4.9 was adopted. Different custom geometries were needed, to adapt to various kind of problems that showed up during the tests, mainly due to frequency range and substrate parasitic effects.

Sigma-Aldrich Phosphate Buffered Saline was the chosen buffer solution for its attributes, similar to plasma's. The Dulbecco's (DPBS) formulation was used[126], as

it provides a chemically defined balanced environment, which maintains structural and physiological integrity of cells in vitro. DPBS is commonly used as a diluent or for cell rinsing, or even as a buffer, like in this case[127]. It needs to be stored at 15–30°C, so room temperature is perfectly fine, and of course it must be used before its expiration date.

The measured conductivity is about 1.5 $\frac{S}{m}$ at room temperature, in agreement with literature data[128], and it strongly depends on temperature with a *negative coefficient* (NTC). It means that as temperature rises the solution resistance R_{sol} decreases, in contrast with most metals and electrical components in general.

As mentioned in Chapter 3, all the electrodes were designed to have a reasonable R_{sol} value, of the order of 50–500 Ω at room temperature, keeping in mind DPBS conductivity. Moreover, the double-layer contribution should be negligible at the measure frequency, and all the devices were designed to have a plateau resemblance at least, where possible. The measure frequency varied from 500 kHz to 3 MHz during different tests, depending on f_{low} (Equation (3.3)) of the specific device. The low-pass filter (LPF) band of the lock-in amplifier was set to about 0.5 Hz, to have a sufficient filtering of the thermal noise. The expected signal is a quite slow for hemozoin and erythrocytes, so this frequency can be further reduced.

The voltage amplitude of the reference signal was set to 10 mV, causing the measured current to be of the order of 5–20 μA, depending on the used configuration. Higher voltages can damage the device, as current densities can increase quite a bit. A current of this order of magnitude can be easily read by the instrumentation though, so the chosen value was deemed a reasonable trade-off.

The protocol usually applied for the measure is the one discussed in Subsection 4.7.2.

Various particle concentrations were used, to verify the linear relation of the impedance variation, given by Equation (2.17). Still, since the concentration may broadly vary, depending on numerous factors, manually counting the particles is overall a better solution. The concentration variation may be due to internal flows inside the container of the bead solution and in the PDMS tank, resulting in a variability in both withdrawal and deposition of the solution with a pipette. When the active area was too broad or the particle concentration was too high, only few random samples were taken, and then averaged on the whole area.

In Figure 5.3 current spectra are reported, which are raw data measured by the LIA, and should be scaled by the applied voltage (10 mV) to obtain the admittance. Then a more meaningful impedance spectrum can be derived. They were obtained

(a) 8 μm interdigitated electrodes, silicon substrate

(b) 8 μm interdigitated electrodes, glass substrate

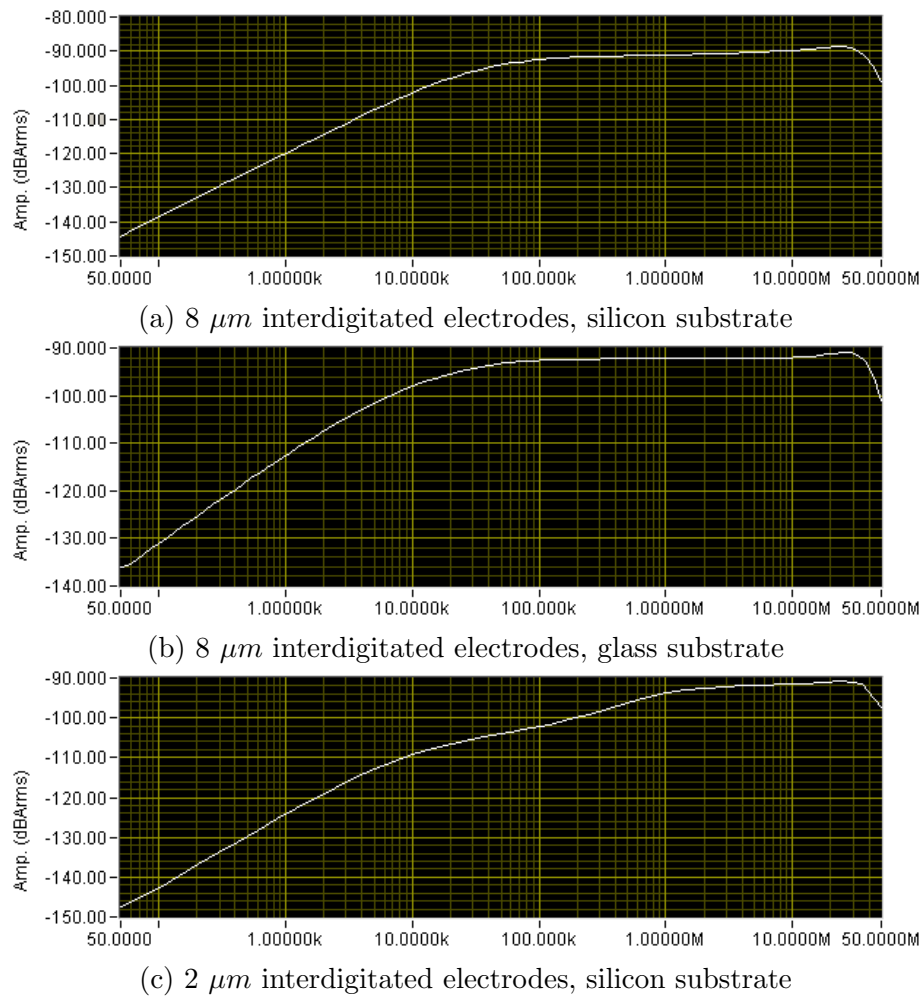(c) 2 μm interdigitated electrodes, silicon substrate

Figure 5.3: Current spectra of various interdigitated configurations, obtained with Zurich Instruments HF2LI and ZiControl

by logarithmically sweeping the whole 50 Hz–50 MHz spectrum in 60 points, and measuring the current at those frequencies. The applied voltage was 10 mV also during these measures.

It is clear that 8 μm electrodes perform better overall, as expected, for their lower double-layer capacitance. The different shape of the spectrum in Figure 5.3c is probably due to the wiring resistive contribution through the solution, as they are closer with respect to the configurations in Figure 5.3a and Figure 5.3b. Glass substrate is slightly better than silicon, but the additional effort during fabrication is not justified by this subtle difference. Moreover, the final device cannot be fabricated on glass slides, as electroplating is feasible only on conductive substrates. Around 30 MHz the signal is subject to an abrupt drop, caused by the limited bandwidth of the instrument. This outcome is not dependent on the device, but it is not very

relevant anyway, since it shows up well above the maximum investigated frequency, namely 10 MHz.
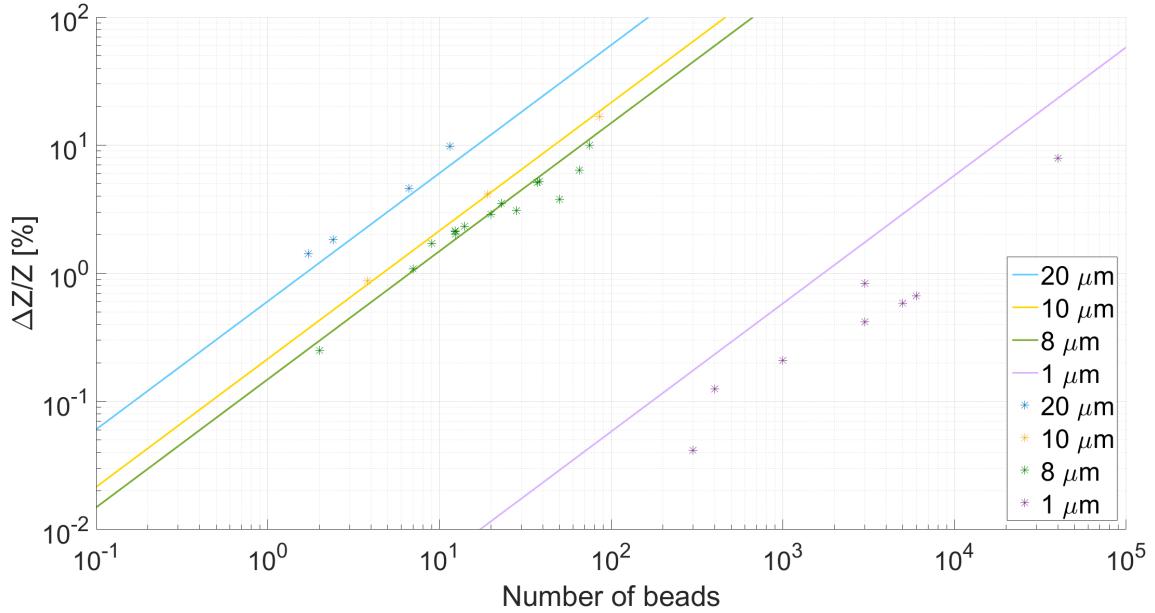
(a) Lines show theoretical variation curves, while asterisks show measured data
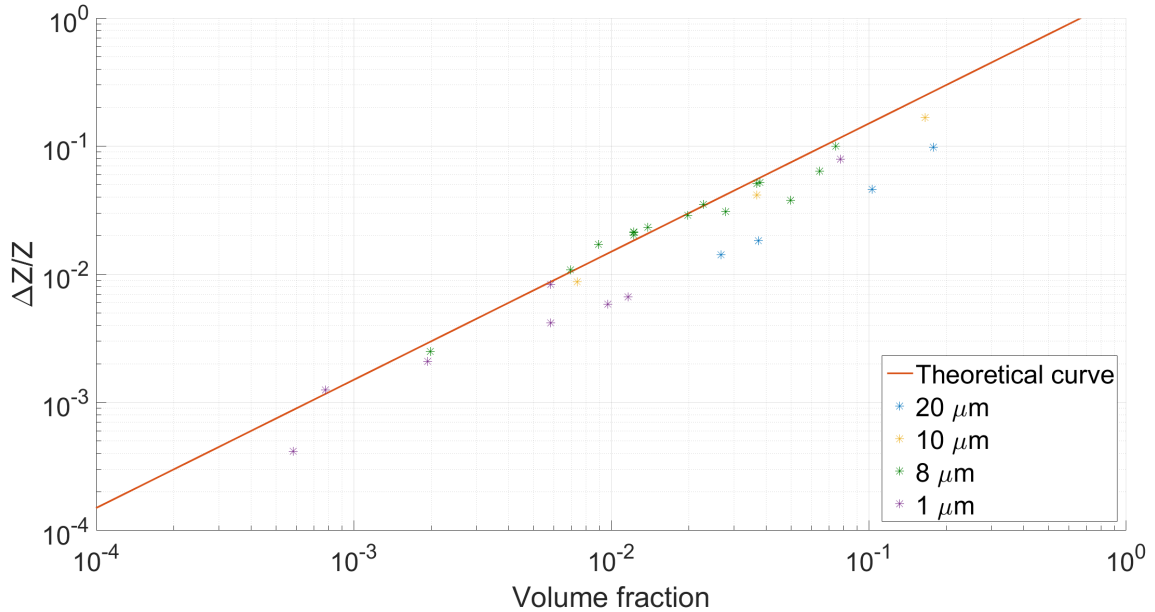
(b) All the particles are on the same curve, as it is related to the occupied volume fraction

Figure 5.4: Measured data for differently-sized superparamagnetic beads fits in with the theoretical curve given by Equation (2.17), using 8 μm IDE

In Figure 5.4 different impedance variation are shown, all given by beads, to validate Equation (2.17) and Equation (2.14). Lines represent theoretical curves, while asterisks are measured data, in which only the smallest beads (1 μm) are superpara-

magnetic. The number of beads reported in Figure 5.4a is relative to the average of various areas provided by NIS elements, which displays about 150 $\mu m \times$ 200 μm at a time. It can be said that the relation is confirmed, as the data fits in reasonably well. The variability may be due to test reproducibility, rough counting, injecting differences, or thermal drifts.

5.3.1 Dummy device
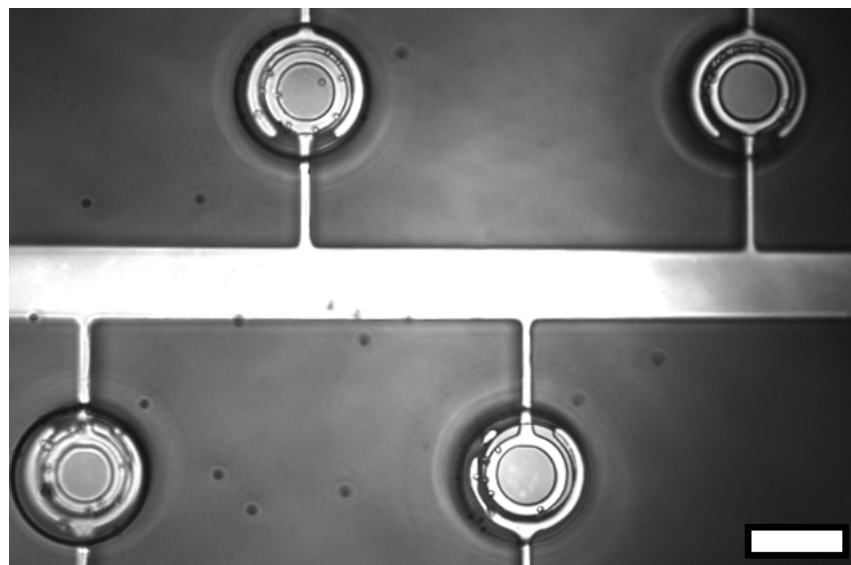
(a) Microscopy image of the captured superparamagnetic beads
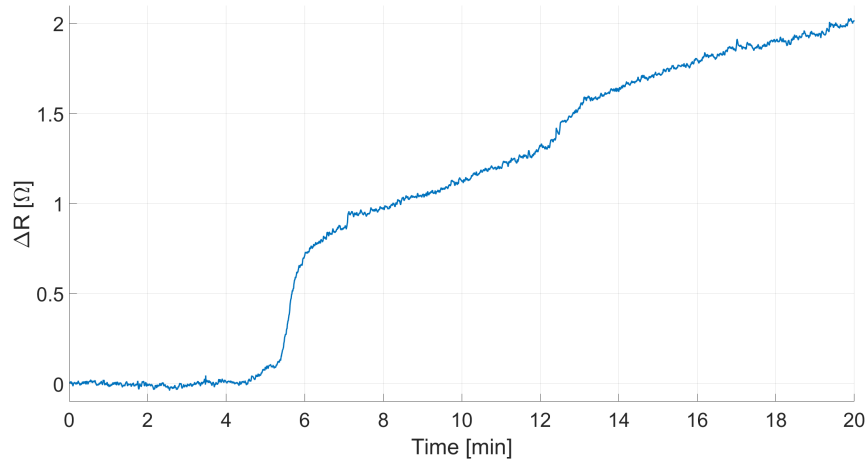
(b) Impedance variation given by the attracted beads

Figure 5.5: Experiment showing captured beads and corresponding impedance variation. A glimpse of the nickel concentrators is visible in (a), as the SU-8 layer is optically transparent. Scale bar is 20 μm

A dummy device is a test tool used to validate the idea behind the actual device,

Figure 5.6: Current spectrum of the dummy device, obtained with Zurich Instruments HF2LI and ZiControl

using however 1-μm-wide superparamagnetic beads, whose attraction time is much shorter than HCs and RBCs. This can be seen by comparing the time scales of Figure 5.5b to the ones in Figure 5.8b and to Figure 5.13b.

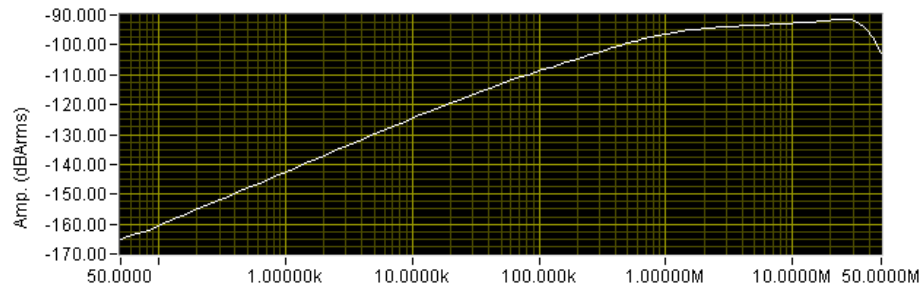The electroplating process is not fully optimized yet, and it certainly does not guarantee a sufficiently planar and smooth surface to allow a lithography process on top of it. 50-nm-thick evaporated concentrators were used instead, to allow a partial integration of the two layers. These nickel cylinders are magnetically less powerful than the 20-μm ones, but this is compensated by the use of the superparamagnetic beads. The employed setup was the one discussed in Subsection 4.7.2.

For the main purpose of this device, namely magnetic plus electrical experiments, glass substrate is not feasible because of fabrication issues. In Figure 5.6 its spectrum is shown, with a resistive plateau starting at about 1 MHz. Also in this device the high-frequency spectrum measurement is limited by the instrument bandwidth.

Hemozoin and erythrocytes tests were not possible with this setup, due to the insufficient attraction and concentration capacity of these magnets, as HCs and RBCs have a susceptibility several orders of magnitude lower than superparamagnetic beads. Figure 5.5a shows that concentrators attract beads along their circumference, although concentrators are not very efficient, due to their limited height.

The electrical layer working principle and characteristics are very similar to the final device, as reported by Figure 5.5b. The measurement in this case should be faster, as the beads are superparamagnetic, but a few observations can be made. The concentrators obviously don't attract very far, and in this case the PBS droplet is relatively thick, about 3 mm. So the main attraction work should be done by the magnet column, which in turn is kind of far from the sample surface (a couple of millimeters), and the thickness of the wafer must be taken into account.

Theoretical confirmation is given by Figure 5.7a, which puts in relation differ-
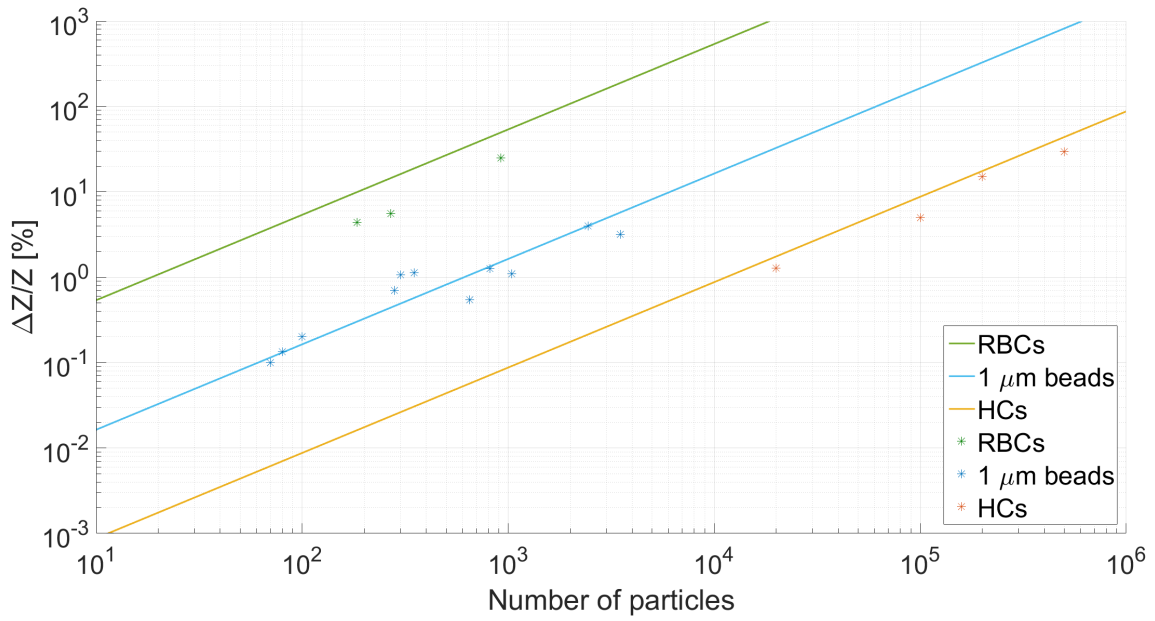
(a) Percentage impedance variation versus number of particles
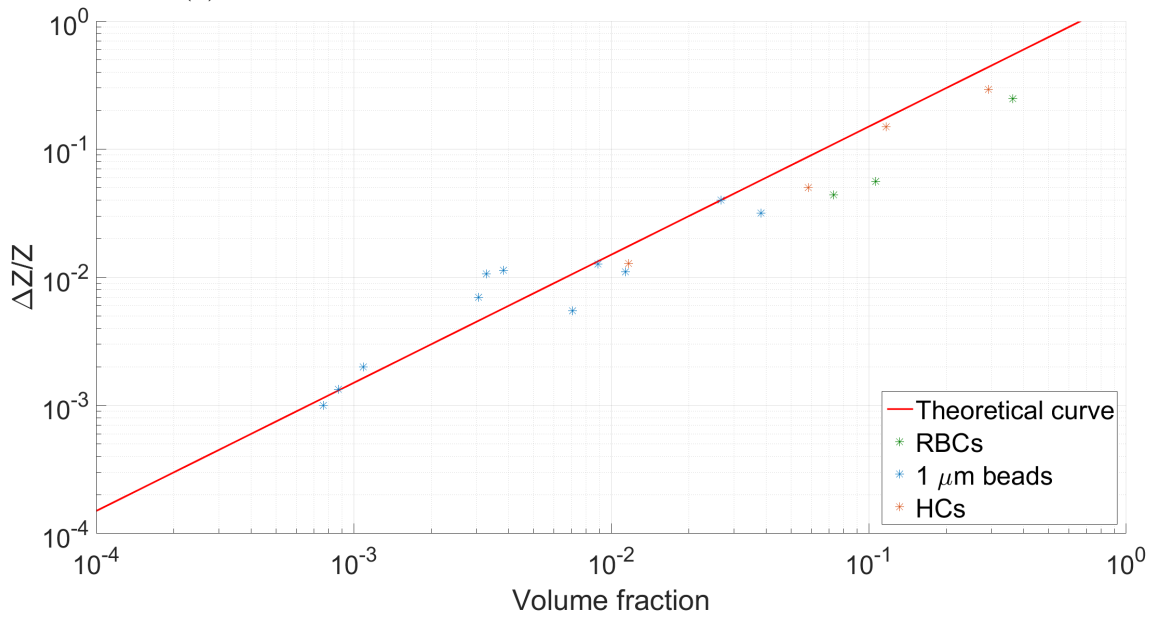
(b) Impedance variation versus volume fraction

Figure 5.7: Measured data for particles fits in with theoretical curves using the dummy device, which gives approximately the same variation of IDE, further validating Equation (2.17)

ent measured numbers of particles with their corresponding theoretical impedance variation. This graph is obtained by counting the particles deposited on the electrodes and compute their mean value, in order to quantify the occupied volume fraction. Last of all, the theoretical impedance variation can be derived according

to Equation (2.17). The aforementioned relation receives additional agreement from Figure 5.7b, as the measured data fits in with the theoretical values, considering measurement variability. To have a significant signal due to the small hemozoin, the number of crystals should be rather high. Therefore, a precise count of both number of crystals and volume fraction is not possible, and the measured data is quite approximate, based on small-area counts and rough estimates on the total occupied area, respectively.

RBCs impedance tests were accomplished in direct configuration with untreated RBCs, and they were consistent with the expected data, in fact the difference between the curves in Figure 5.8b is reasonable, taking into account some measure variability.

(a) 0.012% RBC concentration
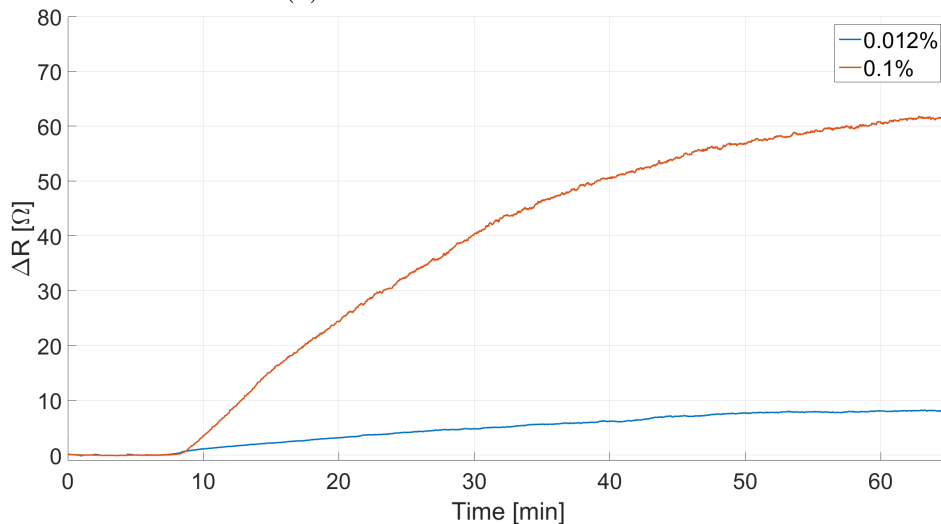
(b) 0.012% and 0.1% RBC concentration comparison

Figure 5.8: Sedimentation of red blood cells with increasing RBC concentration, and corresponding impedance variation. RBCs are poorly visible, as they are transparent. Of course there are some also onto the SU-8 layer, since this was just a sedimentation test, concentrators were not present. Scale bar is 20 μm

5.4 Hemozoin properties

Synthetic hemozoin crystals were bought from InvivoGen[129], provided as solid dark-green to black crystals, with a measured density of 1.49±0.01 $^g/cm^3$, to be stored at -20°C. Upon resuspension in DI water or PBS, for both magnetic and electrical characterization, crystals can be stored at 4°C. Hemozoin concentration in PBS was ~100 $^{\mu g}/mL$, and possibly diluted additionally to vary its concentration for electrical tests.

In Figure 5.9 SEM images of hemozoin crystals are reported, to verify their size and shape.

(a) Close-up of HCs and some 1-μm beads   (b) Hemozoin crystals in scale
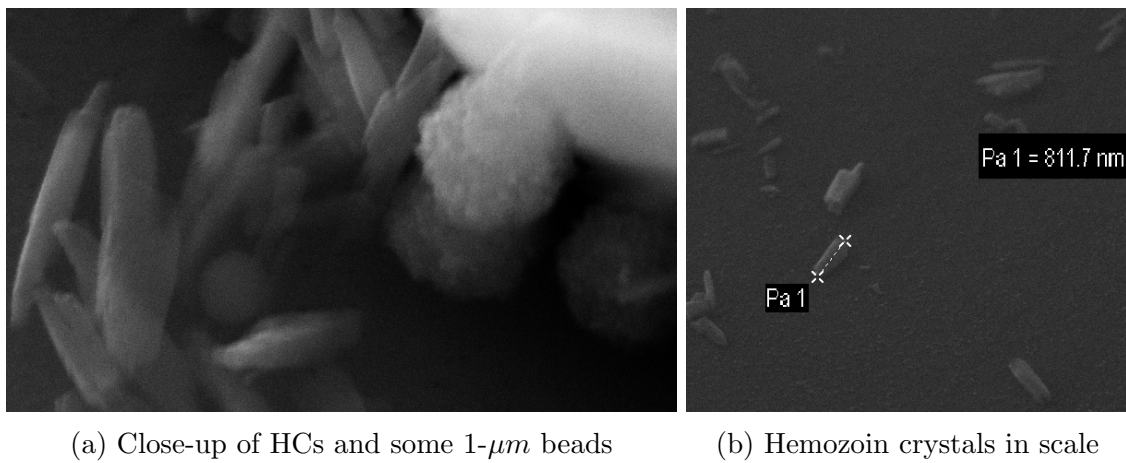
Figure 5.9: SEM images of hemozoin crystals

5.4.1 Magnetic properties

VSM measures were necessary to assess the magnetic properties of hemozoin crystals with reasonable confidence. First of all, a reference sample was measured, to have an idea of the signal given by the HC container, namely a plastic cuvette. It is fundamental to be extremely careful avoiding sample contamination, as even a tiny flake of paramagnetic or ferromagnetic material could invalidate the whole measure. The hemozoin sample was inserted in said cuvette, then fixed to the VSM quartz stick. The average net magnetization, after the subtraction of the background noise of the cuvette, is shown in Figure 5.10, where magnetization **M** is in electromagnetic unit (emu) and the magnetic field **H** is in oersted (Oe).

Starting from Equation (2.1) and considering that the magnetization **M** is the
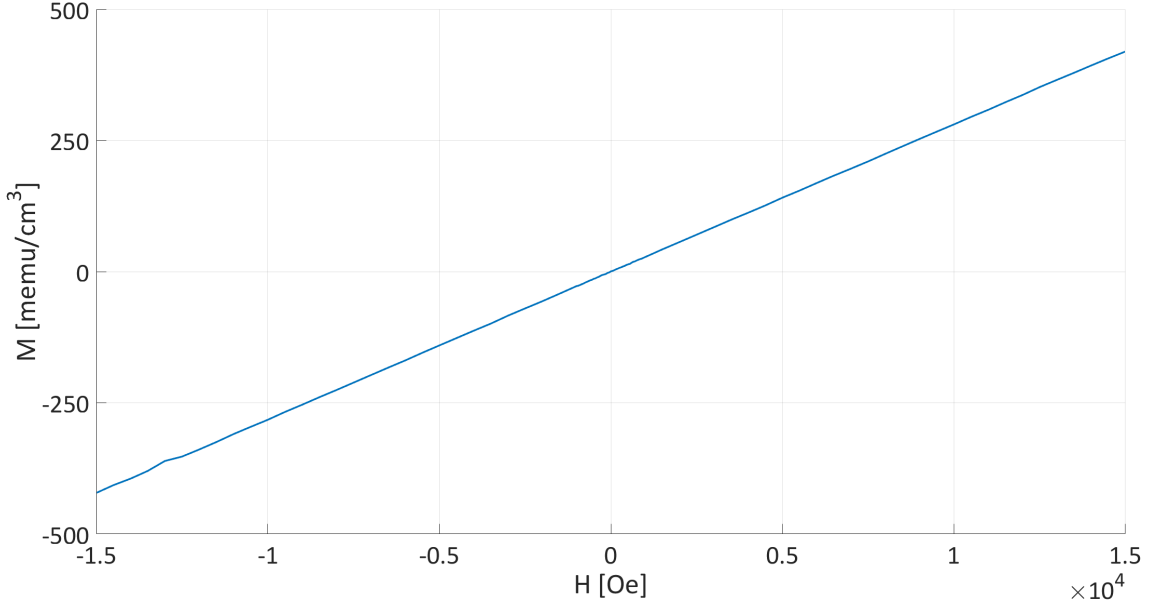
Figure 5.10: VSM measure of synthetic hemozoin crystals, the angular coefficient is $6.2234 \cdot 10^{-5}$ memu/Oe

magnetic moment m per unit volume, the volume magnetic susceptibility χ_{HC} is:

$$\chi_{HC} = \frac{\Delta m}{V_{HC} \cdot \Delta \mathbf{H}} = \frac{6.3152 \cdot 10^{-8} \left[\frac{emu}{Oe}\right]}{2.21 \cdot 10^{-3} \left[cm^3\right]} \cdot 4\pi 10^{-3} = 354 \cdot 10^{-6} \qquad (5.1)$$

The measured volume susceptibility value $\chi_{HC} = (350 \pm 20) \cdot 10^{-6}$ means that hemozoin has paramagnetic properties, in accordance with some bibliographic data [19,20], but it is definitely not superparamagnetic as claimed by Inyushin et Al. [21]

Direct configuration was employed for the capture test in Figure 5.11, with 45-μm-wide cylinders and a spacing of 160 μm. It is clear that there is a preferential side where HCs are attracted, which may be due to some non-uniform features of the pillars or an irregularity of the magnetic field in that area.

5.4.2   Electrical properties

In agreement with what initially anticipated [9], hemozoin crystals show an insulating behaviour at both low and medium frequency. The CS-AFM bandwidth is limited to 6 kHz, while the HF2LI can go up to 50 MHz, but as already explained a complete impedance spectrum is not achievable.

Hemozoin conductivity at low frequency was measured by means of DC IV curves.   Crystals were suspended in DI water and spread on a gold-coated sili-

(a) t=0 min   (b) t=30 min   (c) t=60 min
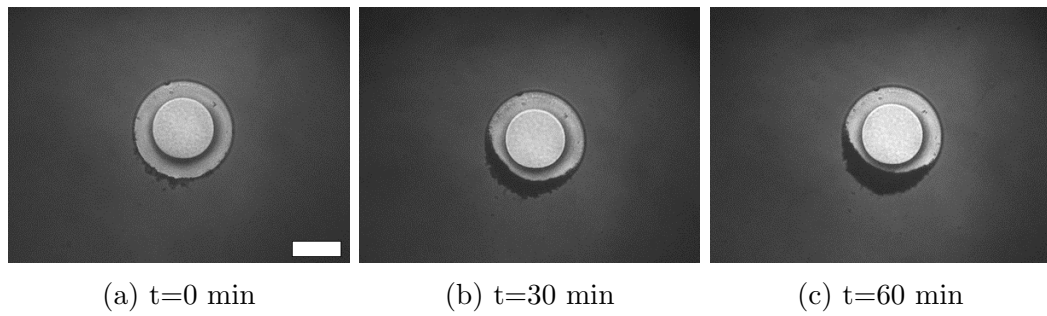
Figure 5.11: Sedimentation and concentration of HCs, it can be noted that the area around the concentrator is free of hemozoin. Scale bar is 20 μm

con substrate, which was left on a hotplate until water was fully evaporated. The PtIr-coated conductive tip applied a voltage in the range of ± 10 V to the sample. As soon as the tip contacted the gold substrate, the current saturated to the maximum readable value (10 nV), while hemozoin measured current was lower than a few picoamperes, indicating the insulating behaviour shown in Figure 5.12. Tests on gold were performed before and after hemozoin measurement to check the tip status, that is to see if the conductive coating wore off.
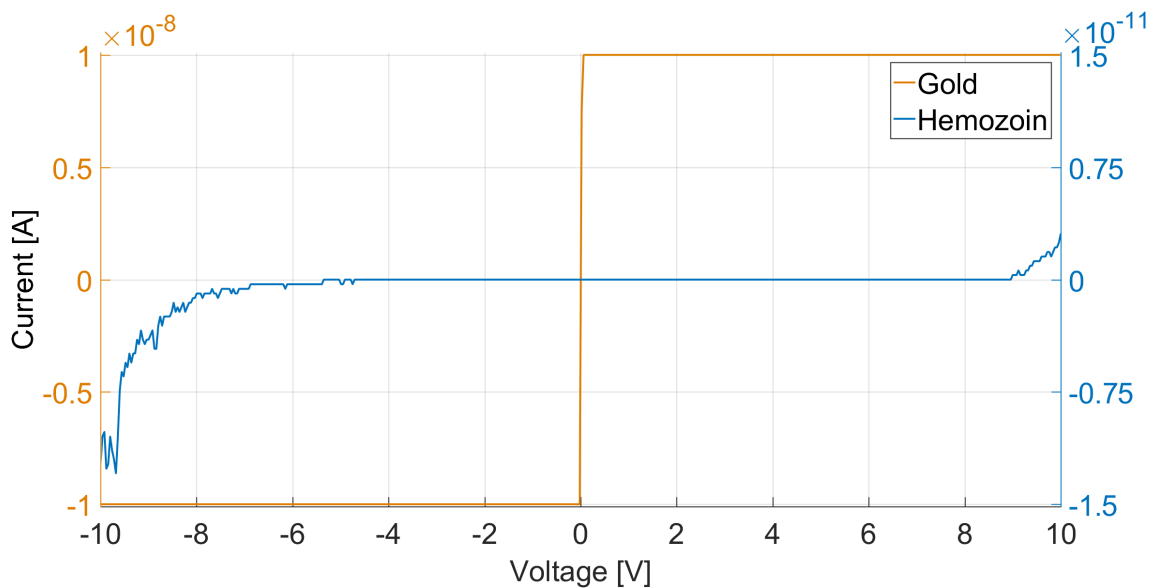
Figure 5.12: Evidence of hemozoin crystals insulating behaviour, given by an IV curve

Regarding the medium-to-high frequency measurement, HCs were characterized at 3 MHz with both interdigitated electrodes and dummy device, to be almost completely free of their double-layer capacitance. Sedimentation tests on IDE proved that hemozoin is electrically more insulating than PBS, reported in Figure 5.13,

in which the resistive component is highlighted. In this test the sedimentation of HCs was helped by a weak magnet, in fact it required tens of minutes to deposit completely. However, an increased resistance can be observed, concordant in sign and amplitude with the expected variation.

(a) Microscopy image of the deposited hemozoin crystals
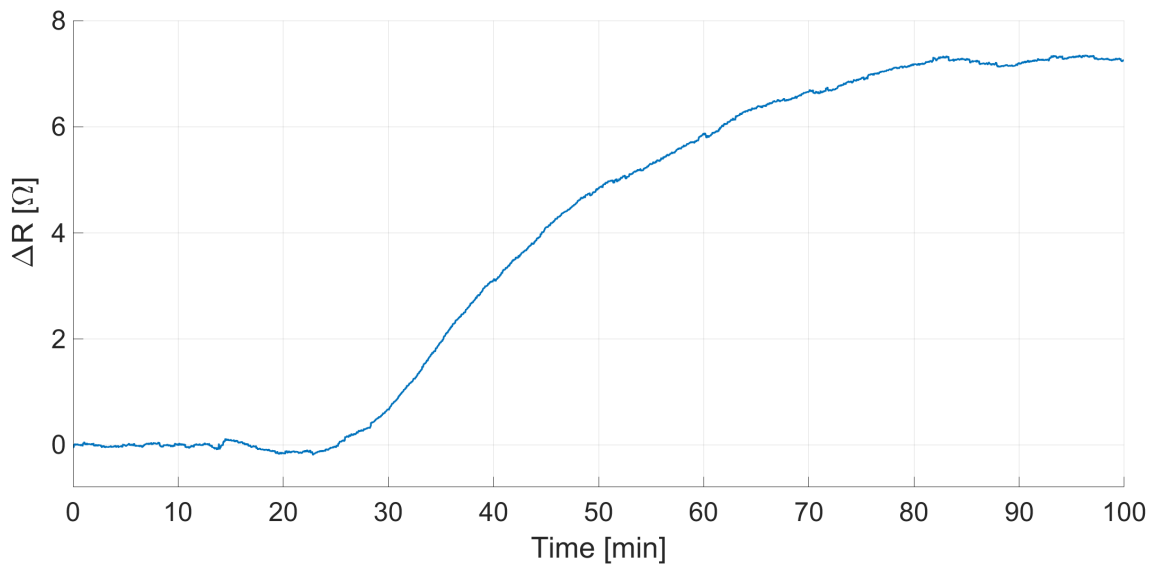
(b) Hemozoin impedance variation

Figure 5.13: Experiment showing hemozoin sedimentation on 2 μm IDE, slightly helped by a weak magnet, and corresponding impedance variation. Scale bar is 10 μm

These results are encouraging, as they mean that hemozoin can be used as a tool to electrically diagnose malaria. For example, if it had about the same conductivity of plasma or PBS, an impedance sensor could have not been possible, as impedance would have not changed significantly once HCs were attracted. Furthermore, if it was more conductive than the medium, lots of hemozoin crystals could have compensated

the signal due to an insulating red blood cell, or at least diminished it, invalidating then the measure. In these two cases, a much more complex sensor should have been designed, specifically tailored to attract RBCs and to reduce hemozoin contribution.

Conclusions and future perspectives

This thesis work has been proficient from multiple standpoints.

From the magnetic point of view, it has been demonstrated that it is possible to attract and concentrate in small areas magnetic particles up to 500 μm away from the device surface, enhancing the conditions for electrical measurements. The magnetic system can still be optimized to improve capture distance, efficiency, and time, by employing a different configuration of both macroscopic magnetic system and microstructures. An electroplating process was developed to insert the magnetic structures in a silicon substrate. The control of the height needs to be optimized, to achieve a sufficient planarity, so that the entire fabrication process flow can be fulfilled.

Hemozoin magnetic properties have been cleared, verifying that crystals are paramagnetic, further confirming that it is a powerful label-free tool to diagnose malaria.

Regarding electrical readout of the sensor, an optimal geometry for the electrodes has been modelled, designed, fabricated and tested. Its parasitic components have been highlighted and analyzed, focusing on their minimization through various techniques. Moreover, it has been proven that non-microfluidic magnetic separation and impedance count is possible on the same chip, opening new possibilities concerning diagnostic tests. For example, labelling pathological particles with a superparamagnetic marker is viable, not only for malaria, but also for other diseases which release cells in the bloodstream, like some cancer types. The actual feasibility of this opportunity should be quantitatively and positively assessed, though.

Hemozoin electrical conductivity has also been investigated, establishing that it is behaves like an insulator in various frequency ranges (DC and MHz). This is a fundamental result, as it makes feasible a simple impedance count of both hemozoin and erythrocytes. A complete impedance characterization has not been possible, as the project is still in a preliminary phase, and a fully-developed effective

magnetic setup is not ready yet. As a consequence, only direct configuration helped by sedimentation and high hemozoin concentrations have been tested, and a proper assessment of the minimum detectable signal has not been achieved. Designing the electronic reading module is the next step to take, to quantify with a high level of confidence the electrical limit of detection, possibly adapting the geometry to improve the impedance variation at the determined frequency.

The whole measurement environment then needs to be thought about and implemented, to fully automate the diagnosis, possibly measuring multiple samples at the same time, to speed up the entire process.

Once these operations are thoroughly finalized and the reliability of the device is adequately high, human infected blood can be tested. First of all, the testing has to be done on known unhealthy samples, to confirm the performance of the device with respect to gold standard and other present diagnostic methods. Eventually, mass production and subsequent marketing of the device should happen.

Bibliography

[1] World Health Organization. World Malaria Report, www.who.int/malaria. Technical report, World Health Organization, 2015.

[2] World Health Organization. WHO Guidelines, www.who.int/malaria.

[3] E Du, S Ha, M Diez-Silva, M Dao, S Suresh, and AP Chandrakasan. Electric impedance microflow cytometry for characterization of cell disease states. *The Royal Society of Chemistry*, 13(19):3903–3909, 2013.

[4] Wikipedia: The Free Encyclopedia. Malaria Wikipedia Webpage, it.wikipedia.org/wiki/Malaria.

[5] AK Tripathi, DJ Sullivan, and MF Stins. Plasmodium falciparum-Infected Erythrocytes Decrease the Integrity of Human Blood-Brain Barrier Endothelial Cell Monolayers. *The Journal of Infectious Diseases*, 195(7):942–950, 2007.

[6] The CRUDEM Foundation. Slideshare Website, www.slideshare.net/CRUDEMFoundation, 2012.

[7] Center for Disease Control and Prevention. CDC Guidelines, www.cdc.gov.

[8] Sigma-Aldrich. Giemsa Stain Technical Datasheet, www.sigma-aldrich.com. 2006.

[9] PN Simao. *Exploring impedance spectroscopy as a mean of malaria diagnostic.* PhD thesis, IST, 2014.

[10] CD Fitch and P Kanjananggulpan. The state of ferriprotoporphyrin IX in malaria pigment. *Journal of Biological Chemistry*, 262(32):15552–15555, 1987.

[11] S Pagola, PW Stephens, DS Bohle, AD Kosar, and SK Madsen. The structure of malaria pigment beta-haematin. *Nature*, 404:307–310, 2000.

[12] AFG Slater, WJ Swiggard, BR Orton, WD Flitter, DE Goldberg, A Cerami, and GB Henderson. An iron-carboxylate bond links the heme units of malaria pigment. In *Proceedings of the National Academy of Sciences*, volume 88, pages 325–329, 1990.

[13] MF Oliveira, SW Kycia, A Gomez, AJ Kosar, DS Bohle, E Hempelmann, D Menezes, MA Vannier-Santos, PL Oliveira, and ST Ferreira. Structural and morphological characterization of hemozoin produced by Schistosoma mansoni and Rhodnius prolixus. *FEBS Letters*, 579(27):6010–6016, 2005.

[14] Wikipedia: The Free Encyclopedia. Hemozoin Wikipedia Webpage, en.wikipedia.org/wiki/Hemozoin.

[15] T Hänscheid, TJ Egan, and MP Grobusch. Haemozoin: from melatonin pigment to drug target, diagnostic tool, and immune modulator. *Lancet Infectious Diseases*, 7(10):675–685, 2007.

[16] T Sun and H Morgan. Single-cell microfluidic Impedance cytometry: A review. *Microfluidics and Nanofluidics*, 8(4):423–443, 2010.

[17] GS Noland, N Briones, and DJ Sullivan. The shape and size of hemozoin crystals distinguishes diverse Plasmodium species. *Molecular and Biochemical Parasitology*, 130(2):91–99, 2003.

[18] AN Hoang. *Hemozoin: A Case of Heme crystal engineering*. PhD thesis, Graduate School of Vanderbilt University, 2010.

[19] S Hackett, J Hamzah, TME Davis, and TG St Pierre. Magnetic susceptibility of iron in malaria-infected red blood cells. *Biochimica et Biophysica Acta - Molecular Basis of Disease*, 1792(2):93–99, 2009.

[20] LM Coronado, CT Nadovich, and C Spadafora. Malarial hemozoin: From target to tool. *Biochimica et Biophysica Acta*, 1840(6):2032–2041, 2014.

[21] M Inyushin, Y Kucheryavih, L Kucheryavih, L Rojas, I Khmelinskii, and V Makarov. Superparamagnetic Properties of Hemozoin. *Scientific Reports*, 6(1):26212, 2016.

[22] LR Moore, H Fujioka, PW Stephens, JJ Chalmers, B Grimberg, P Zimmerman, and M Zborowski. Hemoglobin degradation in malaria-infected erythro-

cytes determined from live cell magnetophoresis. *FASEB Journal*, 20(6):747–749, 2006.

[23] TF Kong, W Ye, WK Peng, HW Hou, Marcos, PR Preiser, NT Nguyen, and J Han. Enhancing malaria diagnosis through microfluidic cell enrichment and magnetic resonance relaxometry detection. *Scientific Reports*, 5(June):1–12, 2015.

[24] World Health Organization. Malaria prevention works, www.who.int/malaria. Technical report, World Health Organization, 2017.

[25] J Kim, M Massoudi, JF Antaki, and A Gandini. Removal of malaria-infected red blood cells using magnetic cell separators: A computational study. *Applied Mathematics and Computation*, 218(12):6841–6850, 2012.

[26] S Kasetsirikul, J Buranapong, W Srituravanich, M Kaewthamasorn, and A Pimpin. The development of malaria diagnostic techniques: a review of the approaches with focus on dielectrophoretic and magnetophoretic methods. *Malaria Journal*, 15(1):358, 2016.

[27] CW Pirnstill and GL Coté. Malaria Diagnosis Using a Mobile Phone Polarized Microscope. *Scientific Reports*, 5(1):13368, 2015.

[28] PA Zimmerman, JM Thomson, H Fujioka, and WE Collins. Diagnosis of Malaria by magnetic deposition microscopy. *The American Society of Tropical Medicine and Hygiene*, 74(4):568–572, 2013.

[29] A Orban, M Rebelo, P Molnar, IS Albuquerque, A Butykai, and I Kezsmarki. Efficient monitoring of the blood-stage infection in a malaria rodent model by the rotating-crystal magneto-optical method. *Scientific Reports*, 6(23218), 2016.

[30] DM Newman, J Heptinstall, RJ Matelon, L Savage, ML Wears, J Beddow, M Cox, HDFH Schallig, and PF Mens. A Magneto-Optic Route toward the In Vivo Diagnosis of Malaria: Preliminary Results and Preclinical Trial Data. *Biophysical Journal*, 95(2):994–1000, 2008.

[31] A Butykai, A Orban, V Kocsis, D Szaller, S Bordács, E Tátrai-Szekeres, LF Kiss, A Bóta, BG Vértessy, T Zelles, and I Kézsmárki. Malaria pigment crystals as magnetic micro-rotors: key for high-sensitivity diagnosis. *Scientific Reports*, 3(1):1431, 2013.

[32] J Nam, H Huang, H Lim, CS Lim, and S Shin. Magnetic separation of malaria-infected red blood cells in various developmental stages. *Analytical Chemistry*, 15(85):7316–7323, 2013.

[33] KH Han and BA Frazier. Paramagnetic capture mode magnetophoretic microseparator for high efficiency blood cell separations. *The Royal Society of Chemistry*, 6(2):265–273, 2006.

[34] M Zborowski, GR Ostera, LR Moore, S Milliron, JJ Chalmers, and AN Schechter. Red blood cell magnetophoresis. *Biophysical Journal*, 84(4):2638–2645, 2003.

[35] L Yang. Electrical impedance spectroscopy for detection of bacterial cells in suspensions using interdigitated microelectrodes. *Talanta*, 74(5):1621–1629, 2008.

[36] WH Coulter. Electromagnetic Flowmeter, 1956.

[37] RW DeBlois and CP Bean. Counting and Sizing of Submicron Particles by the Resistive Pulse Technique. *The American Institute of Physics*, 41(7):909–916, 1970.

[38] RA Hoffman and WB Britt. Flow-System Measurement of Cell Impedance Porperties. *The Journal of Histochemistry and Cytochemistry*, 27(1):234–240, 1979.

[39] RA Hoffman, TS Johnson, and WB Britt. Flow cytometric electronic direct current volume and radiofrequency impedance measurements of single cells and particles. *Cytometry*, 1(6):377–384, 1981.

[40] R Rodriguez-Trujillo, CA Mills, J Samitier, and G Gomila. Low cost micro-Coulter counter with hydrodynamic focusing. *Microfluidics and Nanofluidics*, 3(2):171–176, 2007.

[41] R Rodriguez-Trujillo, O Castillo-Fernandez, M Garrido, M Arundell, A Valencia, and G Gomila. High-speed particle detection in a micro-Coulter counter with two-dimensional adjustable aperture. *Biosensors and Bioelectronics*, 24(2):290–296, 2008.

[42] M Ibrahim, J Claudel, D Kourtiche, and M Nadi. Geometric parameters optimization of planar interdigitated electrodes for bioimpedance spectroscopy. *Journal of Electrical Bioimpedance*, 4(1):13–22, 2013.

[43] J Hong, DS Yoon, SK Kim, TS Kim, S Kim, EY Pak, and K No. AC frequency characteristics of coplanar impedance sensors as design parameters. *The Royal Society of Chemistry*, 5(3):270–279, 2005.

[44] M Carminati. Advances in High-Resolution Microscale Impedance Sensors. *Journal of Sensors*, 2017, 2017.

[45] KF Lei. Review on impedance detection of cellular responses in micro/nano environment. *Micromachines*, 5(1):1–12, 2014.

[46] M Vakilian and BY Majlis. Study of interdigitated electrode sensor for lab-on-chip applications. In *IEEE International Conference on Semiconductor Electronics*, pages 201–204, 2014.

[47] NF Sheppard, RC Tucker, and C Wu. Electrical Conductivity Measurements Using Microfabricated Interdigitated Electrodes. *Analytical Chemistry*, 65(9):1199–1202, 1993.

[48] SC Bhakdi, A Ottinger, S Somsri, P Sratongno, P Pannadaporn, P Chimma, P Malasit, K Pattanapanyasat, and HPH Neumann. Optimized high gradient magnetic separation for isolation of Plasmodium-infected red blood cells. *Malaria Journal*, 9(38), 2010.

[49] BL Wood, J Andrews, S Miller, and DE Sabath. Refrigerated storage improves the stability of the complete blood cell count and automated differential. *American Journal of Clinical Pathology*, 112(5):687–695, 1999.

[50] Stephen Blundell. *Magnetism in Condensed Matter*. Oxford University Press, 1st edition, 2001.

[51] AG Kolhatkar, AC Jamison, D Litvinov, RC Willson, and TR Lee. Tuning the magnetic properties of nanoparticles. *International Journal of Molecular Sciences*, 14(8):15977–16009, 2013.

[52] M Monticelli. *Micromagnetic devices for single-cell mechanobiology*. PhD thesis, Politecnico di Milano, 2017.

[53] CM Tchen. *Mean Value and Correlation Problems connected with the Motion of Small Particles supended in a turbulent fluid.* Springer, 1947.

[54] AB Basset. *A treatise on Hydrodynamics: with numerous examples.* Deighton, Bell & Co., 1888.

[55] CF Lee. Introduction to Multiphase Flows, 2015.

[56] GG Stokes. *On the Effect of the Internal Friction of Fluids on the Motion of Pendulums.* Cambridge: Pitt Press, 1851.

[57] JR Macdonald. Impedance spectroscopy. *Annals of Biomedical Engineering*, 20:289–305, 1991.

[58] M Carminati, C Caviglia, A Heiskanen, M Vergani, G Ferrari, M Sampietro, TL Andresen, and J Emneus. Comparison of microelectrode sensing configurations for impedimetric cell monitoring. In *Proceedings of the International Workshop on Impedance Spectroscopy*, pages 1–10, 2012.

[59] C Ribaut, K Reybier, O Reynes, J Launay, A Valentin, PL Fabre, and F Nepveu. Electrochemical impedance spectroscopy to study physiological changes affecting the red blood cell after invasion by malaria parasites. *Biosensors and Bioelectronics*, 24(8):2721–2725, 2009.

[60] Mosaic Industries. Mosaic Documentation, www.mosaic-industries.com, 2005.

[61] JC Maxwell. A treatise of Electricity and Magnetism. *Clarendon Press*, 1, 1881.

[62] JB Johnson. Thermal agitation of electricity in conductors. *Physical Review*, 32(1):97–109, 1928.

[63] JA Barnes and DW Allan. A Statistical Model of Flicker Noise. In *Proceedings of the IEEE*, volume 54, pages 176–178, 1966.

[64] ET McAdams, J Jossinet, R Subramanian, and RGE McCauley. Characterization of gold electrodes in phosphate buffered saline solution by impedance and noise measurements for biological applications. In *Annual International Conference of the IEEE Engineering in Medicine and Biology - Proceedings*, pages 4594–4597, 2006.

[65] DC Grahame. The electrical double layer and the theory of electrocapillarity. *Chemical Reviews*, 41(3):441–501, 1947.

[66] JB Jorcin, ME Orazem, N Pébère, and B Tribollet. CPE analysis by local electrochemical impedance spectroscopy. *Electrochimica Acta*, 51(8-9):1473–1479, 2006.

[67] M Giesbers, JM Kleijn, and MA Cohen Stuart. The Electrical Double Layer on Gold Probed by Electrokinetic and Surface Force Measurements. *Journal of Colloid and Interface Science*, 248(1):88–95, 2002.

[68] M Carminati, G Ferrari, SU Kwon, M Sampietro, M Monticelli, A Torti, D Petti, E Albisetti, M Cantoni, and R Bertacco. Towards the impedimetric tracking of single magnetically trailed microparticles. In *2014 IEEE 11th International Multi-Conference on Systems, Signals and Devices*, pages 1–5, 2014.

[69] S Chen, RS Ingram, MJ Hostetler, JJ Pietron, RW Murray, TG Schaff, JT Khoury, MM Alvarez, and RL Whetten. Gold Nanoelectrodes of Varied Size: Transition to Molecule-Like Charging. *Science*, 280(5372):2098–2101, 1998.

[70] SE Moulton, JN Barisci, A Bath, R Stella, and GG Wallace. Studies of double layer capacitance and electron transfer at a gold electrode exposed to protein solutions. *Electrochimica Acta*, 49(24):4223–4230, 2004.

[71] T Wandlowski. Electrochemical Nanoscience Lab, Electrochemical double layer, wandlowski.dcb.unibe.ch/research, 2007.

[72] B Hirschorn, ME Orazem, B Tribollet, V Vivier, I Frateur, and M Musiani. Determination of effective capacitance and film thickness from constant-phase-element parameters. *Electrochimica Acta*, 55(21):6218–6227, 2010.

[73] RW Bowen and TA Doneva. Atomic Force Microscopy Studies of Membranes: Effect of Surface Roughness on Double-Layer Interactions and Particle Adhesion. *Journal of Colloid and Interface Science*, 229(2):544–549, 2000.

[74] S Zheng, M Liu, and YC Tai. Micro coulter counters with platinum black electroplated electrodes for human blood cell sensing. *Biomedical Microdevices*, 10(2):221–231, 2008.

[75] A Mortari, A Maaroof, D Martin, and MB Cortie. Mesoporous gold electrodes for sensors based on electrochemical double layer capacitance. *Sensors and Actuators*, 123(1):262–268, 2007.

[76] AS Brown. A Type of Silver Chloride Electrode Suitable for use in Dilute Solutions. *Journal of the American Chemical Society*, 56(3):646–647, 1934.

[77] T Sato, G Masuda, and K Takagi. Electrochemical properties of novel ionic liquids for electric double layer capacitor applications. *Electrochimica Acta*, 49(21):3603–3611, 2004.

[78] N Pamme. Magnetism and microfluidics. *The Royal Society of Chemistry*, 6(1):24–38, 2006.

[79] Q Ramadan, DP Poenar, and Chen Yu. Customized trapping of magnetic particles. *Microfluidics and Nanofluidics*, 6(1):53–62, 2009.

[80] S Takashima, K Asami, and Y Takahashi. Frequency domain studies of impedance characteristics of biological cells using micropipet technique. *Biophysical Journal*, 54(6):995–1000, 1988.

[81] COMSOL Inc. COMSOL Multiphysics Documentation, www.comsol.com.

[82] BS Bull, MA Schneiderman, and G Brecher. Platelet counts with the Coulter counter. *American Journal of Clinical Pathology*, 44(6):678–688, 1965.

[83] RA Serway and JWJ Jewett. *Physics for Scientists and Engineers*. Thomson Brooks/Cole, 6th edition, 2006.

[84] F Lacy. Developing a theoretical relationship between electrical resistivity, temperature, and film thickness for conductors. *Nanoscale Research Letters*, 6(1):636, 2011.

[85] G Kastle, HG Boyen, A Schroder, A Plettl, and P Ziemann. Size effect of the resistivity of thin epitaxial gold films. *Physical Review B*, 70(16):1–6, 2004.

[86] International Organization for Standardization. ISO 14644-1 Standard, www.iso.org/standard/53394.

[87] PoliFab. PoliFab Website, www.polifab.polimi.it/equipments.

[88] JA Hoerni. Method of manufacturing semiconductor devices, 1962.

[89] AZ Electronic Materials. AZ40XT-11D Technical Datasheet, www.microchemicals.com.

[90] AUS e TUTE. Electroplating Concepts, www.ausetute.com.au/electroplate.

[91] SAM Al-Bat'hi. Electrodeposition of Nanostructure Materials. *Electroplating of Nanostructures*, pages 3–25, 2015.

[92] NM Osero. An overview of pulse plating. *Plating and Surface Finishing*, 73(3):20–22, 1986.

[93] K Zandi, Yi Zhao, J Schneider, and YA Peter. New photoresist coating method for high topography surfaces. In *Proceedings of the IEEE International Conference on Micro Electro Mechanical Systems (MEMS)*, pages 392–395, 2010.

[94] JB Yoon, GY Oh, CH Han, E Yoon, and CK Kim. Planarization and trench filling on severe surface topography with thick photoresist for MEMS. In *Proceedings of SPIE - The International Society for Optical Engineering*, volume 3511, pages 297–306, 1998.

[95] RK Trichur, M Fowler, JW McCutcheon, and M Daily. Filling and Planarizing Deep Trenches with Polymeric Material for Through-Silicon Via Technology. In *International Symposium on Microelectronics*, pages 192–196, 2010.

[96] YX Li, PJ French, and RF Wolffenbuttel. Plasma Planarization for Sensor Applications. *Journal of Microelectromechanical Systems*, 4(3):132–138, 1995.

[97] PB Zantye, A Kumar, and AK Sikder. Chemical mechanical planarization for microelectronics applications. *Materials Science and Engineering Reports*, 45(3-6):89–220, 2004.

[98] JM Shaw, JD Gelorme, NC LaBianca, WE Conley, and SJ Holmes. Negative photoresists for optical lithography. *IBM Journal of Research and Development*, 41(1):81–94, 1997.

[99] MicroChemicals. Ti Prime Technical Datasheet, www.microchemicals.com. 2016.

[100] M Teodorescu. Research on Biomimetics Applicability in Textile Products, Master Thesis, 2012.

[101] Merck Performance Materials GmbH. AZ5214e Technical Datasheet, www.microchem.com.

[102] Wikipedia: The Free Encyclopedia. Photoresist Wikipedia Webpage, en.wikipedia.org/wiki/Photoresist.

[103] H Lorenz, M Despont, N Fahrni, N LaBianca, P Renaud, and P Vettiger. SU-8: a low-cost negative resist for MEMS. *Journal of Micromechanics and Microengineering*, 7(3):121–124, 1997.

[104] Heidelberg Instruments Mikrotechnik GmbH. MLA 100 Factsheet, www.himt.de.

[105] P Sigmund. Theory of Sputtering. I. Sputtering Yield of Amorphous and Polycrystalline Targets. *Physical Review*, 184(2):383–416, 1969.

[106] JS Chapin. Sputtering process and apparatus, 1979.

[107] Visual Science. Visual Science Project Website, visual-science.com/projects/magnetron-sputtering, 2008.

[108] G Bräuer, B Szyszka, M Vergöhl, and R Bandorf. Magnetron sputtering - Milestones of 30 years. *Vacuum*, 84(12):1354–1359, 2010.

[109] D Hegemann, H Brunner, and C Oehr. Plasma treatment of polymers for surface and adhesion improvement. *Nuclear Instruments and Methods in Physics Research, Section B: Beam Interactions with Materials and Atoms*, 208(1-4):281–286, 2003.

[110] SH Kim, SW Na, NE Lee, YW Nam, and YH Kim. Effect of surface roughness on the adhesion properties of Cu/Cr films on polyimide substrate treated by inductively coupled oxygen plasma. *Surface and Coatings Technology*, 200(7):2072–2079, 2005.

[111] A Qureshi, JH Niazi, S Kallempudi, and Y Gurbuz. Label-free capacitive biosensor for sensitive detection of multiple biomarkers using gold interdigitated capacitor arrays. *Biosensors and Bioelectronics*, 25(10):2318–2323, 2010.

[112] Microchem. SU-8 2000 Technical Datasheet, www.microchem.com.

[113] A del Campo and C Greiner. SU-8: a photoresist for high-aspect-ratio and 3D submicron lithography. *Journal of Micromechanics and Microengineering*, 17(6):R81–R95, 2007.

[114] R Feng and RJ Farris. Influence of processing conditions on the thermal and mechanical properties of SU8 negative photoresist coatings. *J. Micromechanics Microengineering*, 13(1):80–88, 2003.

[115] F Chambon and HH Winter. Linear Viscoelasticity at the Gel Point of a Crosslinking PDMS with Imbalanced Stoichiometry. *Journal of Rheology*, 31(8):683–697, 1987.

[116] BH Jo, LM Van Lerberghe, KM Motsegood, and DJ Beebe. Three-dimensional micro-channel fabrication in polydimethylsiloxane (PDMS) elastomer. *Journal of Microelectromechanical Systems*, 9(1):76–81, 2000.

[117] JR Anderson, DT Chiu, RJ Jackman, O Chemiavskaya, JC McDonald, H Wu, SM Whitesides, and GM Whitesides. Fabrication of topologically complex three-dimensional microfluidic systems in PDMS by rapid prototyping. *Analytical Chemistry*, 72(14):3158–3164, 2000.

[118] HW Conru, SE Gons, GC Osborne, DWJ Phelps, SG Starr, and WC Ward. Method of bonding gold or gold allow wire to lead tin solder, 2005.

[119] PA Remillard and MC Amorelli. Lock-in amplifier, 1993.

[120] Zurich Instruments. Zurich Instruments Documentation, www.zhinst.com.

[121] M Min, O Martens, and T Parve. Lock-in measurement of bio-impedance variations. *Measurement*, 27:21–28, 2000.

[122] Nikon Instruments. MicroscopyU Website, www.microscopyu.com.

[123] Nikon Instruments. Nikon Instruments Documentation Website, www.nikoninstruments.com.

[124] S Foner. Versatile and Sensitive Vibration-Sample Magnetometer. *The Review of scientific instruments*, 30(7):550–557, 1959.

[125] L Pauling and CD Coryell. The Magnetic Properties and Structure of Hemoglobin, Oxyhemoglobin and Carbonmonoxyhemoglobin. In *Proceedings of the National Academy of Sciences*, volume 22, pages 210–216, 1936.

[126] R Dulbecco and M Vogt. Plaque Formation and Isolation of Pure Lines With Poliomyelitis Viruses. *The Journal of Experimental Medicine*, 99(2):167–182, 1954.

[127] SAFC Biosciences. Dulbecco's PBS Formulation, www.safcbiosciences.com.

[128] S Gawad, L Schild, and P Renaud. Micromachined impedance spectroscopy flow cytometer for cell analysis and particle sizing. *The Royal Society of Chemistry*, 1(1):76, 2001.

[129] InvivoGen. Hemozoin Technical Datasheet, www.invivogen.com/hemozoin.